

**ELECTRONIC TRANSPORT THROUGH NANOWIRES:  
A REAL-SPACE FINITE-DIFFERENCE APPROACH**

Petr Khomyakov

Samenstelling promotiecommissie:

Prof.dr. H. Rogalla	Universiteit Twente, voorzitter
Prof.dr. P.J. Kelly	Universiteit Twente, promotor
Dr. G. Brocks	Universiteit Twente, assistent promotor
Prof.dr.ir. H. Hilgenkamp	Universiteit Twente
Prof.dr. D. Lohse	Universiteit Twente
Prof.dr.ir. A. van der Avoird	Radboud Universiteit Nijmegen
Prof.dr. S. Blügel	Forschungszentrum Jülich, IFF-Institute and University of Aachen (RWTH)
Prof.dr. J.M. van Ruitenbeek	Universiteit Leiden

Het werk beschreven in dit proefschrift maakt deel uit van het onderzoeksprogramma van het gebied Chemische Wetenschappen van de Nederlandse Organisatie voor Wetenschappelijk Onderzoek (NWO-CW).

P. Khomyakov,  
Electronic transport through nanowires: a real-space finite-difference approach  
Proefschrift Universiteit Twente, Enschede.  
ISBN: 90-365-2350-8  
Copyright © P. Khomyakov, 2006  
Printed by FEBODRUK BV, Enschede

---

**ELECTRONIC TRANSPORT THROUGH NANOWIRES:  
A REAL-SPACE FINITE-DIFFERENCE APPROACH**

PROEFSCHRIFT

ter verkrijging van  
de graad van doctor aan de Universiteit Twente,  
op gezag van de rector magnificus,  
prof.dr. W.H.M. Zijm,  
volgens besluit van het College voor Promoties  
in het openbaar te verdedigen  
op donderdag 11 mei 2006 om 15.00 uur

door

**Petr Khomyakov**

geboren op 25 maart 1975  
te Minsk

Dit proefschrift is goedgekeurd door:

Prof.dr. P. J. Kelly

promotor

Dr. G. Brocks

assistent promotor

to my family



# Contents

<b>1</b>	<b>Introduction</b>	<b>1</b>
1.1	Electronic structure methods for atomic-sized conductors . . . . .	1
1.2	Density functional theory . . . . .	2
1.2.1	Hohenberg-Kohn theorem . . . . .	3
1.2.2	Kohn-Sham equation . . . . .	4
1.2.3	Density functionals: local-density approximation . . . . .	5
1.3	Pseudopotential method . . . . .	6
1.3.1	Plane-wave basis set . . . . .	7
1.3.2	Real-space finite-difference representation . . . . .	10
1.4	Electronic transport . . . . .	11
1.4.1	Landauer-Büttiker formalism . . . . .	11
1.4.2	Electronic structure methods for conductance calculations . . . . .	14
<b>2</b>	<b>Conductance calculations for quantum wires and interfaces</b>	<b>19</b>
2.1	Introduction . . . . .	19
2.2	Hamiltonian . . . . .	20
2.3	Mode matching approach . . . . .	21
2.3.1	Bloch matrices . . . . .	22
2.3.2	Transmission matrix . . . . .	23
2.3.3	Green function matrix . . . . .	25
2.4	Green function approach . . . . .	25
2.4.1	Partitioning . . . . .	25
2.4.2	Transmission matrix . . . . .	26
2.5	Mode matching versus Green functions . . . . .	27
2.5.1	Green functions of ideal wires in terms of Bloch matrices . . . . .	28
2.5.2	Equivalence of mode matching and Green function approaches . . . . .	30
2.5.3	Invariance of transmission probability . . . . .	30
2.5.4	The Caroli expression . . . . .	31
2.5.5	Transmission matrix: a compact expression . . . . .	33
2.6	Examples . . . . .	33
2.6.1	A simple analytical model . . . . .	33
2.6.2	Fe vacuum Fe tunnel junction . . . . .	36
2.7	Summary . . . . .	41

<b>3</b>	<b>Real-space finite-difference method for conductance calculations</b>	<b>43</b>
3.1	Introduction . . . . .	43
3.2	Computational Method . . . . .	45
3.2.1	Finite-difference approximation . . . . .	45
3.2.2	Ideal wire . . . . .	47
3.2.3	Scattering problem . . . . .	49
3.2.4	Computational costs . . . . .	52
3.3	Results . . . . .	53
3.3.1	Numerical tests . . . . .	53
3.3.2	Sodium atomic wires . . . . .	57
3.4	Summary . . . . .	61
<b>4</b>	<b>Electronic transport through sodium nanowires</b>	<b>63</b>
4.1	Introduction . . . . .	63
4.2	Structure of sodium wires . . . . .	66
4.2.1	Infinite wires . . . . .	67
4.2.2	Finite wires . . . . .	68
4.3	Conductance oscillation . . . . .	70
4.3.1	First-principles calculations . . . . .	71
4.3.2	Tight-binding model . . . . .	74
4.4	Stability of conductance oscillation . . . . .	77
4.4.1	Tension/compression of linear wires . . . . .	77
4.4.2	Contact geometry . . . . .	79
4.4.3	Wire geometry: zigzag wires and dimerization . . . . .	81
4.4.4	Optimized geometry . . . . .	83
4.5	Beyond linear response . . . . .	84
4.6	Discussion . . . . .	86
4.7	Summary and Conclusions . . . . .	88
	<b>Appendices</b>	<b>91</b>
<b>A</b>	<b>Appendix to Chapter 2</b>	<b>91</b>
A.1	Velocity matrix . . . . .	91
A.2	Projector matrix . . . . .	92
<b>B</b>	<b>Appendix to Chapter 3</b>	<b>95</b>
B.1	H and B matrices . . . . .	95
B.2	Ideal wire . . . . .	96
B.3	F matrices . . . . .	98
B.4	Scattering problem . . . . .	99
B.5	Velocities . . . . .	100
<b>C</b>	<b>Appendix to Chapter 4</b>	<b>103</b>
C.1	k-point sampling . . . . .	103
	<b>Bibliography</b>	<b>107</b>



<b>CONTENTS</b>	<b>III</b>
<b>Summary</b>	<b>119</b>
<b>Samenvatting</b>	<b>123</b>
<b>Заключение</b>	<b>127</b>
<b>Acknowledgements</b>	<b>131</b>
<b>Curriculum Vitae</b>	<b>133</b>
<b>Publications</b>	<b>135</b>



# Chapter 1

## Introduction

In this Chapter we discuss how the electronic structure and conductance can be calculated for atomic-sized conductors. In Section 1.1 various methods for calculating the electronic structure are debated. A brief overview of density functional theory (DFT) is presented in Section 1.2. Subsequently, all approximations that are used to simplify DFT, are discussed. The pseudopotential method for solving the Kohn-Sham equation is described in Section 1.3. In Section 1.4 we present the basic concepts of the Landauer-Büttiker formalism, and discuss the approximations that are usually made in first-principles conductance calculations for atomic-sized conductors.

### 1.1 Electronic structure methods for atomic-sized conductors

The problem of calculating the electronic structure of atomic-sized conductors is essentially a many-particle problem in which hundreds of electrons and ions have to be treated. The description of many-particle systems is a complicated problem. A lot of effort has been made to tackle it by various theoretical approaches.

Many-body perturbation theory is a very popular method among theoretical physicists because it allows one to make systematic corrections by adding higher order terms of the perturbation expansion [1–5]. This method is especially fruitful when a model Hamiltonian can be found, which captures the most essential physics of the problem. An analytical treatment of the problem may also be possible within this approach. To a certain level of approximation, e.g. the GW approximation [6], many-body perturbation theory can be used in a combination with other approaches to perform *ab-initio* calculations for atoms, molecules and solids [7–9]. But the size of systems that can be treated within such a scheme, is relatively small due to the high computational cost of the calculations.

A number of non-perturbative methods that are not based on any kind of expansions with respect to a small parameter, have been developed [10–15]. The Monte-Carlo and configuration interaction (CI) methods are among the most accurate ones. The CI method [12, 13] is based on a variational procedure and ensures very accurate

results for electronic spectra of single atoms and small molecules, but it turns out to be too expensive for extended systems. In recent years there has also been progress in developing Monte-Carlo methods [14,15] for treating molecular systems and solids. In spite of this progress further development is needed to reduce the computational cost of the calculations, as well as to resolve problems associated with calculating excited states in order to reproduce the entire band structure of solids, for instance.

All the above-mentioned methods deal with the many-particle wave function of the system, which is calculated approximately in different ways by these methods. A completely different approach was proposed by Hohenberg and Kohn [16], who formulated the many-particle problem as a variational problem for the total energy as a functional of the density of electrons. This density functional has a minimum at the exact ground state density. Later Kohn and Sham suggested in Ref. [17] to write the density of electrons as a sum of densities of non-interacting particles. The variational minimum can then be found by solving a set of non-linear equations for these independent particles. It simplifies the many-particle problem considerably. That might explain why density functional theory has become such a popular tool for electronic structure calculations [18]. A drawback of DFT is that the exact form of the density functional is not known and approximations are made to construct a practical form [19]. There is also a fundamental limitation to DFT because it is originally designed as an exact theory of the ground state only. Time-dependent density functional theory (TDDFT) overcomes this limitation [20].

## 1.2 Density functional theory

A system consisting of  $N$  electrons and  $M$  ions can be described by the following Hamiltonian

$$H = \sum_{j=1}^N \left[ -\frac{\hbar^2}{2m} \nabla_j^2 + \frac{1}{2} \sum_{i \neq j}^N \frac{e^2}{|\mathbf{r}_i - \mathbf{r}_j|} + V_{\text{ext}}(\mathbf{r}_j; \{\mathbf{R}_\alpha\}) \right], \quad (1.1)$$

where  $\mathbf{r}_j$  is the position operator of an electron,  $\{\mathbf{R}_\alpha\}$  are the positions of ions,  $1 \leq \alpha \leq M$ . The external potential  $V_{\text{ext}}(\mathbf{r}_j; \{\mathbf{R}_\alpha\})$  contains the information of the electron-ion and ion-ion interactions. We assume that ions are not allowed to move, and the ionic coordinates act as external parameters to the Hamiltonian. The Schrödinger equation

$$H\Psi(\mathbf{r}_1, \dots, \mathbf{r}_N; \{\mathbf{R}_\alpha\}) = E(\{\mathbf{R}_\alpha\}) \Psi(\mathbf{r}_1, \dots, \mathbf{r}_N; \{\mathbf{R}_\alpha\}), \quad (1.2)$$

has to be solved with respect to the many-particle wave function  $\Psi(\mathbf{r}_1, \dots, \mathbf{r}_N; \{\mathbf{R}_\alpha\})$ , which provides us a complete knowledge of the stationary states of the many-particle system. The equilibrium ionic positions can be determined by minimizing the total energy  $E$  of the system, with respect to the ionic coordinates  $\{\mathbf{R}_\alpha\}$ . The phonon spectrum can be obtained using the harmonic approximation for vibrations of the ions around their equilibrium positions. In principle, the full quantum dynamics

of ions could be studied by adding the kinetic energy of ions to the Hamiltonian Eq. (1.1), but that would complicate the problem considerably. The dynamics of ions is often treated classically using Newton's equations [21].

The description of the many-particle system in terms of the wave function  $\Psi$  requires the use of sophisticated computational methods [13]. A completely different approach was proposed by Thomas and Fermi [22, 23]. Their scheme is based on the model of non-interacting electrons and the kinetic energy of an electron is approximated by a local function  $\sim \varrho(\mathbf{r})^{5/3}$ , which results from the free electron model. The electrostatic potential acting on an electron in the system is determined by solving Poisson's equation with the density of electrons  $\varrho(\mathbf{r})$ . By assuming the chemical potential to be constant in the system, the Thomas-Fermi equation can be derived for calculating  $\varrho(\mathbf{r})$ . The total ground state energy is then calculated as an integral over a function that depends upon the local density of the ground state only

$$E = \int d^3\mathbf{r} \varrho(\mathbf{r}) \varepsilon[\varrho(\mathbf{r})]. \quad (1.3)$$

The mathematical meaning of this expression is that the energy is a functional of the density.

### 1.2.1 Hohenberg-Kohn theorem

Following the idea of using a density functional for solving the many-particle problem, Hohenberg and Kohn formulated their famous theorem [16], which turned out to be a milestone in the density functional formalism. If the exact many-particle wave function is known then the density of electrons can be determined as <sup>1</sup>

$$\varrho(\mathbf{r}) = N \int d^3\mathbf{r}_2 \dots \int d^3\mathbf{r}_N |\Psi(\mathbf{r}, \mathbf{r}_2, \dots, \mathbf{r}_N)|^2. \quad (1.4)$$

It is not obvious that the knowledge of the density can provide us with the entire information about the properties of the system. The *Hohenberg-Kohn theorem states* that the energy of the ground state can be defined as an unique functional of the electron density

$$E[\varrho(\mathbf{r})] = F[\varrho(\mathbf{r})] + \int d^3\mathbf{r} \varrho(\mathbf{r}) V_{\text{ext}}(\mathbf{r}). \quad (1.5)$$

If the density functional Eq. (1.5) is minimized, taking into account that the number of electrons is conserved, we obtain the variational equation

$$\frac{\delta}{\delta\varrho(\mathbf{r})} \left\{ F[\varrho(\mathbf{r})] + \int d^3\mathbf{r} \varrho(\mathbf{r}) V_{\text{ext}}(\mathbf{r}) - \mu \int d^3\mathbf{r} \varrho(\mathbf{r}) \right\} = 0, \quad (1.6)$$

where  $\mu$  is a Lagrange multiplier. This equation has to be solved with respect to  $\varrho(\mathbf{r})$  in order to find a minimum of the functional Eq. (1.5). A *second theorem states* that

<sup>1</sup>In order to simplify the notation we omit  $\{\mathbf{R}_\alpha\}$  in all expressions.

the density functional reaches its minimum at the exact ground state density  $\varrho_{\text{GS}}(\mathbf{r})$ , and the total energy of the ground state can be calculated from Eq. (1.5)

$$E = F[\varrho_{\text{GS}}(\mathbf{r})] + \int d^3\mathbf{r} \varrho_{\text{GS}}(\mathbf{r}) V_{\text{ext}}(\mathbf{r}). \quad (1.7)$$

The Hohenberg-Kohn theorems provide us with an exact method for calculating the ground state energy. To describe other ground state properties one has to define density functionals corresponding to these properties. Because the exact expressions for the functionals are not known some approximations are to be assumed in order to construct them.

The *Thomas-Fermi theory* is the simplest example of a density functional based upon the free electron model [18]

$$E^{\text{TF}}[\varrho(\mathbf{r})] = \frac{\hbar^2}{2m} \kappa \int d^3\mathbf{r} \varrho^{5/3}(\mathbf{r}) + \frac{1}{2} e^2 \int d^3\mathbf{r} \int d^3\mathbf{r}' \frac{\varrho(\mathbf{r}) \varrho(\mathbf{r}')}{|\mathbf{r} - \mathbf{r}'|} + \int d^3\mathbf{r} \varrho(\mathbf{r}) V_{\text{ext}}(\mathbf{r}), \quad (1.8)$$

where the first and second terms are related to the kinetic energy of electrons and the electrostatic energy of the electron-electron interaction respectively,  $\kappa = 3(3\pi^2)^{2/3}/5$ ; the last term is related to an external potential. For instance, the external potential for a single atom is equal to the ionic potential  $V_{\text{ext}}(\mathbf{r}) = -Ne^2/r$ .

From Eq. (1.6) and Eq. (1.8) a variational equation can be derived

$$\frac{5}{3} \frac{\hbar^2}{2m} \kappa \varrho^{2/3}(\mathbf{r}) + e^2 \int d^3\mathbf{r}' \frac{\varrho(\mathbf{r}')}{|\mathbf{r} - \mathbf{r}'|} + V_{\text{ext}}(\mathbf{r}) = \mu, \quad (1.9)$$

where  $\mu$  is the chemical potential of the system. This equation is equivalent to the Thomas-Fermi equation [24]. The Eq. (1.9) must be solved with respect to the electron density  $\varrho(\mathbf{r})$  and then the total energy is calculated from Eq. (1.8). If the external potential is chosen as  $V_{\text{ext}}(\mathbf{r}) = -Ne^2/r$  then the Thomas-Fermi equation provides an asymptotically exact solution for Eq. (1.1) in the limit of  $N \gg 1$  [25], and the total energy has the analytical form  $E = -20.8 N^{7/3}$  eV.

## 1.2.2 Kohn-Sham equation

The density functional for the kinetic energy in Eq. (1.8) is not exact. The approximate treatment of the kinetic energy within the framework of the Thomas-Fermi theory gives rise to many problems [18], which are resolved to a certain extent by correcting density functional of the kinetic energy.

To avoid these difficulties Kohn and Sham suggested to represent the density functional Eq. (1.5) as a sum of four terms [17]

$$E[\varrho(\mathbf{r})] = T_0[\varrho(\mathbf{r})] + \frac{1}{2} e^2 \int d^3\mathbf{r} \int d^3\mathbf{r}' \frac{\varrho(\mathbf{r}) \varrho(\mathbf{r}')}{|\mathbf{r} - \mathbf{r}'|} + E_{\text{xc}}[\varrho(\mathbf{r})] + \int d^3\mathbf{r} \varrho(\mathbf{r}) V_{\text{ext}}(\mathbf{r}), \quad (1.10)$$

where  $T_0[\varrho(\mathbf{r})]$  is the exact kinetic energy of a auxiliary system of non-interacting particles with the density  $\varrho(\mathbf{r})$ , which is equal to the density of the real system of

interacting electrons; the second term is the electrostatic energy of electrons, and  $E_{\text{xc}} = E_{\text{x}} + E_{\text{c}}$  is a sum of the exchange and correlation energies. The advantage of this approach is that in Eq. (1.10) all terms except for the correlation energy  $E_{\text{c}}$  can be derived exactly. The contribution of the correlation energy is relatively small, but important in many cases [18]. The approximate form of  $E_{\text{xc}}$  that is used in our calculations, will be discussed in Section 1.2.3.

The variational equation for the density functional of Eq. (1.10) is

$$\frac{\delta T_0[\varrho(\mathbf{r})]}{\delta \varrho(\mathbf{r})} + e^2 \int d^3\mathbf{r}' \frac{\varrho(\mathbf{r}')}{|\mathbf{r} - \mathbf{r}'|} + \frac{\delta E_{\text{xc}}[\varrho(\mathbf{r})]}{\delta \varrho(\mathbf{r})} + V_{\text{ext}}(\mathbf{r}) = \mu. \quad (1.11)$$

If we define the density of electrons as a sum over densities of a system of non-interacting particles, described by single-particle wave functions  $\psi_j$ ,

$$\varrho(\mathbf{r}) = \sum_{j=1}^N |\psi_j(\mathbf{r})|^2, \quad (1.12)$$

then the solution of Eq. (1.11) can be obtained by solving equations for  $N$  non-interacting particles,

$$\left[ -\frac{\hbar^2}{2m} \nabla^2 + e^2 \int d^3\mathbf{r}' \frac{\varrho(\mathbf{r}')}{|\mathbf{r} - \mathbf{r}'|} + \frac{\delta E_{\text{xc}}[\varrho(\mathbf{r})]}{\delta \varrho(\mathbf{r})} + V_{\text{ext}}(\mathbf{r}) \right] \psi_j(\mathbf{r}) = \epsilon_j \psi_j(\mathbf{r}). \quad (1.13)$$

The system of equations Eq. (1.12) and Eq. (1.13) is called the Kohn-Sham equations and has to be solved self-consistently. Its solution corresponds to the exact ground state of the many-particle system considered.

The *Kohn-Sham formulation* of the density functional theory is very efficient from the computational point of view because the problem for interacting electrons can be reduced to the equivalent problem for non-interacting particles. The effective single-particle potential in Eq. (1.13)

$$V_{\text{eff}}(\mathbf{r}) = e^2 \int d^3\mathbf{r}' \frac{\varrho(\mathbf{r}')}{|\mathbf{r} - \mathbf{r}'|} + \frac{\delta E_{\text{xc}}[\varrho(\mathbf{r})]}{\delta \varrho(\mathbf{r})} + V_{\text{ext}}(\mathbf{r}), \quad (1.14)$$

is local so solving the Kohn-Sham equations is no more complicated than solving the Hartree equations.

### 1.2.3 Density functionals: local-density approximation

The Kohn-Sham approach provides an exact method for treating any correlated many-particle problem given by Eq. (1.2). Because the exact expression for the density functional is not known, an approximate functional must be found, which is suitable for describing a great number of systems.

The exact functional does not depend on the details of a particular system. To construct a functional sophisticated numerical calculations have to be performed for some model system, e.g. the homogeneous gas of interacting electrons imbedded in

a positively charged background [26]. The homogeneous gas has a constant density of electrons  $\varrho$ , the exchange-correlation energy per electron  $\varepsilon_{\text{xc}}(\varrho)$  is determined as a function of  $\varrho$ . The local-density approximation (LDA) is often used to simplify the exchange-correlation functional  $E_{\text{xc}}$  for inhomogeneous systems. LDA for a finite system with density  $\varrho(\mathbf{r})$  assumes that the local exchange-correlation energy  $\varepsilon_{\text{xc}}(\varrho(\mathbf{r}))$  must be equal to the energy  $\varepsilon_{\text{xc}}(\varrho)$  for the model system with the density  $\varrho = \varrho(\mathbf{r})$

$$E_{\text{xc}}^{\text{LDA}} = \int d^3\mathbf{r} \varrho(\mathbf{r}) \varepsilon_{\text{xc}}(\varrho(\mathbf{r})). \quad (1.15)$$

The contribution of the local exchange energy within the LDA was derived by Dirac [27]

$$E_{\text{x}}^{\text{LDA}} = -\frac{3}{4} \left(\frac{3}{\pi}\right)^{1/3} e^2 \int d^3\mathbf{r} [\varrho(\mathbf{r})]^{4/3}. \quad (1.16)$$

There are a few schemes for parameterizing the correlation energy functional. The simplest one was proposed by Wigner [5, 28]

$$\varepsilon_c^{\text{W}}(\varrho) = -\frac{0.44}{r_s(\varrho) + 7.8}, \quad (1.17)$$

where  $r_s(\varrho) = (3/4\pi\varrho)^{1/3}$  is the electronic Wigner-Seitz radius.<sup>2</sup> Wigner performed approximate calculations for high- and low densities of the homogenous gas of interacting electrons and constructed the interpolation formula, which would fit the correlation energy in the intermediate region.

To construct a good interpolation formula Ceperley and Alder [26] performed state-of-the art Monte-Carlo simulations in order to find an exact numerical solution for the interacting electron gas. Perdew and Zunger [19] made use of this result and interpolated the correlation energy. Their resulting formula is

$$\begin{aligned} \varepsilon_c(\varrho) &= \frac{-0.1432}{1 + 1.0529\sqrt{r_s(\varrho)} + 0.3334r_s(\varrho)} && \text{for } r_s \geq 1 \\ &= -0.0480 + 0.0311 \ln r_s(\varrho) - 0.0116 r_s(\varrho) \\ &\quad + 0.0020 r_s(\varrho) \ln r_s(\varrho) && \text{for } r_s < 1. \end{aligned} \quad (1.18)$$

The Perdew-Zunger expression Eq. (1.18) has proved to provide accurate results for the electronic structure of numerous systems, and we also make use of it in our calculations.<sup>3</sup>

### 1.3 Pseudopotential method

There are various self-consistent schemes [18, 30] for solving the Kohn-Sham equation Eq. (1.13). A common procedure for finding the solution assumes that we have to

<sup>2</sup> $e_c^{\text{W}}$  in energy atomic units (Hartree), where 1 Hartree is equal to 27.21 eV.

<sup>3</sup>Generalized gradient approximation (GGA) [29] is used instead of LDA for performing geometry optimizations in Chapter 4.



represent the Kohn-Sham equation and one-electron wave functions on some basis set [31–35]. Various methods based on the real-space discretization techniques [36] such as finite-difference [37, 38], finite-elements and wavelets [39], have been also proposed. These methods provide a solution of the Kohn-Sham equation on a real-space grid, not requiring the use of a basis set explicitly.

In principle, the exact solution does not depend on a particular choice of the basis set if it is complete. In practice, a basis set is always terminated, and that leads to an approximate solution, which must be converged with respect to the size of the basis set. The number of basis functions defines the dimension of the entire problem.

We can separate basis sets into two major groups: localized atomic orbitals and plane waves. It is also possible to construct a mix of these two. A localized atomic orbital basis is usually relatively small and very suitable for describing nearly localized core electrons. On the contrary, valence electrons can be nearly free, and it is easier to describe them with the plane waves. The choice of the basis set can also depend on what kind of materials is investigated, e.g. insulators or metals.

The formulation of the plane-wave formalism is rather simple [30, 31, 40], but it requires some extra approximations in order to be computationally practical. The same is also true for a real-space finite-difference approach. To describe core electrons within these formalisms one has to use the pseudopotential approach [41–49], which replaces the potential of the nuclei and the core electrons acting on the valence electrons by an effective potential, called a pseudopotential. Pseudopotentials allow us to treat the Kohn-Sham equation for valence electrons only. Pseudopotentials are constructed in such a way that they are much smoother than the original all electron potentials. That reduces the dimension of the plane-wave basis set or the number of real-space grid points considerably. At present, the plane-wave formalism is one of the basic tools for calculating the total energy and its derivatives with respect to structural degrees of freedom (ionic coordinates). It allows one to perform structural relaxation and molecular dynamics simulations in a simple way [21, 30].

In this Section we show how to represent the Kohn-Sham equation both on a plane-wave basis and on a real-space grid, using the pseudopotential method.

### 1.3.1 Plane-wave basis set

The Kohn-Sham equation within the pseudopotential approach has the following form<sup>4</sup>

$$\left[ -\frac{1}{2}\nabla^2 + \int d^3\mathbf{r}' \frac{\varrho(\mathbf{r}')}{|\mathbf{r} - \mathbf{r}'|} + V_{xc}(\varrho(\mathbf{r})) + \sum_{\mu} \hat{V}_{ps}(\mathbf{r} - \mathbf{R}_{\mu}) \right] \psi_j(\mathbf{r}) = \epsilon_j \psi(\mathbf{r}), \quad (1.19)$$

where  $\psi_j$  is the wave function,  $j$  is the quantum number, which runs over all occupied states,  $\mathbf{R}_{\mu}$  is a lattice vector;  $\varrho(\mathbf{r}) = \sum_j \psi_j^*(\mathbf{r})\psi_j(\mathbf{r})$  is the density of valence electrons,  $V_{xc} = \delta E_{xc}[\varrho]/\delta\varrho$  is the exchange-correlation potential; the pseudopotential

<sup>4</sup>Atomic units  $e = \hbar = m_e = 1$  will be used in all equations of this section.

$\hat{V}_{\text{ps}}$  describing the effect of core electrons and ions has the form

$$\hat{V}_{\text{ps}}(\mathbf{r} - \mathbf{R}_\mu) = \sum_{\alpha} V_{\text{loc}}^{\alpha}(|\mathbf{r} - \mathbf{R}_\mu|) + \sum_{\alpha} \sum_l \delta V_l^{\alpha}(|\mathbf{r} - \mathbf{R}_\mu|) \hat{P}_l, \quad (1.20)$$

where  $\alpha$  runs over all atoms in the unit cell (supercell),  $V_{\text{loc}}^{\alpha}(\mathbf{r})$  is the local part of the pseudopotential,  $\delta V_l^{\alpha}(|\mathbf{r} - \mathbf{R}_\alpha|)$  is  $l$ -th component of the non-local pseudopotential;  $\hat{P}_l$  is the projector operator on angular momentum  $l$ . The non-local pseudopotential is a short range potential with a range that is smaller than the interatomic distance. All components of the pseudopotential are constructed as smooth functions without nodes. At present, there are a few commonly used types of pseudopotential which can be divided into two major groups: norm-conserving [43–45] and ultrasoft [46–49]. The ultrasoft pseudopotentials require a smaller plane-wave basis set because they are smoother than the norm-conserving ones, but the implementation of these pseudopotentials is rather complicated so we use norm-conserving Troullier-Martins pseudopotentials [45] in most of the calculations.

The use of plane-wave functions assumes periodic boundary conditions, which can be easily exploited in the case of crystalline structures, where the one-electron potential is periodic. Calculations for atoms, molecules and atomic clusters can be performed using a supercell. After introducing periodicity in the system a plane wave expansion (Fourier series) of the wave function can be made

$$\psi_{n,\mathbf{k}}(\mathbf{r}) = \sum_{\mathbf{g}} c_{n,\mathbf{g}+\mathbf{k}} e^{i(\mathbf{g}+\mathbf{k})\cdot\mathbf{r}}, \quad (1.21)$$

where  $\mathbf{g}$  is the reciprocal lattice vector,  $n$  and  $\mathbf{k}$  are the band index and the wave vector in the Brillouin zone, respectively;  $c_{n,\mathbf{g}+\mathbf{k}}$  are the coefficients of the Fourier series. These coefficients can be interpreted as a wave function in the reciprocal space. Using Eq. (1.21) the Kohn-Sham equation Eq. (1.19) is written in plane-wave representation as [31, 40]

$$\sum_{\mathbf{g}'} \left[ \frac{1}{2}(\mathbf{k} + \mathbf{g}')^2 \delta_{\mathbf{g},\mathbf{g}'} + V_{\mathbf{g},\mathbf{g}'} \right] c_{n,\mathbf{k}+\mathbf{g}'} = \epsilon_{n,\mathbf{k}} c_{n,\mathbf{k}+\mathbf{g}'}. \quad (1.22)$$

The Fourier components  $V_{\mathbf{g},\mathbf{g}'}$  of the total one-electron potential of Eq. (1.19) are

$$\begin{aligned} V_{\mathbf{g},\mathbf{g}'} &= V_{\text{H}}(\mathbf{g} - \mathbf{g}') + V_{\text{xc}}(\mathbf{g} - \mathbf{g}') + \sum_{\mu} \frac{e^{i(\mathbf{g}' - \mathbf{g})\cdot\mathbf{R}_{\mu}}}{N_{\text{t}}} \left[ \sum_{\alpha} V_{\text{loc}}^{\alpha}(\mathbf{g} - \mathbf{g}') \right. \\ &\quad \left. + \sum_{\alpha} \sum_l \delta V_l^{\alpha}(\mathbf{k} + \mathbf{g}, \mathbf{k} + \mathbf{g}') \right], \end{aligned} \quad (1.23)$$

where  $N_{\text{t}}$  is the total number of unit cells in the system,  $V_{\text{H}}(\mathbf{g}) = 4\pi\rho(\mathbf{g})/\mathbf{g}^2$  is the interelectronic Coulomb potential (Hartree potential);  $\rho(\mathbf{g})$ ,  $V_{\text{xc}}(\mathbf{g})$ ,  $V_{\text{loc}}^{\alpha}(\mathbf{g})$  and

$\delta V_l^\alpha(\mathbf{k} + \mathbf{g}, \mathbf{k} + \mathbf{g}')$  are the Fourier components of the electron density and the corresponding potentials of Eq. (1.19). The angular component of the non-local pseudopotential is

$$\delta V_l^\alpha(\mathbf{k} + \mathbf{g}, \mathbf{k} + \mathbf{g}') = \frac{4\pi(2l+1)}{\Omega} P_l(\cos \gamma) \int_0^\infty dr r^2 \delta V_l^\alpha(r) j_l(|\mathbf{k} + \mathbf{g}|) j_l(|\mathbf{k} + \mathbf{g}'|), \quad (1.24)$$

where  $\Omega$  is the unit cell (supercell) volume;  $j_l$  and  $P_l$  are spherical Bessel functions and Legendre polynomials, respectively, and  $\gamma$  is

$$\cos \gamma = \frac{(\mathbf{k} + \mathbf{g}) \cdot (\mathbf{k} + \mathbf{g}')}{|\mathbf{k} + \mathbf{g}| |\mathbf{k} + \mathbf{g}'|}.$$

If the non-local part of the pseudopotential Eq. (1.20) is used in a fully separable form suggested in Ref. [42], then the non-local pseudopotential has the form

$$\begin{aligned} \delta V_l^\alpha(\mathbf{k} + \mathbf{g}, \mathbf{k} + \mathbf{g}') &= \frac{1}{\Omega \langle \phi_l^\alpha | \delta V_l^\alpha(r) | \phi_l^\alpha \rangle} \int_0^\infty dr r^2 \phi_l^\alpha(r) \delta V_l^\alpha(r) j_l(|\mathbf{k} + \mathbf{g}| r) \\ &\times \int_0^\infty dr' r'^2 \phi_l^\alpha(r') \delta V_l^\alpha(r') j_l(|\mathbf{k} + \mathbf{g}'| r') \sum_{m=-l}^l Y_{lm}(\hat{\mathbf{q}}) Y_{lm}^*(\hat{\mathbf{q}}'), \end{aligned} \quad (1.25)$$

where  $Y_{lm}(\hat{\mathbf{q}})$  are the spherical harmonics;  $\hat{\mathbf{q}} = (\mathbf{k} + \mathbf{g})/|\mathbf{k} + \mathbf{g}|$  and  $\hat{\mathbf{q}}' = (\mathbf{k} + \mathbf{g}')/|\mathbf{k} + \mathbf{g}'|$ ;  $\phi_l^\alpha(r)$  is a radial part of a pseudo-wave function that is related to the  $l$ -component of the pseudopotential  $V_l^\alpha$  for  $\alpha$ -th atom. Such a form of the pseudopotential allows to speed up computations considerably.

The system of linear equations of Eq. (1.22) is a matrix representation of the Kohn-Sham equation. According to conventional numerical schemes for treating non-linear equations the matrix Kohn-Sham equation can be solved by matrix diagonalization with respect to  $c_{n,\mathbf{k}+\mathbf{g}}$  and  $\epsilon_{n,\mathbf{k}}$ . A large-scale eigenvalue problem has to be solved which scales as  $M^3$  with respect to the number of plane-wave functions used. There are approaches that allow one to deal only with the lowest  $N$  eigenstates [50] needed to construct the electron density. The computational cost of such diagonalization techniques is  $O(N^2M)$  for very large systems. A completely different method has been proposed by Car and Parrinello in Ref. [21], based on a molecular-dynamics (MD) simulation which allows to achieve self-consistency and diagonalization simultaneously. Moreover, the MD approach provides a total energy optimization with respect to the electronic and ionic degrees of freedom. This algorithm scales with size of the system as  $O(N^2M)$ , but the actual computational cost depends highly on a particular implementation. The original MD method was based on a simulated annealing-like approach [51], which allowed to search for a global minimum of the total energy. If the ions are not allowed to move this minimization scheme is too expensive because in this case usually a single minimum exists. The steepest descent (SD) approach [52] was found to improve the efficiency considerably, but it still has various drawbacks. There is an efficient robust method, which overcomes the drawbacks of the previously mentioned techniques. It is based on the conjugate

gradient minimization method [53, 54]. For low-symmetry systems this method is computationally efficient as compared with the SD and MD approaches because it reduces the computational cost by an order of magnitude [30, 54]. It also does not need the use of any convergence parameter like the integration time step in the SD method.

The plane-wave pseudopotential method [31, 45, 55] is used for calculating the electronic structure of the atomic-sized conductors considered in this thesis.

### 1.3.2 Real-space finite-difference representation

An alternative way for solving the Kohn-Sham equation is based on the finite-difference method [36, 37]. The plane-wave and finite-difference methods are closely related. Both approaches are equally computationally efficient for slowly varying wave functions and require the use of pseudopotentials. There are two advantages of a finite-difference representation of the Kohn-Sham equation. Firstly, the implementation of this technique is relatively simple and straightforward [37, 56] if a uniform grid is used. The accuracy of the calculations can easily be controlled by changing the grid spacing. Secondly, the finite-difference scheme allows one to avoid using a periodic supercell for treating finite systems like atoms, molecules and clusters. That can be done by placing hard walls around the finite system considered. In general, arbitrary boundary conditions can be imposed upon the system within the framework of a real-space finite-difference approach.

The simplest finite-difference representation of the Kohn-Sham equation Eq. (1.19) can be based on the well-known first-order approximation of the second derivative

$$\frac{\partial^2 \psi(x_i, y_j, z_k)}{\partial^2 x} \approx \frac{1}{h^2} [\psi(x_{i-1}, y_j, z_k) - 2\psi(x_i, y_j, z_k) + \psi(x_{i+1}, y_j, z_k)], \quad (1.26)$$

where the grid points are defined as  $x_i = x_0 + i h$ ,  $y_j = y_0 + j h$  and  $z_i = z_0 + k h$ ; indices  $i, j, k$  run over integer values;  $h$  is the grid spacing. Similar expressions can be derived for partial derivatives of  $\psi$  with respect to  $y$  and  $z$ . The electrostatic Hartree potential  $V_H(x, y, z)$ , the exchange-correlation potential  $V_{xc}(x, y, z)$  and the local pseudopotential  $V_{loc}^\alpha(x, y, z)$  are replaced by  $V_H(x_i, y_j, z_k)$ ,  $V_{xc}(x_i, y_j, z_k)$  and  $V_{loc}^\alpha(x_i, y_j, z_k)$ , respectively.

The fully separable non-local pseudopotential of Eq. (1.20) represented on the real-space grid has the form

$$\delta V_l^\alpha(x_i, y_j, z_k) \hat{P}_l \psi(x_i, y_j, z_k) = \sum_{m=-l}^l \phi_{lm}^\alpha(x_i, y_j, z_k) \delta V_l^\alpha(x_i, y_j, z_k) W_{lm}^\alpha, \quad (1.27)$$

where

$$W_{lm}^\alpha = \frac{\sum_{i', j', k'} \phi_{lm}^\alpha(x_{i'}, y_{j'}, z_{k'}) \delta V_l^\alpha(x_{i'}, y_{j'}, z_{k'}) \psi(x_{i'}, y_{j'}, z_{k'}) h^3}{\sum_{i'', j'', k''} \phi_{lm}^\alpha(x_{i''}, y_{j''}, z_{k''}) \delta V_l^\alpha(x_{i''}, y_{j''}, z_{k''}) \phi_{lm}^\alpha(x_{i''}, y_{j''}, z_{k''}) h^3}, \quad (1.28)$$

and  $\phi_{lm}^\alpha$  is a pseudo-wave function that is related to the  $lm$ -component of the pseudopotential  $V_{lm}^\alpha$  for  $\alpha$ -th atom. The sums in Eq. (1.28) arises from the approximate integration of the non-local pseudopotential on the uniform grid. The

summation in Eq. (1.28) is taken over the grid points in the unit cell and its nearest neighbor cells because  $\delta V_{lm}^\alpha(\mathbf{r})$  is a short-range function.

Combining all the terms we can write the Kohn-Sham equation as a matrix equation

$$\begin{aligned}
& -\frac{1}{2} \sum_{n=-N}^N c_n [\psi(x_{i+n}, y_j, z_k) + \psi(x_i, y_{j+n}, z_k) + \psi(x_i, y_j, z_{k+n})] \\
& + [V_H(x_i, y_j, z_k) + V_{xc}(x_i, y_j, z_k) + \sum_{\alpha} V_{loc}^\alpha(x_i, y_j, z_k)] \psi(x_i, y_j, z_k) \\
& + \sum_{\alpha} \sum_l \sum_{m=-l}^l \phi_{lm}^\alpha(x_i, y_j, z_k) \delta V_l^\alpha(x_i, y_j, z_k) W_{lm}^\alpha = \epsilon \psi(x_i, y_j, z_k), \quad (1.29)
\end{aligned}$$

where  $\alpha$  runs over all atoms in the system;  $c_n$  are equal to  $c_0 = -2$  and  $c_1 = c_{-1} = 1$  for the first-order approximation of the second derivative. The high-order approximations  $N > 1$  are commonly used in realistic calculations to provide a faster convergence of the total energy of the system considered [37]. The high sparsity of the Hamiltonian matrix in Eq. (1.29) allows one to solve the matrix eigenvalue problem using an iterative sparse matrix technique [57]. Application of this real-space method to localized systems was first conducted in Refs. [37, 56]. The generalization of this formalism to the extended periodical systems has been recently developed in Refs. [58, 59]. A more accurate double-grid approximation for the non-local pseudopotential was also proposed in Ref. [38]. A high-order finite-difference approach for treating the electronic transport will be considered in Chapter 3. A brief review on real-space methods such as finite-difference, finite elements and wavelets applied to electronic structure calculations and to the electronic transport problem, can be found in Ref. [39].

## 1.4 Electronic transport

This section is devoted to a general discussion of the electronic transport for small conductors. A brief overview of the Landauer-Büttiker formalism is given for the coherent electronic transport problem. Approximations used to simplify first-principles conductance calculations within a general theory of electronic transport are discussed.

### 1.4.1 Landauer-Büttiker formalism

It is well-known that the conductance of a macroscopic conductor is described by Ohm's law

$$G = \sigma \frac{A}{L}, \quad (1.30)$$

where  $A$  is the area of the cross section of the conductor,  $L$  is the length of the conductor, and  $\sigma$  is its conductivity. According to this law the conductance should vanish as the conductor gets narrower and  $A \rightarrow 0$ , and it becomes infinite for very

short conductors,  $L \rightarrow 0$ . This behavior relies on the assumption that the conductivity does not depend on the size of the conductor because it is a macroscopically defined quantity, which is assumed to be homogenous over the conductor. If the size of the conductor reaches the atomic scale then the homogeneity of the conductivity is violated, and Ohm's law must break down. The failure of Ohm's law was indeed seen in experiments on the quantum point contact [60] and atomic-sized wires [61], where a stair-case behavior of the conductance was observed during narrowing of the point contact and elongation of the wire, respectively.

An important issue is to define the characteristic size of the conductor when the macroscopic description is no longer applicable. There are three length scales that are important in determining this size [62]: (i) the *de Broglie wavelength* that is related to the kinetic energy of the electrons, (ii) the *mean free path*, which is the average distance that an electron passes without changing its momentum, e.g. such events occur because scattering on impurities, and (iii) the *phase-relaxation length*, which is the average distance that an electron passes without destroying its phase. Phase loss takes place due to inelastic scattering caused by the electron-electron and electron-phonon interactions. A conductor usually exhibits ohmic behavior if its size is much larger than any of these length scales. The characteristic lengths depend on the material considered, and they can be affected by temperature or magnetic field. If the dimensions of the conductor is intermediate between microscopic and macroscopic then it is called a mesoscopic conductor having a size of tens or hundreds nanometers. Microscopic conductors have nanometer dimensions, and are often called atomic-sized conductors, see Fig. 1.1. Because the phase-relaxation length in the mesoscopic and atomic-scaled conductors is larger than their dimensions, the electronic transport can be treated as coherent. The latter means that a full quantum-mechanical treatment is required for an adequate description of the electron propagation in such conductors. In this thesis we develop a computational technique that can be used for solving the electronic coherent transport problem in mesoscopic and atomic-sized conductors.

A quantum-mechanical formulation of the electronic transport through small conductors was first proposed by Landauer [63,64], who suggested a simple formula which established the relation between the transmission probability of the electron and the electronic conductance in one-dimensional conductors. Landauer's idea was generalized by Fisher and Lee [65] for multi-channel three-dimensional conductors, using the linear response formalism.<sup>5</sup> Büttiker [67,68] proposed a multi-channel Landauer formula for multi-probe devices, and a derivation of this formula was later given by Stone and Szafer [69] based upon linear response theory. They also provided a general discussion of different versions of Landauer's formula present in the literature at that time. An introduction to the Landauer-Büttiker formalism can be found in Ref. [62], where also the relation between different approaches such as the Kubo, the Green's function and the Landauer-Büttiker formalisms is discussed. In the Chapter 2 we present a comprehensive study on the relation between the Green's function formalism and the Landauer-Büttiker formalism based on the mode-matching technique.

---

<sup>5</sup>The linear response formalism was first applied for deriving Landauer's formula for a one-dimensional conductor by Economou and Soukoulis [66].

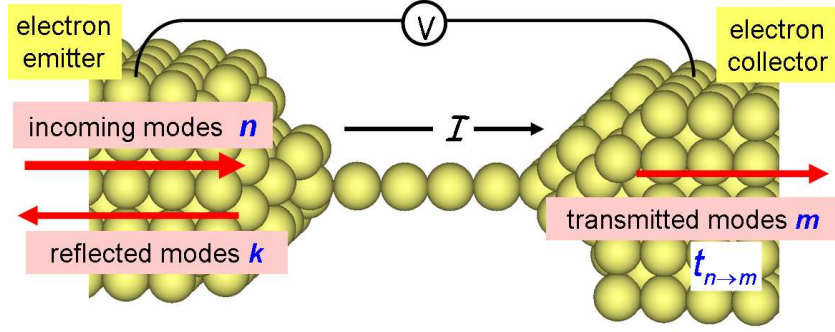


**Figure 1.1** : An atomic wire is an example of a two-probe atomic-sized device. An electron coming in from the left lead is partially transmitted through the wire into the right lead. The electron transmission is described by quantum-mechanical transmission probability amplitudes  $t_{n,m}$ , which is calculated at the Fermi level if the applied voltage  $V$  is small. The conductance of the wire  $G = dI/dV$  can be expressed in terms of the normalized transmission probability amplitudes  $t_{n,m}$  by the Landauer-Büttiker formula Eq. (1.31).

The latter is used in our conductance calculations [70, 71].

Reformulating what was said in the previous paragraph, the Landauer-Büttiker formalism is based on a quantum-mechanical scattering approach for calculating the electronic conductance in small devices. In this thesis we focus on two-probe devices as shown in Fig. 1.1. The Landauer-Büttiker formula for a two-probe device

$$G = \frac{2e^2}{h} \sum_{n,m} |t_{n,m}|^2, \quad (1.31)$$

expresses the conductance  $G = dI/dV$  as a sum over the normalized transmission probability amplitudes  $t_{n,m}$  between all right-going modes  $n$  and  $m$  in the left and right leads, respectively. The factor of 2 in the Eq. (1.31) takes account of the spin degeneracy of the electrons. If the conductor is attached to semi-infinite ideal crystalline leads then the modes are described by Bloch functions. The latter are just plane waves in the case of jellium leads, which are commonly used for modeling the metallic electrodes. Note that only the electrons at the Fermi energy  $E_F$  contribute to the current in the linear response regime, when the applied voltage  $V$  is small [62]. The applied bias  $V$  is assumed to be equal to the difference  $\Delta\mu = \mu_L - \mu_R$  in the chemical potentials of the left and right macroscopic electrodes.

We would like to emphasize that the Landauer-Büttiker formalism relies upon a single-particle picture of the electronic transport, i.e. the electrons are considered to be non-interacting. Nevertheless, the electron-electron interaction can be partially taken into account within a mean field approach. In this case the transmission

amplitudes are calculated from a single particle equation

$$\left[ -\frac{\hbar^2}{2m} \nabla^2 + V_{\text{eff}}(\mathbf{r}) - E_F \right] \psi(\mathbf{r}) = 0, \quad (1.32)$$

where the effective potential  $V_{\text{eff}}(\mathbf{r})$  represents the interaction of an electron with some average field of other electrons and nuclei. The choice of the mean field potential  $V_{\text{eff}}$  is not unique, and this problem will be discussed below in detail.

### 1.4.2 Electronic structure methods for conductance calculations

So far we have separately discussed various methods for describing the electronic structure of the conductors and the Landauer-Büttiker formalism for calculating the conductance. To study electronic transport from first-principles an electronic structure method has to be merged with a method for conductance calculations, e.g. the Landauer-Büttiker formalism. In principle, there is a general theory, based on either Keldysh's formalism [72–74] or the Kadanoff-Baym formalism [72], that can be used for describing both the electronic structure of the system and the electronic transport. Both approaches make use of the non-equilibrium Green's function technique taking into account the elastic and inelastic processes during the electron propagation through the conductor. The implementation of these methods within a first-principles approach is an extremely challenging problem, which can not proceed without simplifying approximations. If we are interested in electronic transport at low temperature and apply a small voltage to the electrodes, then the effect of inelastic scattering processes due to the electron-phonon and electron-electron interactions can be neglected provided the dimensions of the conductor are smaller than the phase-relaxation length. The electric current can be assumed time-independent as soon as the regime of a steady-state current is reached. This regime reflects the experimental conditions, and simplifies the problem considerably. At this level of approximation the transport problem is still rather complicated because of the electron-electron interaction. A crucial simplification is the use of a mean field approximation which leads to single particle Hartree-Fock equations for the electrons. The conductance can be then calculated using Caroli's formula [75] which represents the conductance in terms of the Green's functions. The Landauer-Büttiker formula Eq. (1.31) was shown to be identical to Caroli's formula [71, 76]. At this point the use of either the Landauer-Büttiker formalism or the non-equilibrium Green's function approach becomes a matter of taste. The relation between the Green's function approach and the mode-matching approach, which we use as a general technique in our transport calculations, will be demonstrated in Chapter 2.

Let us discuss the mean field approximation in more detail. The Hartree-Fock mean field potential consists of three parts: (a) the local potential of all nuclei, (b) the local Hartree potential, and (c) the non-local exchange potential. The non-locality of the Hartree-Fock exchange potential has a long range, which does not create a problem for localized systems like atoms and molecules, but it can lead to artifacts in an infinite solid. For instance, the Hartree-Fock method applied to the homogenous electron gas predicts that the density of states at the Fermi energy is



zero [77], and that would lead to zero conductance. This prediction is obviously wrong because the homogenous electron gas exhibits a metallic behavior if one performs more accurate calculations. The Hartree-Fock method also predicts unphysically large band gaps in insulators (sometimes by a factor of 2-5) [78]. A correction to the Hartree-Fock approach can be done by using the GW-approximation, which takes into account electron-electron correlation. The correlation interaction reduces the range of the exchange potential by accounting for the electron screening in solids. The GW method is rather expensive computationally, and so far it has been used in transport calculations on model systems only [79].

Any many-body correlation correction to the Hartree-Fock mean field potential would reduce the computational efficiency considerably. As we emphasize in Section 1.1 one of the most popular methods for calculating the electronic structure is based on the density functional formalism and uses the LDA approximation. The formulation of DFT-LDA in terms of non-interacting particles provides a local potential which contains the nuclear potential, the Hartree potential and the local exchange-correlation potential. In contrast to the Hartree-Fock approach DFT deals with a local mean field potential which also contains the correlation potential. The Landauer-Büttiker formalism can be then used for calculating the conductance in terms of the transmission amplitudes obtained from the single particle equation Eq. (1.32) with the effective DFT potential  $V_{\text{eff}}$  given by Eq. (1.14). In Chapter 3 we present our implementation of the first-principles approach for treating the electronic transport, based on the finite-difference representation of the Kohn-Sham equation. The application of this method to calculate the conductance in sodium nanowires is given in Chapter 4.

There has been a discussion in the last couple of years on how good ground state DFT is for describing electronic transport. The argument is that a description of electronic transport requires calculating excited states of the system, and that is beyond the scope of static or ground state DFT. First of all, if coherent electronic transport is treated in the linear response regime, one can assume that the single particle potential of the ground state, obtained from DFT, is not changed by the transported electrons. It is well-known from electronic structure calculations on bulk materials and surfaces that the DFT potential provides fairly good approximations of quasi-particle wave functions, band structures and Fermi surfaces, even within LDA. However, there is a problem of predicting the band gap in insulating solids and the HOMO-LUMO gap in molecules. DFT-LDA usually underestimates this minimum energy gap between hole and electron excitations (by a factor of 2). For instance, if a tunnel junction is formed by a semiconducting heterojunction or an organic molecule then the band gap is a crucial quantity to define the tunneling barrier, charge transfer and band alignment. All these quantities strongly affect the electronic transport. We do not expect this gap problem to play a role for metallic systems, e.g. for the electronic transport through metallic wires considered in Chapter 4. The conductance calculations for insulators/semiconductors and molecules can be affected by this problem, and the results must be treated with care.

There is a generalization of ground state DFT, so-called time-dependent density functional theory [20, 79], which overcomes the drawbacks of DFT, and provides an

exact solution to the transport problem, in principle. This formalism will have success as soon as a good functional is found. A recent development within TDDFT was a proof that LDA within DFT is equivalent to the adiabatic local density approximation (ALDA) within TDDFT [79]. So we might say that DFT-LDA has found its place in the exact transport approach. Some exchange-correlation corrections to the ALDA have been also proposed recently [80], based on time-dependent current-density functional theory. These corrections demonstrated decrease of the conductance due to dynamical exchange-correlation effects. The correction to the conductance obtained from DFT-LDA is 2% and 11% for atomic gold wires and for a molecular junction, respectively. Note that these corrections are not large even for the molecule because the present disagreement between the theoretical and experimental results on the conductance of molecular junctions is several order of magnitude.<sup>6</sup> Fortunately, there is considerably better agreement for atomic wires [61]. In Chapter 4 we conduct an investigation of the even-odd conductance oscillation in monatomic wires, which was observed experimentally [82].

Finally, let us discuss briefly how we can treat the electronic transport beyond the linear response regime. The current-voltage characteristic can be also calculated within the framework of the Landauer-Büttiker formalism as follows

$$I(V) = \frac{2e^2}{h} \sum_{n,m} \int_{\mu_R}^{\mu_L} dE [f_L(E) - f_R(E)] |t_{n,m}(E, V)|^2, \quad (1.33)$$

where  $f_L(E)$  and  $f_R(E)$  are the Fermi distributions of electrons in the left and right leads, respectively; the voltage  $V$  is equal to the difference  $\Delta\mu = \mu_L - \mu_R$  between the chemical potentials of the electrodes. The transmission amplitudes become bias-dependent, and have to be calculated in a self-consistent way [83–85]. Apparently, the applied bias  $V$  or the temperature can not be too large otherwise it would cause the interaction of electrons with ionic vibrations, leading to dephasing. If the electron-electron and electron-phonon interactions are assumed to occur in the conductor only then a Landauer-like formula can still be derived, as shown in Ref. [76]. The effect of local vibrations on the electronic transport through atomic-scaled conductors has been studied recently, based on the DFT-LDA approach combined with either the second-order perturbation theory [86] or the self-consistent Born approximation [87, 88]. In principle, inelastic processes due to the electron correlations in the conductor can also be partially included within TDDFT. There is a recent paper by Delaney and Greer [89] where the configuration interaction method was used for treating the electronic correlations in a molecular junction, but their conductance calculations rely on strong assumptions about the electronic distribution of the particle reservoirs as noted in Ref. [80]. So further developments in incorporating electron-electron and

<sup>6</sup>In a recent paper by Toher *et al.* [81] this disagreement is explained by the self-interaction errors (SIE) in the DFT-LDA approach. The SIE play a role only for weak molecule-electrode coupling and for relatively small bias. But as soon as the voltage exceeds some critical value or the coupling to electrodes is sufficiently strong then the conductance predicted in Ref. [81] for a molecular junction is again much higher than in experimental findings. Moreover, no abrupt change has been observed experimentally in the current-voltage characteristics. Note that the SIE do not play a significant role for atomic wires due to the strong wire-electrode coupling.

---

electron-phonon interactions into the transport formalism, based on the atomistic description of the conductor, are of great interest.



## Chapter 2

# Conductance calculations for quantum wires and interfaces

Landauer's formula relates the conductance of a quantum wire or interface to transmission probabilities. Total transmission probabilities are frequently calculated using Green function techniques and an expression derived by Caroli. Alternatively, partial transmission probabilities can be calculated from the scattering wave functions that are obtained by matching the wave functions in the scattering region to the Bloch modes of ideal bulk leads. An elegant technique for doing this, formulated by Ando, is here generalized to any Hamiltonian that can be represented in tight-binding form. A more compact expression for the transmission matrix elements is derived and it is shown how all the Green function results can be derived from the mode matching technique. We illustrate this for a simple model which can be studied analytically, and for an Fe|vacuum|Fe tunnel junction which we study using first-principles calculations.

### 2.1 Introduction

Since the discovery of giant magnetoresistance in metallic multilayers there has been considerable interest in studying electronic transport in layered materials [90, 91]. At the same time, experimental control of the lateral scale has enabled studies of electronic transport in quantum wires of atomic dimensions [61]. Because of the small dimensions involved, the transport properties of both of these systems should be understood on the basis of their atomic structure. This perception has generated a large effort in recent years to calculate the conductance of multilayers and quantum wires from first principles. Several different approaches have been formulated which have a common basis in the Landauer-Büttiker approach or are equivalent to it. In the linear response regime, the conductance  $\mathcal{G}$  is expressed as a quantum mechanical scattering problem [67] and can be simply related to the total transmission probability

at the Fermi energy,  $T(E_F)$ , as

$$\mathcal{G} = \frac{e^2}{h} T(E_F). \quad (2.1)$$

The multilayer or quantum wire is generally considered as a scattering region of finite size, sandwiched between two semi-infinite ballistic wires. Aiming at a materials specific description, most current approaches treat the electronic structure within the framework of density functional theory (DFT) [84, 92–100].

Frequently the conductance is calculated using a Green function expression derived by Caroli *et al.* [62, 75]. An alternative technique, suitable for Hamiltonians that can be represented in tight-binding form, has been formulated by Ando [101]. It is based upon directly matching the wave function in the scattering region to the Bloch modes of the leads. The latter technique has been applied to conductance calculations at the empirical tight-binding level [102], as well as on the first-principles DFT level [95, 103–105]. The relationship between the mode matching [101] and Green function [62, 75, 106] approaches is not immediately obvious. Indeed, it was recently stated that Ando’s approach is incomplete and does not yield the correct expression for the conductance [106].

In this Chapter we demonstrate that the two approaches are completely equivalent. In the Green function approach, a small imaginary part must be added to or subtracted from the energy in order to distinguish between the retarded and advanced forms [84, 92–94, 97–100, 106]. In mode matching, scattering wave functions are calculated that incorporate the retarded or advanced boundary conditions directly. This makes it possible to solve the scattering problem also at real, instead of complex energies. In addition to yielding the total conductance, by focussing on wave functions the contribution of each individual scattering channel can be identified. In particular, we derive a simple, compact expression for the transmission matrix elements, see Eq. (2.67).

The Chapter is organized as follows. In the next section the Hamiltonian we will use is introduced. This model allows us to study both quantum wires that are finite in the directions perpendicular to the wire, and systems that are periodic in these directions such as single interfaces, sandwiches and multilayers. We will use the single term “quantum wire” to describe both systems. In Secs. 2.3 and 2.4 the mode matching and Green function techniques are summarized. The equivalence of the transmission matrices obtained using these two techniques is demonstrated in Sec. 2.5 and the Caroli expression for the conductance is derived from the mode matching expressions. In Sec. 2.6 the two techniques are applied first to a simple analytical model [107], and then to an Fe|vacuum|Fe tunnel junction using numerical first-principles calculations. The main conclusions are summarized in Sec. 2.7.

## 2.2 Hamiltonian

We set up a tight-binding representation of the Hamiltonian. This is not a severe restriction since a first-principles DFT implementation that uses a representation on

an atomic orbital basis set has the same mathematical structure as a tight-binding model [108].<sup>1</sup> Alternatively, an implementation that uses a representation of the Hamiltonian on a grid in real space, can also be mapped onto a tight-binding model [70]. We begin by dividing the system into slices (“principal layers”) perpendicular to the wire direction [109]. The thickness of these slices is chosen such that there is only an interaction between neighboring slices. Labelling each slice with an index  $i$ , the Schrödinger equation of the quantum wire becomes

$$-\mathbf{H}_{i,i-1}\mathbf{c}_{i-1} + (E\mathbf{I} - \mathbf{H}_{i,i})\mathbf{c}_i - \mathbf{H}_{i,i+1}\mathbf{c}_{i+1} = 0, \quad (2.2)$$

for  $i = -\infty, \dots, \infty$ . Assuming that each slice contains  $N$  sites and/or orbitals,  $\mathbf{c}_i$  is a vector of dimension  $N$  containing the wave function coefficients on all sites and/or orbitals of slice  $i$ . The  $N \times N$  matrices  $\mathbf{H}_{i,i}$  and  $\mathbf{H}_{i,i\pm 1}$  consist of on-slice and hopping matrix elements of the Hamiltonian, respectively.  $\mathbf{I}$  is the  $N \times N$  identity matrix. A schematic representation of the structure of the Hamiltonian is given in Fig. 2.1.

Eq. (2.2) is valid both for quantum wires that are finite in the directions parallel to the slices, and for layered systems that are periodic in these directions. In the latter case, translations in the transverse direction can be described in terms of a Bloch wave vector in the two-dimensional Brillouin zone,  $\mathbf{k}_{\parallel}$ , which is a good quantum number and the system becomes effectively one dimensional. Explicit expressions for the Hamilton matrix elements depend upon the particular localized orbital basis or real-space grid representation used.<sup>2</sup> Since details of the tight-binding muffin tin orbital scheme used in Refs. [95, 103–105] are given in Ref. [108] and of the real-space high-order finite-difference method can be found in Ref. [70], they will not be discussed further here.

The system is divided into three parts, with  $i = -\infty, \dots, 0$  corresponding to the left lead (L),  $i = 1, \dots, S$  to the scattering region (S) and  $i = S + 1, \dots, \infty$  to the right lead (R). The leads are assumed to be ideal wires characterized by a periodic potential. It is then sufficient to identify a slice with a translational period along the wire. By construction, the Hamilton matrix is the same for each slice of the leads, i.e.  $\mathbf{H}_{i,i} \equiv \mathbf{H}_{L/R}$ ,  $\mathbf{H}_{i,i-1} \equiv \mathbf{B}_{L/R}$  and  $\mathbf{H}_{i,i+1} \equiv \mathbf{B}_{L/R}^{\dagger}$  for the left/right leads. Fig. 2.1 summarizes our model of a quantum wire.

## 2.3 Mode matching approach

Eq. (2.2) can be solved in a particularly convenient way by a technique which we call mode matching. In this, we follow Ando and generalize his approach to a slice geometry [101].

<sup>1</sup>We restrict ourselves to a representation on orthogonal basis sets, but the extension to non-orthogonal basis sets is straightforward.

<sup>2</sup>In some representations the hopping matrices can be singular. In all cases where the inverse of such a matrix would be needed, one can use the well-defined pseudo-inverse matrix instead, cf. Ref. [110]

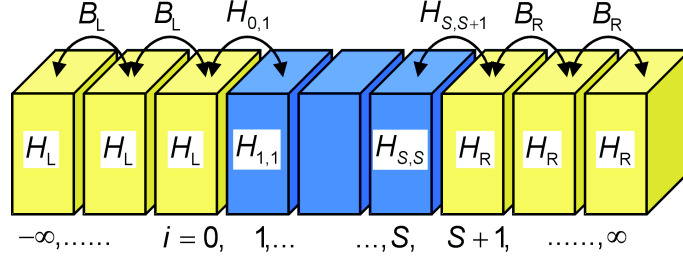


**Figure 2.1** : Hamilton matrix of a quantum wire divided into slices. The left (L) and right (R) leads are ideal periodic wires that span the cells  $i = -\infty, \dots, 0$  and  $i = S + 1, \dots, \infty$ , respectively. The scattering region spans cells  $i = 1, \dots, S$ .

### 2.3.1 Bloch matrices

The first step consists of finding solutions for the leads, for which Eq. (2.2) can be simplified to

$$-\mathbf{B}\mathbf{c}_{i-1} + (\mathbf{E}\mathbf{I} - \mathbf{H})\mathbf{c}_i - \mathbf{B}^\dagger\mathbf{c}_{i+1} = 0. \quad (2.3)$$

These equations hold for  $i = -\infty, \dots, -1$  and  $i = S + 2, \dots, \infty$ , i.e. the left and right leads. To keep the notation as simple as possible, we have omitted the subscripts L and R, see Fig. 2.1. Since the leads are periodic wires, one can make the ansatz that the solutions have Bloch symmetry, i.e.  $\mathbf{c}_i = \lambda\mathbf{c}_{i-1}$ ,  $\mathbf{c}_{i+1} = \lambda^2\mathbf{c}_{i-1}$ , where  $\lambda$  is the Bloch factor. Substituting this into Eq. (2.3) results in a quadratic eigenvalue equation of dimension  $N$ . The latter can be solved most easily by transforming it to an equivalent linear (generalized) eigenvalue problem of dimension  $2N$  and solving this by a standard algorithm [110, 111].

It can be shown that the equation generally has  $2N$  solutions, which can be divided into  $N$  right-going modes and  $N$  left-going modes [112], labelled as (+) and (-) in the following. Right-going modes are either evanescent waves that are decaying to the right, or waves of constant amplitude that are propagating to the right, whereas left-going modes are decaying or propagating to the left. We denote the eigenvalues by  $\lambda_n(\pm)$  where  $n = 1, \dots, N$ , the corresponding eigenvectors by  $\mathbf{u}_n(\pm)$  and write the eigenvalue equation as

$$-\mathbf{B}\mathbf{u}_n(\pm) + (\mathbf{E}\mathbf{I} - \mathbf{H})\lambda_n(\pm)\mathbf{u}_n(\pm) - \mathbf{B}^\dagger\lambda_n(\pm)^2\mathbf{u}_n(\pm) = 0. \quad (2.4)$$

In the following we assume that the vectors  $\mathbf{u}_n(\pm)$  are normalized; note that in general they are *not* orthogonal.

One can distinguish right- from left-going evanescent modes on the basis of their eigenvalues; right going evanescent modes have  $|\lambda(+)| < 1$  and left going evanescent modes have  $|\lambda(-)| > 1$ . Propagating modes have  $|\lambda(\pm)| = 1$ , so here one has to determine the Bloch velocity and use its sign to distinguish right from left propagation. The Bloch velocities are given by the expression

$$v_n(\pm) = -\frac{2a}{\hbar} \text{Im} [\lambda_n(\pm)\mathbf{u}_n(\pm)^\dagger \mathbf{B}^\dagger \mathbf{u}_n(\pm)], \quad (2.5)$$



where  $a$  is the slice thickness. A derivation of this equation is given in Appendix A.1.

Since the eigenvectors are non-orthogonal, it is convenient to define dual vectors  $\tilde{\mathbf{u}}_n(\pm)$

$$\tilde{\mathbf{u}}_n^\dagger(\pm)\mathbf{u}_m(\pm) = \delta_{n,m}; \quad \mathbf{u}_n^\dagger(\pm)\tilde{\mathbf{u}}_m(\pm) = \delta_{n,m}. \quad (2.6)$$

Any wave function in the leads can be expressed as a linear combination of the lead modes. This can be done in a compact form using the two  $N \times N$  Bloch matrices for right- and left-going solutions

$$\mathbf{F}(\pm) = \sum_{n=1}^N \lambda_n(\pm)\mathbf{u}_n(\pm)\tilde{\mathbf{u}}_n^\dagger(\pm). \quad (2.7)$$

For any integer  $i$ ,  $\mathbf{F}^i$  is given by a similar expression but with  $\lambda_n$  replaced by  $\lambda_n^i$ . From the foregoing it is easy to show that the Bloch matrices obey the equation

$$-\mathbf{B}\mathbf{F}^{-1}(\pm) + (E\mathbf{I} - \mathbf{H}) - \mathbf{B}^\dagger\mathbf{F}(\pm) = 0. \quad (2.8)$$

A general solution in the leads can be expressed in terms of a recursion relation

$$\begin{aligned} \mathbf{c}_i &= \mathbf{c}_i(+)+\mathbf{c}_i(-) \\ &= \mathbf{F}^{i-j}(+)\mathbf{c}_j(+)+\mathbf{F}^{i-j}(-)\mathbf{c}_j(-). \end{aligned} \quad (2.9)$$

Fixing the coefficients in one slice then sets the boundary conditions and determines the solution for the whole lead.

### 2.3.2 Transmission matrix

The scattering region is defined by  $i = 1, \dots, S$ , see Fig. 2.1. Right and left of the scattering regions one has the recursion relations for the states in the leads from Eq. (2.9)

$$\begin{aligned} \mathbf{c}_{-1} &= \mathbf{F}_L^{-1}(+)\mathbf{c}_0(+) + \mathbf{F}_L^{-1}(-)\mathbf{c}_0(-) \\ &= [\mathbf{F}_L^{-1}(+) - \mathbf{F}_L^{-1}(-)]\mathbf{c}_0(+) + \mathbf{F}_L^{-1}(-)\mathbf{c}_0, \end{aligned} \quad (2.10)$$

with  $\mathbf{c}_0 = \mathbf{c}_0(+) + \mathbf{c}_0(-)$  and

$$\mathbf{c}_{S+2} = \mathbf{F}_R(+)\mathbf{c}_{S+1}(+) + \mathbf{F}_R(-)\mathbf{c}_{S+1}(-), \quad (2.11)$$

where the subscripts L and R distinguish between the Bloch matrices of the left and right leads.

The boundary conditions for the scattering problem are set up in the usual way. The vector  $\mathbf{c}_0(+)$  is treated as the source, i.e. as a fixed incoming wave from the left lead. There is no incoming wave from the right lead, so we set  $\mathbf{c}_{S+1}(-) = 0$ .

Having set the boundary conditions, Eqs. (2.10) and (2.11) can be used to rewrite Eq. (2.2) in the region not covered by Eq. (2.3), i.e. for  $i = 0, \dots, S+1$ . This describes

the wave function in the scattering region and the matching to the solutions in the leads. Eq. (2.2) in this region is rewritten as

$$-\mathbf{H}'_{i,i-1}\mathbf{c}_{i-1} + (E\mathbf{I} - \mathbf{H}'_{i,i})\mathbf{c}_i - \mathbf{H}'_{i,i+1}\mathbf{c}_{i+1} = \mathbf{Q}_i\mathbf{c}_0(+), \quad (2.12)$$

with a modified Hamilton matrix defined so  $\mathbf{H}'_{i,j} = \mathbf{H}_{i,j}$  for the elements  $\{i, j = 0, 1\}$ ,  $\{i = 1, \dots, S; j = i, i \pm 1\}$  and  $\{i, j = S + 1, S\}$ , but with

$$\begin{aligned} \mathbf{H}'_{0,0} &= \mathbf{H}_L + \mathbf{B}_L\mathbf{F}_L^{-1}(-), \\ \mathbf{H}'_{S+1,S+1} &= \mathbf{H}_R + \mathbf{B}_R^\dagger\mathbf{F}_R(+). \end{aligned} \quad (2.13)$$

$\mathbf{H}'_{0,-1} = 0$  and  $\mathbf{H}'_{S+1,S+2} = 0$ , so the modified scattering region is decoupled from the leads. On the left-hand side of Eq. (2.12), we have a source term with

$$\mathbf{Q}_0 = \mathbf{B}_L [\mathbf{F}_L^{-1}(+) - \mathbf{F}_L^{-1}(-)], \quad (2.14)$$

and  $\mathbf{Q}_i = 0$  for  $i = 1, \dots, S + 1$ . Eq. (2.12) defines a set of  $(S + 2) \times N$  linear equations. Because the Hamilton matrix is block tridiagonal, each block being of dimension  $N$ , this set of equations can be solved efficiently using a block Gaussian elimination scheme [110]. The total wave function  $\mathbf{c}_i$  can then be obtained by back substitution.

The transmission is obtained from the wave function in the right lead  $\mathbf{c}_{S+1}(+)$ . In particular, choosing the incoming wave as one of the modes of the left lead, i.e.  $\mathbf{c}_0(+) = \mathbf{u}_{L,m}(+)$ , generalized transmission matrix elements  $\tau_{n,m}$  are defined by expanding  $\mathbf{c}_{S+1}(+)$  in modes of the right lead

$$\mathbf{c}_{S+1}(+) = \sum_{n=1}^N \mathbf{u}_{R,n}(+)\tau_{n,m}. \quad (2.15)$$

By letting  $\mathbf{c}_0(+) run over all possible incoming modes of the left lead  $\mathbf{u}_{L,m}(+)$ ;  $m = 1, \dots, N$ , a full transmission matrix is obtained.$

Matrix elements can be defined for all modes, propagating and evanescent, but of course only matrix elements where  $n, m$  denote propagating modes contribute to the real physical transmission. These modes can be selected by making use of their eigenvalues; see the discussion following Eq. (2.4). The physical transmission matrix elements are then found by normalizing with respect to the current [62]

$$t_{n,m} = \sqrt{\frac{v_{R,n}(+)a_L}{v_{L,m}(+)a_R}} \tau_{n,m}, \quad (2.16)$$

where  $v_{L,m}(+)$  and  $v_{R,n}(+)$  are the Bloch velocities in the direction of the wire for the right-propagating modes  $m$  and  $n$  in the left and right leads, respectively, see Eq. (2.5);  $a_L$  and  $a_R$  are the slice thicknesses of left and right leads.<sup>3</sup> The total

<sup>3</sup>The current per mode is given by velocity  $\times$  density. Since we normalize a mode in a slice, its density is given by 1/thickness of the slice.

transmission probability is given by

$$T(E) = \sum_{n,m}^{(+)} |t_{n,m}|^2, \quad (2.17)$$

and the conductance is given by Eq. (2.1) evaluated at  $E = E_F$ .

### 2.3.3 Green function matrix

Solving the set of linear equations Eq. (2.12) directly leads to the conductance. However, to facilitate a connection to the Green function approach discussed in the next section, we can formulate the solution in a slightly different way. A finite Green function matrix  $\mathbf{G}'_{i,j}(z)$ ,  $i, j = 0, \dots, S+1$  can be defined by

$$-\mathbf{H}'_{i,i-1} \mathbf{G}'_{i-1,j} + (z\mathbf{I} - \mathbf{H}'_{i,i}) \mathbf{G}'_{i,j} - \mathbf{H}'_{i,i+1} \mathbf{G}'_{i+1,j} = \mathbf{I}\delta_{i,j}, \quad (2.18)$$

with  $z$  complex. Note, however, that the matrices  $\mathbf{H}'_{0,0}$  and  $\mathbf{H}'_{S+1,S+1}$  are non-Hermitian and  $\mathbf{G}'_{i,j}(E)$  is also uniquely defined for real energies. The Green function matrix allows the solution of Eq. (2.12) to be written as

$$\mathbf{c}_i = \mathbf{G}'_{i,0}(E) \mathbf{Q}_0 \mathbf{c}_0(+). \quad (2.19)$$

As before, the transmission can be extracted at  $i = S+1$  and comparison with Eq. (2.15) gives

$$\tau_{n,m} = \tilde{\mathbf{u}}_{R,n}^\dagger(+)\mathbf{G}'_{S+1,0}(E) \mathbf{Q}_0 \mathbf{u}_{L,m}(+). \quad (2.20)$$

which can be used in Eq. (2.16). The Green function matrix block  $\mathbf{G}'_{S+1,0}(E)$  can be found by solving Eq. (2.18) using a recursive algorithm that resembles a Gaussian elimination scheme [108, 113].

## 2.4 Green function approach

An apparently quite different route to the transmission matrix starts by defining an infinite Green function matrix  $\mathbf{G}_{i,j}(z)$  for  $i, j = -\infty, \dots, \infty$  with respect to the original Hamiltonian of Eq. (2.2).

$$-\mathbf{H}_{i,i-1} \mathbf{G}_{i-1,j} + (z\mathbf{I} - \mathbf{H}_{i,i}) \mathbf{G}_{i,j} - \mathbf{H}_{i,i+1} \mathbf{G}_{i+1,j} = \mathbf{I}\delta_{i,j}. \quad (2.21)$$

Choosing  $z = \lim_{\eta \rightarrow 0} (E \pm i\eta)$  defines as usual the retarded/advanced Green function matrix. We shall use  $\mathbf{G}_{i,j}(E)$  to denote the *retarded* Green function matrix and  $\mathbf{G}_{i,j}^a(E)$  to denote the *advanced* Green function matrix.

### 2.4.1 Partitioning

Eq. (2.21) is most conveniently solved by applying a partitioning technique [62, 114]. It is straightforward to show that the finite part  $\mathbf{G}_{i,j}(z)$  defined for  $i, j = 0, \dots, S+1$

can be derived from a closed set of equations, similar to Eq. (2.21), but with  $\mathbf{H}_{i,j}$  replaced by  $\mathbf{H}_{i,j}''$  where  $\mathbf{H}_{i,j}'' = \mathbf{H}_{i,j}$  for the elements  $\{i, j = 0, 1\}$ ,  $\{i = 1, \dots, S; j = i, i \pm 1\}$  and  $\{i, j = S + 1, S\}$ , but with

$$\begin{aligned}\mathbf{H}_{0,0}''(z) &= \mathbf{H}_L + \mathbf{B}_L \mathbf{g}_L(z) \mathbf{B}_L^\dagger, \\ \mathbf{H}_{S+1,S+1}''(z) &= \mathbf{H}_R + \mathbf{B}_R^\dagger \mathbf{g}_R(z) \mathbf{B}_R.\end{aligned}\quad (2.22)$$

Here  $\mathbf{g}_L(z)$  and  $\mathbf{g}_R(z)$  are the surface Green functions of the semi-infinite left and right leads, respectively, which can be calculated using an iterative technique: denoting  $\mathbf{G}_{i,j}^{[n]}(z)$  as the solution of an equation similar to Eq. (2.21), but with  $\mathbf{H}_{i,j} = 0$  for  $\{i > n \vee j > n\}$ , one can easily derive the right-going recursion relation

$$\left[ z\mathbf{I} - \mathbf{H}_{n+1,n+1} - \mathbf{H}_{n+1,n} \mathbf{G}_{n,n}^{[n]}(z) \mathbf{H}_{n,n+1} \right] \mathbf{G}_{n+1,n+1}^{[n+1]}(z) = \mathbf{I}. \quad (2.23)$$

For an ideal wire with  $i, j = -\infty, \dots, n$ ,  $\mathbf{G}_{n,n}^{[n]}(z) = \mathbf{g}_L(z)$  should be independent of  $n$  resulting in the following equation for the surface Green function,

$$\left[ z\mathbf{I} - \mathbf{H}_L - \mathbf{B}_L \mathbf{g}_L(z) \mathbf{B}_L^\dagger \right] \mathbf{g}_L(z) = \mathbf{I}. \quad (2.24)$$

Several iterative algorithms have been formulated for solving this non-linear matrix equation [109, 115, 116]. A similar reasoning based upon a left-going recursion for the right lead results in an equation for the surface Green function  $\mathbf{g}_R(z)$  of the right lead

$$\left[ z\mathbf{I} - \mathbf{H}_R - \mathbf{B}_R^\dagger \mathbf{g}_R(z) \mathbf{B}_R \right] \mathbf{g}_R(z) = \mathbf{I}. \quad (2.25)$$

Again, setting  $z = E + i\eta$  in Eqs. (2.24) and (2.25) defines the usual retarded surface Green functions  $\mathbf{g}_{L/R}(E)$ . Although we are mainly interested in the physical limit  $\lim_{\eta \rightarrow 0}$ , in practice a finite value of  $\eta$  is often used in order to make the iterative algorithms stable.

The quantities

$$\Sigma_L(E) = \mathbf{B}_L \mathbf{g}_L(E) \mathbf{B}_L^\dagger; \quad \Sigma_R(E) = \mathbf{B}_R^\dagger \mathbf{g}_R(E) \mathbf{B}_R, \quad (2.26)$$

which appear in Eqs. (2.22)-(2.25), are called the self-energies of the left and right leads, respectively [62]. Once these are obtained, the finite Hamilton matrix of Eq. (2.22) is constructed and the retarded Green function matrix  $\mathbf{G}_{i,j}(E)$  can be found using a recursive algorithm [113]. Using the lead modes the transmission matrix elements can then be calculated, as will be shown in the next section, Sec. 2.4.2. Alternatively, the total transmission probability can be expressed in a form that does not require the lead modes explicitly, which is discussed in Sec. 2.5.

## 2.4.2 Transmission matrix

The transmission matrix can be obtained from the Green function matrix of Eq. (2.21). To do this, we adapt a Fisher-Lee type of approach to our tight-binding formulation [65]. Assuming that the unperturbed reference wave function is the Bloch mode

$\mathbf{u}_{L,m}(+)$  that comes in from the left lead, the Lippmann-Schwinger equation [117] in tight-binding form is

$$\begin{aligned} \mathbf{c}_i &= \mathbf{u}_{L,m,i}(+) + \sum_{j,k} \mathbf{G}_{i,j} \mathbf{V}_{j,k} \mathbf{u}_{L,m,k}(+) \\ &= \left[ \mathbf{F}_L^i(+) + \sum_{j,k} \mathbf{G}_{i,j} \mathbf{V}_{j,k} \mathbf{F}_L^k(+) \right] \mathbf{u}_{L,m}(+). \end{aligned} \quad (2.27)$$

Here  $\mathbf{u}_{L,m,i}(+)$  is the reference wave function in slice  $i$ . It obeys Bloch symmetry and  $\mathbf{u}_{L,m}(+) \equiv \mathbf{u}_{L,m,0}(+)$  is the Bloch mode at the origin, see Sec. 2.3.1. The matrix  $\mathbf{V}_{j,k}$  represents the perturbation with respect to the ideal left lead.

Eq. (2.27) can be simplified using the Dyson equation, which in tight-binding form reads

$$\begin{aligned} \mathbf{G}_{i,0} &= \mathbf{G}_{i,0}^{(0)} + \sum_{j,k} \mathbf{G}_{i,j} \mathbf{V}_{j,k} \mathbf{G}_{k,0}^{(0)} \\ &= \left[ \mathbf{F}_L^i(+) + \sum_{j,k} \mathbf{G}_{i,j} \mathbf{V}_{j,k} \mathbf{F}_L^k(+) \right] \mathbf{G}_{0,0}^{(0)}, \end{aligned} \quad (2.28)$$

using Eq. (2.32). Comparing Eqs. (2.27) and (2.28) one finds the simple expression

$$\mathbf{c}_i = \mathbf{G}_{i,0}(E) \left[ \mathbf{G}_{0,0}^{(0)}(E) \right]^{-1} \mathbf{u}_{L,m}(+). \quad (2.29)$$

From the definition of the generalized transmission matrix elements, cf. Eq. (2.15), one then obtains the expression

$$\tau_{n,m} = \tilde{\mathbf{u}}_{R,n}^\dagger(+) \mathbf{G}_{S+1,0}(E) \left[ \mathbf{G}_{0,0}^{(0)}(E) \right]^{-1} \mathbf{u}_{L,m}(+). \quad (2.30)$$

To find  $\tau_{n,m}$  one needs to calculate only the Green function matrix blocks  $\mathbf{G}_{S+1,0}(E)$  of the full system and  $\mathbf{G}_{0,0}^{(0)}(E)$  of the ideal left lead. The physical transmission matrix elements and the total transmission probability can then be obtained from Eqs. (2.16) and (2.17).

## 2.5 Mode matching versus Green functions

The two seemingly different formalisms introduced in Secs. 2.3 and 2.4 are in fact closely related. In this section we will show how all Green function results can be obtained from the mode matching approach. We begin by expressing the Green function matrices of ideal wires in terms of the Bloch matrices,  $\mathbf{F}(\pm)$ . These expressions are then used to prove that the transmission matrix elements obtained from the mode matching and Green function approaches, cf. Eqs. (2.20) and (2.30), are

in fact identical. After that, we show that the transmission matrix elements are independent of the exact positions within the leads that are used to match the leads to the scattering region, apart from a trivial phase factor. Then we derive from the mode matching expression for the total transmission probability the Green function expression known as the Caroli expression [75]. Finally, a more compact expression for the transmission matrix elements is derived.

### 2.5.1 Green functions of ideal wires in terms of Bloch matrices

We begin by deriving an expression for the retarded Green function matrix  $\mathbf{G}_{i,j}^{(0)}$  of an *ideal infinite wire* in terms of its eigenmodes [118]. The columns of such a Green function obey the equation

$$-\mathbf{B}\mathbf{G}_{i-1,j}^{(0)} + (E^+\mathbf{I} - \mathbf{H})\mathbf{G}_{i,j}^{(0)} - \mathbf{B}^\dagger\mathbf{G}_{i+1,j}^{(0)} = \mathbf{I}\delta_{i,j}, \quad (2.31)$$

where  $E^+ = E + i\eta$ . For  $i \neq j$  the solution is similar to that of the wave functions, see Eq. (2.3). In addition, the retarded Green function should consist only of propagating waves that move outwards from the  $\delta$ -source and/or evanescent states that decay away from the source [117]. From Eq. (2.9), we have the *column* recursion relations

$$\begin{aligned} \mathbf{G}_{i,j}^{(0)}(E) &= \mathbf{F}^{i-j}(-)\mathbf{G}_{j,j}^{(0)}(E), \quad i < j, \\ \mathbf{G}_{i,j}^{(0)}(E) &= \mathbf{F}^{i-j}(+)\mathbf{G}_{j,j}^{(0)}(E), \quad i > j. \end{aligned} \quad (2.32)$$

The diagonal block  $\mathbf{G}_{j,j}^{(0)}(E)$  can now be obtained by combining Eqs. (2.31) and (2.32), which gives for  $i = j$

$$[-\mathbf{B}\mathbf{F}^{-1}(-) + E^+\mathbf{I} - \mathbf{H} - \mathbf{B}^\dagger\mathbf{F}(+)]\mathbf{G}_{j,j}^{(0)} = \mathbf{I}. \quad (2.33)$$

Eliminating  $E^+\mathbf{I} - \mathbf{H}$  using Eq. (2.8) then yields

$$\left[\mathbf{G}_{j,j}^{(0)}(E)\right]^{-1} = \mathbf{B}\left[\mathbf{F}^{-1}(+) - \mathbf{F}^{-1}(-)\right], \quad (2.34)$$

or the equivalent

$$\left[\mathbf{G}_{j,j}^{(0)}(E)\right]^{-1} = \mathbf{B}^\dagger[\mathbf{F}(-) - \mathbf{F}(+)], \quad (2.35)$$

Eqs. (2.32) and (2.34) represent the full expression for the Green function  $\mathbf{G}_{i,j}^{(0)}$  of an infinite ideal wire in terms of the Bloch matrices  $\mathbf{F}(\pm)$  and thus in terms of the eigenmodes. Note that we can set  $E^+ = E$  since, in terms of the modes, the retarded Green function matrix is uniquely defined for real energies.

The *advanced* Green function matrix  $\mathbf{G}_{i,0}^{(0)a}(E)$  can be found from a similar procedure. It should consist of propagating waves that move towards the source and/or evanescent states that grow towards the source. One can construct two new Bloch matrices  $\mathbf{F}^a(\pm)$ , which are similar to those defined in Eq. (2.7). In  $\mathbf{F}^a(+)$  one collects the modes that are decaying to the right (growing to the left) and modes that are

propagating to the left.  $\mathbf{F}^a(-)$  then contains modes that grow or propagate to the right.

$$\begin{aligned}\mathbf{F}^a(\pm) &= \sum_{n=1}^N \lambda_n^a(\pm) \mathbf{u}_n^a(\pm) \tilde{\mathbf{u}}_n^{a\dagger}(\pm), \text{ with} & (2.36) \\ \lambda_n^a(\pm) &= \lambda_n(\mp), \mathbf{u}_n^a(\pm) = \mathbf{u}_n(\mp) \text{ propagating} \\ \lambda_n^a(\pm) &= \lambda_n(\pm), \mathbf{u}_n^a(\pm) = \mathbf{u}_n(\pm) \text{ evanescent.}\end{aligned}$$

Using these definitions, expressions for the advanced Green function matrix are obtained from Eqs. (2.32) and (2.34) by replacing  $\mathbf{F}(\pm)$  with  $\mathbf{F}^a(\pm)$ .

From the general relation between retarded and advanced Green functions,  $\mathbf{G}_{i,j} = (\mathbf{G}_{j,i}^a)^\dagger$ , the following *row* recursion relations can be deduced for the retarded Green function

$$\begin{aligned}\mathbf{G}_{i,j}^{(0)}(E) &= \mathbf{G}_{i,i}^{(0)}(E) [\mathbf{F}^{a\dagger}(+)]^{j-i}, \quad i < j, \\ \mathbf{G}_{i,j}^{(0)}(E) &= \mathbf{G}_{i,i}^{(0)}(E) [\mathbf{F}^{a\dagger}(-)]^{j-i}, \quad i > j.\end{aligned} \quad (2.37)$$

The retarded Green function  $\mathbf{G}_{i,0}^{(s)}(E)$  of a *semi-infinite wire* extending from  $i = -\infty, \dots, 0$  can be obtained using a similar technique. Instead of Eq. (2.32), we get

$$\mathbf{G}_{i,0}^{(s)}(E) = \mathbf{F}^i(-) \mathbf{g}(E), \quad i < 0. \quad (2.38)$$

where  $\mathbf{g}(E) = \mathbf{G}_{0,0}^{(s)}(E)$  is the surface Green function. Using this in Eq. (2.31) gives for  $i = 0$  and  $j = 0$  and for  $i = -1$  and  $j = 0$ , respectively,

$$\begin{aligned}[-\mathbf{B}\mathbf{F}^{-1}(-) + E^+\mathbf{I} - \mathbf{H}] \mathbf{g} &= \mathbf{I}, \\ [-\mathbf{B}\mathbf{F}^{-1}(-) + E^+\mathbf{I} - \mathbf{H}] \mathbf{F}^{-1}(-) \mathbf{g} &= \mathbf{B}^\dagger \mathbf{g}.\end{aligned} \quad (2.39)$$

Note that the  $\mathbf{B}^\dagger$  term is absent in the first equation since we are dealing with a semi-infinite wire. These two equations can be easily solved to find an expression for the surface Green function [109, 118, 119]

$$\mathbf{g}(E) = \mathbf{F}^{-1}(-) (\mathbf{B}^\dagger)^{-1}. \quad (2.40)$$

Eqs. (2.38) and (2.40) represent the Green function of a semi-infinite ideal wire extending from  $i = -\infty, \dots, 0$ . In a similar fashion, one gets for the Green function of a semi-infinite ideal wire extending from  $i = 0, \dots, \infty$

$$\mathbf{G}_{i,0}^{(s)}(E) = \mathbf{F}^{i+1}(+) \mathbf{B}^{-1}, \quad i \geq 0. \quad (2.41)$$

Analogously to Eqs. (2.38)-(2.41), one can define the advanced Green function matrix  $\mathbf{G}_{i,0}^{(s)a}(E)$  in terms of the Bloch matrices  $\mathbf{F}^a(\pm)$ . Moreover, since  $[\mathbf{g}^a]^\dagger = \mathbf{g}$ , we have the following relation between the Bloch matrices

$$\mathbf{B}^\dagger \mathbf{F}(\pm) = \mathbf{F}^{a\dagger}(\pm) \mathbf{B}. \quad (2.42)$$

### 2.5.2 Equivalence of mode matching and Green function approaches

The retarded surface Green functions of the left and right leads can be derived from Eqs. (2.40) and (2.41)

$$\mathbf{g}_L(E) = \mathbf{F}_L^{-1}(-) \left[ \mathbf{B}_L^\dagger \right]^{-1}; \quad \mathbf{g}_R(E) = \mathbf{F}_R(+)\mathbf{B}_R^{-1}. \quad (2.43)$$

The retarded self-energies of Eq. (2.26) are then given by

$$\Sigma_L(E) = \mathbf{B}_L \mathbf{F}_L^{-1}(-); \quad \Sigma_R(E) = \mathbf{B}_R^\dagger \mathbf{F}_R(+). \quad (2.44)$$

Comparing Eqs. (2.13) and (2.22) then establishes

$$\mathbf{G}'_{i,j}(E) = \mathbf{G}_{i,j}(E). \quad (2.45)$$

In other words, the two Green functions discussed in Secs. 2.3 and 2.4 are identical. By comparing Eqs. (2.14) and (2.34) one has

$$\mathbf{Q}_0 = \left[ \mathbf{G}_{0,0}^{(0)}(E) \right]^{-1}. \quad (2.46)$$

In conclusion, the two expressions for the generalized transmission matrix elements, Eqs. (2.20) and (2.30), are identical.

### 2.5.3 Invariance of transmission probability

Apart from trivial phase factors, the transmission matrix elements should not depend on where in the ideal lead the wave function matching is carried out. In a recent paper it was stated that Ando's expression for  $t_{n,m}$ , Eqs. (2.20) and (2.16), lacks this invariance property and is therefore incomplete [106]. One can however prove directly from Eq. (2.20) that the transmission matrix elements do have the required invariance property [120]. The proof becomes easier if the equivalence of Eqs. (2.20) and (2.30), established above, is used.

The scattering region runs from slices 0 to  $S+1$  if we include the boundaries with the left and right leads. This means that the Green function matrix  $\mathbf{G}_{i,j}$  with indices  $i, j$  outside this region obeys the equations for the ideal leads. From the column and row recursion relations, Eqs. (2.32) and (2.37), one derives

$$\mathbf{G}_{S+1+i,j}(E) = \mathbf{F}_R^i(+)\mathbf{G}_{S+1,0}(E) \left[ \mathbf{F}_L^{a\dagger}(-) \right]^j, \quad (2.47)$$

for  $j < 0, i > 0$ . In a similar way, one derives for the Green function matrix of the left lead

$$\mathbf{G}_{j,j}^{(0)}(E) = \mathbf{F}_L^j(+)\mathbf{G}_{0,0}^{(0)}(E) \left[ \mathbf{F}_L^{a\dagger}(-) \right]^j, \quad (2.48)$$

for  $j < 0$ .



We now artificially extend the scattering region by including slices from the left and right leads and let it run from  $j < 0$  to  $S + 1 + i$  with  $i > 0$ . Eq. (2.30) gives for the transmission matrix element

$$\tau'_{n,m} = \tilde{\mathbf{u}}_{\mathbf{R},n}^\dagger(+)\mathbf{G}_{S+1+i,j}(E) \left[ \mathbf{G}_{j,j}^{(0)}(E) \right]^{-1} \mathbf{u}_{\mathbf{L},m}(+) \quad (2.49)$$

Using (2.47) and (2.48) then gives

$$\begin{aligned} \tau'_{n,m} &= \tilde{\mathbf{u}}_{\mathbf{R},n}^\dagger(+)\mathbf{F}_{\mathbf{R}}^i(+)\mathbf{G}_{S+1,0}(E) \left[ \mathbf{G}_{0,0}^{(0)}(E) \right]^{-1} \mathbf{F}_{\mathbf{L}}^{-j}(+)\mathbf{u}_{\mathbf{L},m}(+) \\ &= \lambda_{\mathbf{R},n}^i(+)\lambda_{\mathbf{L},m}^{-j}(+)\tau_{n,m} \\ &= e^{i\alpha}\tau_{n,m}, \end{aligned} \quad (2.50)$$

with  $\alpha$  real. The third line follows from applying Eq. (2.7). The last line follows from the fact that we are only interested in propagating states and for propagating states  $|\lambda| = 1$ . Using this result in (2.16) and (2.17) proves the invariance of the total transmission probability with respect to moving the boundaries between leads and scattering region into the leads.

#### 2.5.4 The Caroli expression

The total transmission probability is given by Eq. (2.17), where the sum has to be over propagating states only. We can extend the summation to include all  $N$  states (propagating and evanescent) by defining an  $N \times N$  transmission matrix

$$\mathbf{t} = \mathbf{V}_{\mathbf{R}}^{\frac{1}{2}}(+) \tau \tilde{\mathbf{V}}_{\mathbf{L}}^{\frac{1}{2}}(+), \quad (2.51)$$

where  $\tau$  is the matrix whose elements are given by Eq. (2.20).  $\mathbf{V}_{\mathbf{R}}(+)$  is defined as the singular, diagonal matrix that has the velocities  $v_{\mathbf{R},n}$  times the constant  $\hbar/a_{\mathbf{R}}$  on the diagonal for the right-propagating states and zeros for evanescent states. We call it the velocity matrix. Likewise a pseudo-inverse velocity matrix  $\tilde{\mathbf{V}}_{\mathbf{L}}(+)$  can be defined, which has  $1/v_{\mathbf{L},n} \times a_{\mathbf{L}}/\hbar$  on the diagonal for left-propagating states and all other matrix elements are zero. These velocity matrices project onto the space of the propagating states so that the transmission matrix has only non-zero values between propagating states. (2.17) can then be expressed in the familiar form

$$\begin{aligned} T &= \text{Tr} [\mathbf{t}^\dagger \mathbf{t}] \\ &= \text{Tr} \left[ \tau^\dagger \mathbf{V}_{\mathbf{R}}(+)\tau \tilde{\mathbf{V}}_{\mathbf{L}}(+)\right]. \end{aligned} \quad (2.52)$$

Using the above definition of the velocity matrix and Ando's expressions for the transmission matrix elements, we will show how (2.52) can be rewritten as

$$T = \text{Tr} [\mathbf{\Gamma}_{\mathbf{R}} \mathbf{G}^r \mathbf{\Gamma}_{\mathbf{L}} \mathbf{G}^a], \quad (2.53)$$

where  $\mathbf{G}^r, \mathbf{G}^a$  are short-hand notations for  $\mathbf{G}_{S+1,0}(E)$  and  $\mathbf{G}_{0,S+1}^a(E)$ , respectively. The matrices  $\mathbf{\Gamma}_{\mathbf{L}/\mathbf{R}}$  are defined as

$$\mathbf{\Gamma}_{\mathbf{L}/\mathbf{R}} = i \left[ \mathbf{\Sigma}_{\mathbf{L}/\mathbf{R}} - \mathbf{\Sigma}_{\mathbf{L}/\mathbf{R}}^\dagger \right]. \quad (2.54)$$

Eq. (2.53) is known as the Caroli expression [75], and it is often used to calculate transmission probabilities [62, 106]. It is equivalent to the Kubo-Greenwood expression for the linear response regime [100, 121]. The latter expression is also equivalent to Landauer's formula [122].

The first step is to construct  $N \times N$  matrices  $\mathbf{U}(\pm)$ , the columns of which are the eigenmodes  $\mathbf{u}_n(\pm)$ , and diagonal matrices  $\mathbf{\Lambda}(\pm)$ , the elements of which are the eigenvalues  $\lambda_n(\pm)$

$$\mathbf{U}(\pm) = \begin{pmatrix} \mathbf{u}_1(\pm) & \mathbf{u}_2(\pm) & \dots & \mathbf{u}_N(\pm) \end{pmatrix}, \quad (2.55)$$

$$\mathbf{\Lambda}(\pm)_{m,n} = \lambda_n(\pm) \delta_{m,n}. \quad (2.56)$$

From Eqs. (2.6) and (2.9) it is then easy to show that the dual vectors  $\tilde{\mathbf{u}}_n(\pm)$  form the columns of the matrix  $[\mathbf{U}(\pm)^{-1}]^\dagger$  and that the  $\mathbf{F}(\pm)$  matrices obey the equation

$$\mathbf{F}(\pm)\mathbf{U}(\pm) = \mathbf{U}(\pm)\mathbf{\Lambda}(\pm). \quad (2.57)$$

In a similar way matrices  $\mathbf{U}^a(\pm)$  and  $\mathbf{\Lambda}^a(\pm)$  can be constructed, see Eq. (2.36).

Using these definitions, one can generalize the  $\tau$ -matrix of Eq. (2.20) to

$$\tau = \mathbf{U}_R^{-1}(+) \mathbf{G}^r \mathbf{Q}_0 \mathbf{U}_L(+). \quad (2.58)$$

Note that  $\tau$ -matrix elements are defined not only between propagating states, but also between evanescent states. However, as we remarked above already, only propagating states contribute to the physical transmission.

The second step is to express the velocity matrices in terms of the  $\mathbf{\Gamma}$ -matrices. To do this we use an expression for the velocity matrix,

$$\mathbf{V}(\pm) = i [\mathbf{U}^\dagger(\pm) \mathbf{B}^\dagger \mathbf{U}(\pm) \mathbf{\Lambda}(\pm) - \mathbf{\Lambda}^\dagger(\pm) \mathbf{U}^\dagger(\pm) \mathbf{B} \mathbf{U}(\pm)], \quad (2.59)$$

which can be shown (see Appendix A.1 for a proof) to be equivalent to the definition introduced in the first paragraph of this section. Using (2.57), this can be rewritten for the right lead as

$$\begin{aligned} \mathbf{V}_R(+) &= i \mathbf{U}_R^\dagger(+) \left[ \mathbf{B}_R^\dagger \mathbf{F}_R(+) - \mathbf{F}_R^\dagger(+) \mathbf{B}_R \right] \mathbf{U}_R(+) \\ &= i \mathbf{U}_R^\dagger(+) \left[ \mathbf{\Sigma}_R - \mathbf{\Sigma}_R^\dagger \right] \mathbf{U}_R(+) \\ &= \mathbf{U}_R^\dagger(+) \mathbf{\Gamma}_R \mathbf{U}_R(+). \end{aligned} \quad (2.60)$$

The second line follows from (2.44). A similar relation between the  $\mathbf{\Gamma}$ -matrix and the velocity matrix for the left lead can be shown to exist,

$$\mathbf{V}_L(+) = \mathbf{U}_L^{a\dagger}(-) \mathbf{\Gamma}_L \mathbf{U}_L^a(-), \quad (2.61)$$

by using (2.42) and an equivalent expression for the velocity matrix, Eq. (A.7). Eqs. (2.60) and (2.61) imply that the  $\mathbf{\Gamma}$ -matrices project onto the space spanned by the propagating states.

The third step is to introduce a matrix  $\mathbf{P}$  that explicitly projects onto the propagating states of the left lead

$$\begin{aligned}\mathbf{P} &= \mathbf{U}_L(+)\mathbf{I}_p[\mathbf{U}_L^a(-)]^{-1} \\ &= \sum_{n=1}^{N_p} \mathbf{u}_{L,n}(+)\tilde{\mathbf{u}}_{L,n}^{a\dagger}(-),\end{aligned}\quad (2.62)$$

where the  $\mathbf{I}_p$ -matrix contains 1 on the  $N_p$  diagonal elements that correspond to propagating states, and 0 at all other positions. Given this projector matrix, it is possible to prove that

$$\mathbf{Q}_0\mathbf{P} = i\mathbf{\Gamma}_L. \quad (2.63)$$

The proof is given in Appendix A.2. Using this property one has

$$\begin{aligned}\mathbf{Q}_0\mathbf{U}_L(+)\tilde{\mathbf{V}}_L(+) &= \mathbf{Q}_0\mathbf{P}\mathbf{U}_L^a(-)\tilde{\mathbf{V}}_L(+) \\ &= i\mathbf{\Gamma}_L\mathbf{U}_L^a(-)\tilde{\mathbf{V}}_L(+) = i\left[\mathbf{U}_L^a(-)\right]^{-1}\mathbf{V}_L(+)\tilde{\mathbf{V}}_L(+) \\ &= i\left[\mathbf{U}_L^a(-)\right]^{-1}\mathbf{I}_p.\end{aligned}\quad (2.64)$$

Substituting (2.58), (2.60) and (2.64) into (2.52) leads directly to the Caroli expression, Eq. (2.53).

### 2.5.5 Transmission matrix: a compact expression

Using the results of the previous section it is possible to derive a more compact expression for the transmission matrix. Combining (2.51), (2.58) and (2.62) one has

$$\mathbf{t} = \mathbf{V}_R^{\frac{1}{2}}(+)\mathbf{U}_R^{-1}(+)\mathbf{G}^r\mathbf{Q}_0\mathbf{P}\mathbf{U}_L^a(-)\tilde{\mathbf{V}}_L^{\frac{1}{2}}(+). \quad (2.65)$$

By following the same steps as in Eq. (2.64) and using  $\mathbf{V}_L\tilde{\mathbf{V}}_L^{\frac{1}{2}} = \mathbf{V}_L^{\frac{1}{2}}$  this can be simplified to

$$\mathbf{t} = i\mathbf{V}_R^{\frac{1}{2}}(+)\mathbf{U}_R^{-1}(+)\mathbf{G}^r\left[\mathbf{U}_L^a(-)\right]^{-1}\mathbf{V}_L^{\frac{1}{2}}(+). \quad (2.66)$$

Writing out the transmission matrix elements gives the compact expression

$$t_{n,m} = i\hbar\sqrt{\frac{v_{R,n}v_{L,m}}{a_R a_L}}\tilde{\mathbf{u}}_{R,n}^\dagger(+)\mathbf{G}_{S+1,0}(E)\tilde{\mathbf{u}}_{L,m}^a(-). \quad (2.67)$$

This is the tight-binding equivalent of the Fisher-Lee expression relating transmission and Green function matrices [65].

## 2.6 Examples

### 2.6.1 A simple analytical model

We consider a system consisting of a single impurity in a one-dimensional chain and treat this within a one-band nearest neighbor tight-binding model. The parameters

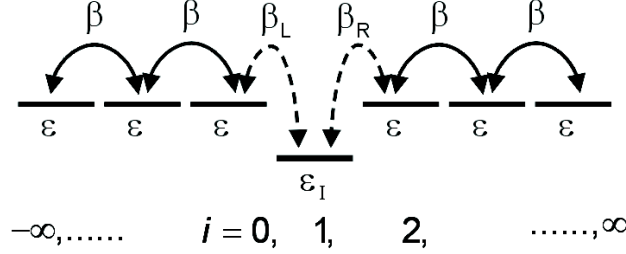


**Figure 2.2** : The parameters of a one-band nearest neighbor tight-binding model for a single impurity in a one-dimensional chain.

of this model are given in Fig. 2.2. This model can be solved analytically [107], so it can serve as a simple test to illustrate the equivalence of the different approaches.

We will first solve the problem using the mode matching approach of Sec. 2.3. It is convenient to define a scaled energy by

$$\omega \equiv \frac{E - \epsilon}{2\beta}. \quad (2.68)$$

The model involves only one channel and with  $\mathbf{u}_m(\pm) = 1$  Eq. (2.4) reduces to

$$-\beta + (E - \epsilon)\lambda(\pm) - \beta\lambda(\pm)^2 = 0, \quad (2.69)$$

The roots  $\lambda(\pm)$  can be given a more familiar form. For  $|\omega| \leq 1$  we define a wave number  $k$  by

$$\cos(ka) = \omega, \quad (2.70)$$

where  $a$  is the lattice parameter. From Eqs. (2.69), (2.70) one then obtains

$$\lambda(\pm) = e^{\pm ika}, \quad (2.71)$$

which describes propagating states. For  $|\omega| > 1$  one defines  $\kappa$  by

$$\cosh(\kappa a) = |\omega|. \quad (2.72)$$

One obtains  $\lambda(\pm) = \exp(\mp\kappa a)$  if  $\omega > 1$  and  $\lambda(\pm) = -\exp(\mp\kappa a)$  if  $\omega < -1$ ; both cases describe evanescent states.

Since the scattering region consists of a single impurity,  $S = 1$ , Eqs. (2.12)-(2.14) give three linear equations with three unknowns describing the scattering problem. In a one-channel model one has  $\mathbf{F}(\pm) = \lambda(\pm)$  and  $\lambda(\pm)^{-1} = \lambda(\mp)$ . There is only one possible incoming wave, so  $\mathbf{c}_0(+)$  = 1. The linear equations then become in matrix form

$$\mathbf{A} \begin{pmatrix} c_0 \\ c_1 \\ c_2 \end{pmatrix} = \begin{pmatrix} \beta[\lambda(-) - \lambda(+)] \\ 0 \\ 0 \end{pmatrix}, \quad (2.73)$$

with

$$\mathbf{A} = \begin{pmatrix} E - \epsilon - \beta\lambda(+), & -\beta_L & 0 \\ -\beta_L & E - \epsilon_I & -\beta_R \\ 0 & -\beta_R & E - \epsilon - \beta\lambda(+), \end{pmatrix}. \quad (2.74)$$

Solving this set of equations and using Eqs. (2.70) and (2.71) we obtain the compact expression

$$c_2 = e^{2ika} \frac{-if \sin(ka)}{d + (1-b) \cos(ka) - ib \sin(ka)}, \quad (2.75)$$

defining the dimensionless parameters

$$b = \frac{\beta_L^2 + \beta_R^2}{2\beta^2}, \quad d = \frac{\epsilon - \epsilon_I}{2\beta}, \quad f = \frac{\beta_L \beta_R}{\beta^2}. \quad (2.76)$$

Applying Eqs. (2.15)-(2.17) then yields for the total transmission probability

$$T(E) = |c_2|^2. \quad (2.77)$$

Using Eqs. (2.70) and (2.75) it is easy to show that this transmission probability is identical to Eq. (15) of Ref. [107], which was obtained using a different technique.

It is instructive to solve the same problem using the Green function approach of Sec. 2.4.1. First one has to find the surface Green functions of the leads from Eqs. (2.24) and (2.25), which for the current model become

$$[E - \epsilon - \beta^2 g(E)] g(E) = 1, \quad (2.78)$$

where  $E$  is a real energy. This equation has the solutions

$$g^\pm(E) = \frac{e^{\pm ika}}{\beta}, \quad (2.79)$$

for both leads. The Green function matrix in the scattering region can then be found from Eqs. (2.21) and (2.22), which can be combined in the  $3 \times 3$  matrix equation

$$\mathbf{A}\mathbf{G}(E) = \mathbf{I}, \quad (2.80)$$

where  $G_{i,j}(E)$ ,  $i, j = 0, \dots, 2$  are the matrix elements of  $\mathbf{G}(E)$  and  $\mathbf{A}$  is given by Eq. (2.74). Inverting  $\mathbf{A}$  yields the matrix element

$$G_{2,0}(E) = \frac{f}{2\beta} \frac{e^{2ika}}{d + (1-b) \cos(ka) - ib \sin(ka)}, \quad (2.81)$$

with the parameters  $b$ ,  $d$  and  $f$  defined by Eq. (2.76). The relevant Green function matrix element for the ideal lead is found from Eq. (2.34)

$$G_{0,0}^{(0)}(E) = \frac{i}{2\beta \sin(ka)}. \quad (2.82)$$

Using these results in Eq. (2.30) one observes that the expression for the (one channel) transmission matrix element becomes identical to Eq. (2.75).

Finally one can calculate the transmission probability from the Caroli expression given in Sec. 2.5.4, cf. Eq. (2.53). Using Eqs. (2.26), (2.54) and (2.79) one obtains

$$\Gamma_L = \Gamma_R = -2\beta \sin(ka), \quad (2.83)$$

for left and right leads. Using Eqs. (2.81), (2.83) and  $G_{0,2}^a = (G_{2,0})^*$  in Eq. (2.53) then yields an expression for the transmission probability that is identical to Eq. (2.77). It illustrates the equivalence of the different approaches for calculating the transmission in this simple model.

In addition to providing a channel for propagating states, an impurity can also give rise to localized states, whose energy is outside the energy band of the chain, cf. Eq. (2.72). Such a state does not contribute to the physical transmission, but the transmission amplitude has a pole at an energy that corresponds to a localized state [24]. Within the mode matching approach this corresponds to an energy at which  $c_{S+1}$  becomes infinite. For the present model the energies of localized states can be obtained by setting  $k = i\kappa$  and setting the denominator to zero in Eq. (2.75). This leads to the equation

$$(\omega + d) \left( \omega + \operatorname{sgn}(\omega) \sqrt{\omega^2 - 1} \right) - b = 0; \quad |\omega| > 1, \quad (2.84)$$

the roots of which give the energies of the localized states. Again these results are equivalent to the results obtained using the approach of Ref. [107].

Within the Green function approach the energies of the localized states are given by the poles of the Green function matrix. Via Eq. (2.81) this again leads to Eq. (2.84). Alternatively, since the Green function matrix is the inverse of the  $\mathbf{A}$ -matrix, cf. Eq. (2.80), its poles are given by the roots of  $\det(\mathbf{A}) = 0$ . This equation is equivalent to Eq. (2.84), as is easily shown by setting  $\lambda(\pm) = \pm \exp(-\kappa a)$  in the  $\mathbf{A}$ -matrix.

## 2.6.2 Fe|vacuum|Fe tunnel junction

As an example of a more complex system, we consider an Fe|vacuum|Fe tunnel junction where the electronic structure is treated using the local density approximation of DFT [19]. The calculations are based upon a tight-binding muffin tin orbital (TB-MTO) atomic spheres approximation (ASA) implementation [95, 103–105, 108] of the formalism described in Sect. 2.3.

The first step in the calculation is the self-consistent determination of the electronic structure of the tunnel junction using the layer Green function approach of Ref. [115]. The Fe leads are oriented in the (001) direction and the atoms at the Fe(001) surfaces are kept at their unrelaxed bulk positions. For the bcc structure and TB-MTOs [123], a principal layer in the (001) direction contains two monolayers of Fe with a thickness of 2.866 Å. The vacuum region is modeled by a number of such slices, of the same thickness, filled with “empty” spheres of the same size and packing as the Fe atomic spheres. The atomic sphere potentials of the vacuum

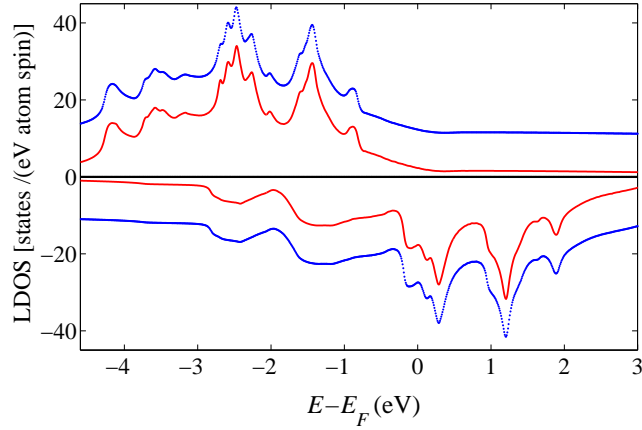


**Figure 2.3** : Layer density of states (LDOS) at the Fe(001) surface layer. Top panel: majority spin. Top curve (red, dashed): as calculated using the layer Green function method [115]. Bottom curve (blue, solid): as calculated using the mode matching approach. Both calculations use  $\eta = 0.0025$  Ry. For clarity, the top curve has been displaced by 10 units along the y-axis. Bottom panel: minority spin, the LDOS is shown with a negative sign.

region and four monolayers (two principal layers) of Fe on either side of the vacuum are calculated self-consistently while the potentials of more distant layers are kept at their bulk values. These potentials then form the input to a transmission calculation based on mode matching [95, 104, 105]. Further technical details can be found in Ref. [108].

A useful quantity to extract from the self-consistent layer calculation is the layer density of states (LDOS)  $\rho_i(E)$ . It is related to the retarded Green function matrix defined in Eq. (2.21) by

$$\rho_i(E + i\eta) = -\pi^{-1} \text{ImTr}[\mathbf{G}_{i,i}(E + i\eta)] \quad (2.85)$$

where the trace refers to the usual  $lm$  angular momentum indices characterizing MTOs. For reasons of numerical stability the retarded Green function matrix is calculated by adding a finite imaginary part to the energy; we have used  $\eta = 0.0025$  Ry. In the mode matching approach, the LDOS can be directly expressed in terms of the wave functions or, alternatively, in terms of the Green function matrix of Eq. (2.18)

$$\rho_i(E) = -\pi^{-1} \text{ImTr}[\mathbf{G}'_{i,i}(E)]. \quad (2.86)$$

This Green function matrix can be calculated for a real energy, but in order to make a comparison to the results obtained with Eq. (2.85), we add an imaginary part,  $\eta = 0.0025$  Ry.

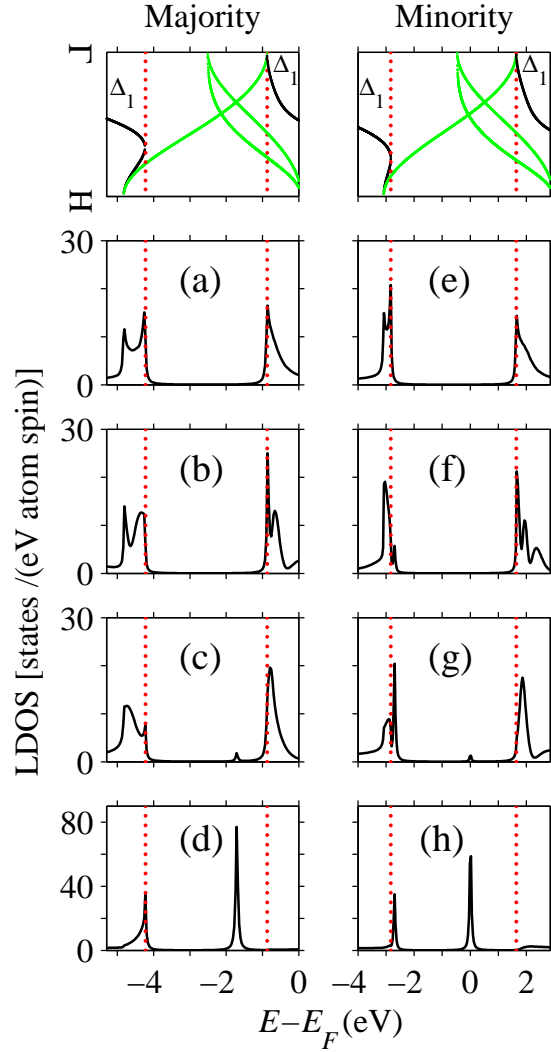


**Figure 2.4** : The top panels represent the band structures along  $\Gamma$ -H of bulk Fe for majority and minority spins. Panels (a-h) give the  $\Delta_1$  contribution to the LDOS  $\rho_i(E)$  at  $\bar{\Gamma}$  of the Fe|vacuum interface as a function of the layer position. (a) LDOS of an Fe layer at an infinite distance from the interface; the double peak structure below -4 eV and single peak (of a double peak structure) above -1 eV correspond to the  $\Delta_1$  bulk bands. (b) LDOS of the 6th Fe layer (the surface layer is layer 1). (c) LDOS of the 3rd Fe layer; the sharp peak in the bulk band gap corresponds to a surface state. (d) LDOS of the the surface Fe layer; the surface state peak has maximum amplitude. (e-h) Same for minority spin.



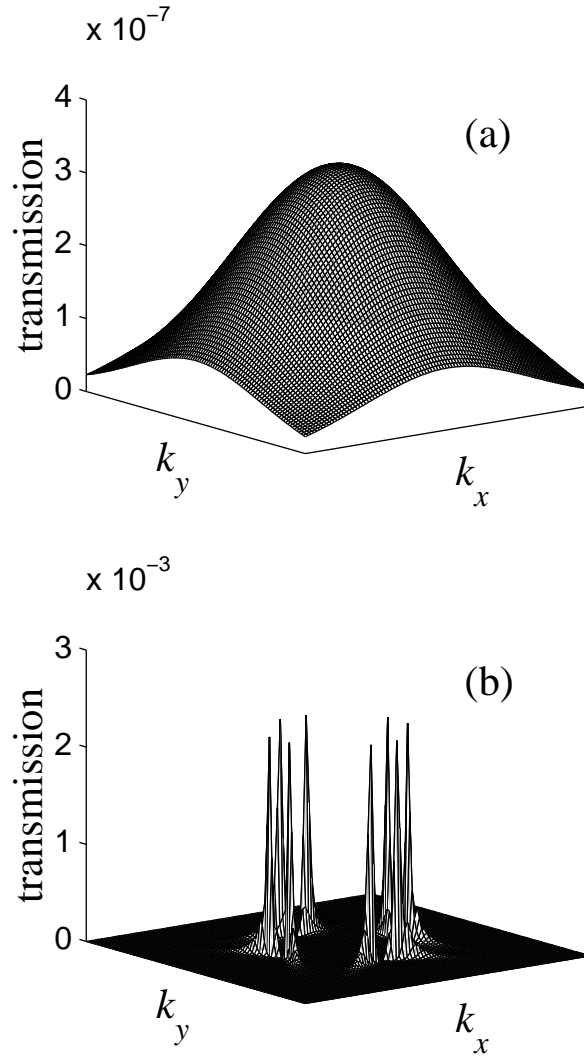


**Figure 2.5** : Calculated  $\mathbf{k}_{\parallel}$ -resolved transmission in (a) the majority and (b) the minority spin channels through a Fe-vacuum-Fe tunnel junction. The vacuum region has a thickness of  $5.733 \text{ \AA}$  and the Fe electrodes have a parallel magnetization. Only the central part of the Brillouin zone is shown, i.e.  $-\pi/3a \leq k_x, k_y \leq \pi/3a$ ; the transmission in the other parts is close to zero.

In Fig. 2.3 we compare the LDOS obtained using (2.85) and (2.86) for the topmost Fe monolayer of (001) Fe|vacuum|Fe where the vacuum layer was so thick (four principal layers, corresponding to a thickness of 11.466 Å) that the LDOS corresponds closely to that of a free Fe(001) surface. The two curves, displaced vertically for clarity, are indistinguishable, illustrating the equivalence of the two Green functions defined in (2.18) and (2.21). Moreover, the LDOS are in essential agreement with results found previously for a Fe(001) surface [124].

If one resolves the LDOS into contributions from different parts of the surface Brillouin zone, then the contribution at  $\bar{\Gamma}$  ( $\mathbf{k}_{\parallel} = 0$ ) exhibits sharp peaks near the Fermi level. These are associated with characteristic surface states found on (001) surfaces of bcc transition metals [125]. These surface states are mainly derived from  $d_{3z^2-r^2}$  orbitals on the surface atoms projecting into the vacuum, and they have  $\Delta_1$  symmetry [126, 127]. They become most clearly visible if one filters out the contribution to the LDOS at  $\bar{\Gamma}$  of the states with  $\Delta_1$  symmetry.

This contribution, calculated using the mode matching approach, is shown in Fig. 2.4 as a function of the distance from the surface. In the majority spin LDOS, a sharp peak is found at  $E_F - 1.8$  eV, which is very prominent in the surface Fe layer, cf. Fig. 2.4(d) and decays rapidly into the bulk, cf. Figs. 2.4(c)-(a). This evanescent state clearly represents a state that is localized at the surface. In the minority spin LDOS, a sharp peak with similar properties is found very close to  $E_F$ . It corresponds to the surface state that is observed experimentally by STM [125]. The positions of both these surface state peaks in the majority and minority LDOS are in excellent agreement with those obtained using a Green function (KKR) approach [126, 127]. Such surface states are good examples of evanescent states. Clearly, they are described properly within the mode matching approach which was, however, disputed in Ref. [106].

Using the mode matching approach, we next calculate the transmission through an Fe|vacuum|Fe tunnel junction in which the vacuum region is only 5.733 Å thick (corresponding to two principal layers) and the magnetizations are parallel. Fig. 2.5 shows the calculated  $\mathbf{k}_{\parallel}$ -resolved transmission for majority- and minority-spin channels. The majority conductance has a maximum at  $\bar{\Gamma}$  and it decreases smoothly going away from  $\bar{\Gamma}$ . This behavior is quite general for scattering from a potential barrier. At fixed energy, a wave travelling perpendicular to the vacuum barrier penetrates furthest into the vacuum and therefore has a maximum tunneling probability [128].

In contrast, the minority conductance is dominated by sharp spikes of very high intensity, close to  $0.13 \bar{\Gamma}\bar{X}$ . This behavior has been analyzed in terms of interface resonant states that extend relatively far into the vacuum. States originating from the two Fe|vacuum interfaces couple through the thin vacuum region, which enhances the transmission considerably [128]. These transmission spikes or “hot spots” are observed quite generally in calculations for perfect transition metal|insulator|transition metal tunnel junctions [129, 130]. A calculation using Eq. (2.30) gives the same transmission within numerical accuracy. It again illustrates the correct treatment of evanescent states within the mode matching approach. We have also tested expression (2.67) numerically and found that it too gives the same transmission within

numerical accuracy.

Finally, the invariance property of the transmission discussed in Sec. 2.5.3, has been tested numerically by moving the interfaces between the leads and the scattering region, where the matching is carried out, into the leads. In this way more and more slices of lead are treated as scattering region, see Fig. 2.1; the transmission should be invariant under this operation. Adding up to ten principal layers (20 monolayers) of bulk Fe to each side of the scattering region changes the transmission negligibly, by less than one part in  $10^8$ .

## 2.7 Summary

We have demonstrated the equivalence of the mode matching and the Green function approaches to calculating the conductance of quantum wires and interfaces. In the mode matching technique, the scattering problem is solved by matching the wave function in the scattering region to the Bloch modes in the leads. The technique is formulated for tight-binding Hamiltonians and covers all representations that can be expressed in tight-binding form, including first-principles implementations using localized orbital basis sets or a real-space grid.

Alternatively, the scattering information can be extracted from the Green function, which is calculated by partitioning the system into a scattering region and leads. We demonstrate that the Green function technique can be reformulated in terms of mode matching. In addition we prove that the mode matching expression for the transmission matrix does not depend on where in the leads the scattering region is matched to the ideal leads, which was called into question in Ref. [106].

Calculating the full transmission matrix allows us to study individual scattering amplitudes from and to every possible mode. We have derived a compact expression for the transmission matrix elements, Eq. (2.67). Only propagating modes enter this expression, since evanescent modes do not contribute to the transmission directly. The evanescent modes are important, however, for setting up the correct matching conditions at the boundaries between the scattering region and the leads. Alternatively, the total transmission probability can be calculated from the Caroli expression, Eq. (2.53). Formally this expression sums over all possible modes, i.e. propagating and evanescent. However, by deriving the Caroli expression from the mode matching approach we show explicitly that only the propagating modes give a non-zero contribution.

The mode matching approach and its equivalence to the Green function approach were illustrated for a simple analytical model, as well as by numerical calculations on an Fe|vacuum|Fe tunnel junction. In the latter we treat the electronic structure within DFT, using a TB-MTO-ASA basis set. We demonstrate that the layer densities of states that follow from the mode matching and Green function approaches are numerically indistinguishable. We identify the Fe(001) surface state in the density of states and establish its contribution to the transmission through the tunnel junction. Finally, the invariance property discussed above is demonstrated numerically on the Fe|vacuum|Fe tunnel junction.



## Chapter 3

# Real-space finite-difference method for conductance calculations

In this chapter we present a general method for calculating coherent electronic transport in quantum wires and tunnel junctions. It is based upon a real-space high-order finite-difference representation of the single particle Hamiltonian and wave functions. Landauer's formula is used to express the conductance as a scattering problem. Dividing space into a scattering region and left and right ideal electrode regions, this problem is solved by wave function matching (WFM) in the boundary zones connecting these regions. The method is tested on a model tunnel junction and applied to sodium atomic wires. In particular, we show that using a high-order finite-difference approximation of the kinetic energy operator leads to a high accuracy at moderate computational costs.

### 3.1 Introduction

The progress in experimental control on the nanometer scale has enabled studies of electronic transport in quantum wires of atomic dimensions [61]. The transport properties of such systems have to be understood on the basis of their atomic structure. This notion has generated a large effort in recent years to calculate the conductance of quantum wires from first principles. Several different approaches have been formulated, which have a common basis in the Landauer-Büttiker approach to express the conductance of a coherent system in terms of a quantum mechanical scattering problem [67]. In such calculations the quantum wire consists of a scattering region of finite size, sandwiched between two semi-infinite leads that are considered to be ideal ballistic wires. Semi-empirical tight-binding models have been exploited to solve this problem [102, 131–133]. Aiming at a better description of the electronic structure, several current approaches rely upon density functional theory (DFT).

The main differences between these approaches lie in the approximations that are used to describe the atomic structure of the leads and in the techniques that are used to solve the scattering problem. In pioneering work, jellium (i.e. free

electron) electrodes have been used to describe the leads and the scattering wave functions have been obtained by a transfer matrix method [134, 135] or by solving the Lippman-Schwinger equation [136–138]. A transfer matrix method has also been used taking into account the full atomic structure of the leads at the DFT level [139, 140]. Alternatively, the conductance can be calculated using a Green function approach without calculating the scattering wave functions explicitly [62]. Several implementations of this approach have been formulated that use a localized basis set to form a representation of the scattering problem. These implementations mainly differ in the kind of basis set used, e.g. Gaussian or numerical atomic orbitals, or wavelets [83, 84, 97, 99, 141–144]. An embedded Green function approach has been applied using a delocalized basis set of augmented plane waves [98].

In this chapter we present a technique for solving the scattering problem of a quantum wire without the use of a basis set. Instead, potentials and wave functions are represented on a uniform real space grid and differential operators are approximated by a finite difference approximation (FDA). Previous implementations of this idea have used a simple first order FDA [145–150]. In that case the grid has to be relatively fine in order to obtain sufficiently converged results. This hinders the application to large systems because of the computational costs involved in using fine grids. However, in ground state (DFT) electronic structure calculations high-order FDA's have been shown to markedly increase the efficiency of real-space grid techniques by enabling the use of coarse grids [37, 56, 151]. In this chapter we demonstrate that high-order FDA's make it possible to solve the scattering problem much more efficiently.

The method we propose for calculating the conductance of a quantum wire is based upon wave function matching (WFM) in the boundary zones connecting the leads and the scattering region [101]. Unlike transfer matrix methods, however, it does not require the explicit calculation of wave functions in the scattering region [134, 135, 139, 140]. It does not require the explicit calculation of Green functions either [62, 83, 84, 97–99, 141–144], which enables us to solve the scattering problem at real, instead of complex, energies.<sup>1</sup> Our method can be classified as an  $O(N)$  technique, since the computing costs are determined by the size of the scattering region with which they scale linearly. A related technique that uses a linearized muffin tin orbital basis set, has been applied to calculate the electronic transport in layered magnetic materials [104, 105]. Although the formalism presented here can be extended to the non-equilibrium situation, we consider in this chapter the linear response regime only.

This chapter is organized as follows. In Sec. 3.2 the main ingredients of our computational method are explained, where the computational details can be found in Appendix B. The accuracy and convergence properties of the method are verified on model tunnel junctions in Sec. 3.3.1. The application to a more complex system, which consists of a sodium atomic wire, is discussed in Sec. 3.3.2. A summary is given in Sec. 3.4.

---

<sup>1</sup>If one uses Green functions, one has to distinguish between retarded and advanced Green functions. This can be done by subtracting or adding a (small) imaginary number to the energy.

## 3.2 Computational Method

Within the Landauer-Büttiker approach the conductance  $G$  of a quantum wire is expressed in terms of the total transmission  $T(E)$

$$G = \frac{e^2}{\pi\hbar} T(E), \quad (3.1)$$

assuming spin degeneracy [67].  $T(E)$  can be obtained by solving the quantum mechanical scattering problem at the fixed energy  $E$ . Eq. (3.1) is valid in the linear response regime, where  $T(E)$  needs to be evaluated at the Fermi energy  $E = E_F$ . Our quantum wire is defined as a system consisting of a finite scattering region that is connected left and right to semi-infinite leads. The latter are supposed to be ‘ideal’ wires, which can be described by a periodic potential along the wire direction. In the scattering region the potential can have any shape. We consider two cases that can be treated by essentially the same technique. In the first case the system has a finite cross-section perpendicular to the wire direction, whereas in the second case the system is periodic perpendicular to the wire. The latter case also covers planar interfaces and tunnel junctions.

In order to solve the scattering problem we generalize a method formulated by Ando [101]. Here one basically solves a single particle Schrödinger equation directly at a fixed energy  $E$  in two steps. In the first step one obtains the modes of the ideal leads. Subsequently the wave functions for the scattering region are constructed such, that they are properly matched to the solutions in the leads. We use a real-space finite-difference method to represent the Schrödinger equation. In the following three subsections we will introduce this representation and discuss the steps required to solve the scattering problem.

### 3.2.1 Finite-difference approximation

We start from a single particle equation of the general form

$$\left( E - V(\mathbf{r}) + \frac{\hbar^2}{2m} \nabla^2 \right) \Psi(\mathbf{r}) = 0, \quad (3.2)$$

which represents the Schrödinger equation of a single particle in a potential  $V$ . Alternatively, within the DFT scheme it represents the Kohn-Sham equation with  $V$  the total effective potential. We put the wave function  $\Psi$  and the potential  $V$  on a equidistant grid in real space  $\mathbf{r} = (x_j, y_k, z_l)$ , where  $x_j = x_0 + jh_x$ ,  $y_k = y_0 + kh_y$ ,  $z_l = z_0 + lh_z$  and  $h_x, h_y, h_z$  are the grid spacings in  $x, y$  and  $z$  directions, respectively. Following Refs. [37, 56] we replace the kinetic energy operator in Eq. (3.2) by a high-order FDA. For the  $x$  part this gives

$$\frac{\partial^2 \Psi(x_j, y_k, z_l)}{\partial x^2} \approx \frac{1}{h_x^2} \sum_{n=-N}^N c_n \Psi(x_{j+n}, y_k, z_l), \quad (3.3)$$

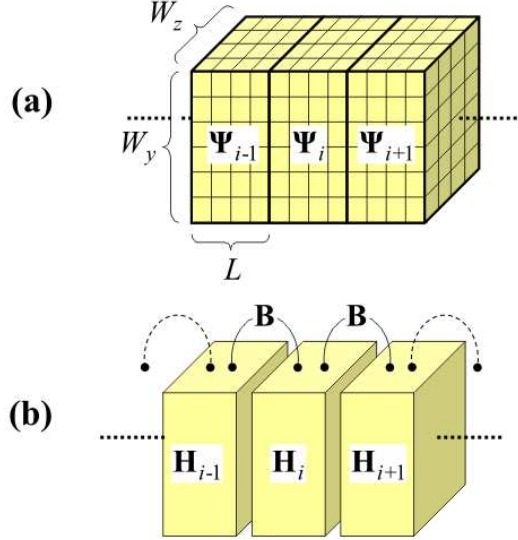


**Figure 3.1** : (a) The system is divided into cells indicated by an index  $i$ . The cells have  $L \cdot W_y \cdot W_z$  grid points in the  $x, y$  and  $z$  directions, respectively.  $\Psi_i$  is the supervector that contains the wave function values on all grid points in cell  $i$ . (b)  $\mathbf{H}_i$  is the Hamiltonian matrix connecting grid points within cell  $i$ ; the  $\mathbf{B}$ -matrix connects grid points between neighboring cells and is independent of  $i$ .

with similar expressions for the  $y$  and  $z$  parts. Expressions for the coefficients  $c_n$  for various values of  $N$  are tabulated in Ref. [56]. The simplest approximation in Eq. (3.3) ( $N = 1$ , where  $c_1 = c_{-1} = 1$  and  $c_0 = -2$ ) reduces Eq. (3.2) to the well-known simple finite-difference representation of the Schrödinger equation [62, 145–150]. However, we will demonstrate that the scattering problem can be solved much more efficiently using higher order FDA's with  $N = 4-6$ .

In a FDA the Schrödinger equation of Eq. (3.2) becomes

$$(E - V_{j,k,l}) \Psi_{j,k,l} + \sum_{n=-N}^N (t_n^x \Psi_{j+n,k,l} + t_n^y \Psi_{j,k+n,l} + t_n^z \Psi_{j,k,l+n}) = 0, \quad (3.4)$$

where  $V, \Psi_{j,k,l}$  is a short-hand notation for  $V, \Psi(x_j, y_k, z_l)$  and

$$t_n^{x,y,z} = \frac{\hbar^2 c_n}{2m h_{x,y,z}^2}.$$

In order to make a connection to Ando's formalism [101] we divide the wire into cells of dimension  $a_x \times a_y \times a_z$ . The direction of the wire is given by the  $x$ -axis. The number of grid points in a cell is  $L = a_x/h_x$ ,  $W_y = a_y/h_y$ ,  $W_z = a_z/h_z$  for the  $x, y$



and  $z$  directions respectively. We wish to distinguish between two different cases. In the first case the wire has a finite cross-section in the  $yz$  plane. In the second case the wire has an infinite cross-section, but it has a periodic potential in the  $yz$  plane, i.e.  $V_{j,k+W_y,l} = V_{j,k,l+W_z} = V_{j,k,l}$ . In both cases the (unit) cell in the  $yz$  plane is described by  $W_y \times W_z$  grid points.

The values  $\Psi_{j,k,l}$  where the indices  $j, k, l$  correspond to a single cell  $i$  are grouped into a supervector  $\Psi_i$ . The idea is shown in Fig. 3.1. This supervector has the dimension  $N_{\text{rs}} = L \cdot W_y \cdot W_z$ , which is the total number of real-space grid points in a cell. If we let  $i$  denote the position of the cell along the wire then Eq. (3.4) can then be rewritten as

$$(E\mathbf{I} - \mathbf{H}_i)\Psi_i + \mathbf{B}\Psi_{i-1} + \mathbf{B}^\dagger\Psi_{i+1} = 0, \quad (3.5)$$

for  $i = -\infty, \dots, \infty$ . Here  $\mathbf{I}$  is the  $N_{\text{rs}} \times N_{\text{rs}}$  identity matrix. The matrix elements of the  $N_{\text{rs}} \times N_{\text{rs}}$  matrices  $\mathbf{H}_i$  and  $\mathbf{B}$  can be derived straightforwardly from Eq. (3.4). The expressions are given in Appendix B.1, both for a wire that is finite and for a wire that is periodic in the  $yz$  plane. For the latter  $\mathbf{H}_i = \mathbf{H}_i(\mathbf{k}_\parallel)$ , where  $\mathbf{k}_\parallel$  is a wave vector in the two-dimensional Brillouin zone. In the following this notation is suppressed.

Eq. (3.5) has the form of a nearest neighbor tight-binding equation, expressed in terms of vectors/matrices of dimension  $N_{\text{rs}}$ . This form enables us to use Ando's technique to solve the scattering problem [101]. Note however that the matrices  $\mathbf{B}, \mathbf{B}^\dagger$  in Eq. (3.4) are singular, see Eq. (B.3), which requires a generalization of this technique.

### 3.2.2 Ideal wire

An ideal wire is defined by a potential that is periodic in the direction of the wire, i.e.  $V(x_j + a_x, y_k, z_l) = V(x_j, y_k, z_l)$  or  $V_{j+L,k,l} = V_{j,k,l}$ . Since the potential is the same in each cell, the matrix  $\mathbf{H}_i = \mathbf{H}$  in Eq. (3.5) is independent of the cell position  $i$ . In a periodic system the vectors in subsequent cells are related by the Bloch condition

$$\lambda\Psi_i = \Psi_{i+1}, \quad (3.6)$$

where  $\lambda = e^{ik_x a_x}$  with  $k_x$  real for propagating waves and complex for evanescent (growing or decaying) waves. Combining Eqs. (3.5) and (3.6) one then obtains the following generalized eigenvalue problem

$$\left[ \begin{pmatrix} E\mathbf{I} - \mathbf{H} & \mathbf{B} \\ \mathbf{I} & 0 \end{pmatrix} - \lambda \begin{pmatrix} -\mathbf{B}^\dagger & 0 \\ 0 & \mathbf{I} \end{pmatrix} \right] \begin{pmatrix} \Psi_i \\ \Psi_{i-1} \end{pmatrix} = 0. \quad (3.7)$$

Formally, the dimension of this problem is  $2N_{\text{rs}}$ . There are a number of trivial solutions, however, since  $\mathbf{B}, \mathbf{B}^\dagger$  are singular matrices. In Appendix B.2 it is shown how reduce the problem to its  $2N \cdot W_y \cdot W_z$  non-trivial solutions.

The non-trivial solutions of Eq. (3.7) can be divided into two classes. The first class comprises Bloch waves propagating to the right and evanescent waves decaying

to the right; the corresponding eigenvalues are denoted by  $\lambda(+)$ . The second class comprises Bloch waves propagating to the left or evanescent waves decaying to the left; the eigenvalues are denoted by  $\lambda(-)$ . The eigenvalues of the propagating waves have  $|\lambda(\pm)| = 1$  and for evanescent waves  $|\lambda(\pm)| \leq 1$ . The evanescent states come in pairs, since it is easy to show that for every solution  $\lambda(+)$  there is a corresponding solution  $\lambda(-) = 1/\lambda^*(+)$ . It can be shown that the propagating states also come in pairs, i.e. for every right propagating wave  $\lambda(+)$  there is a left propagating wave  $\lambda(-)$  [112].

It makes sense to keep only those evanescent waves for which  $1/\delta < |\lambda| < \delta$ , where  $\delta$  is a sufficiently large number. States with  $|\lambda|$  outside this interval are extremely fast decaying or growing. Such states are not important in matching an ideal wire to a scattering region. Typical of finite difference schemes there are also non-physical solutions to Eq. (3.7), which are related to so-called parasitic modes [152,153]. These are easily recognized and discarded since their  $|\lambda|$ 's are either extremely small or large and thus fall outside the selected interval. Moreover, these  $|\lambda|$ 's are very sensitive to the grid spacing and rapidly go to 0 or  $\infty$  if the grid spacing is decreased.

After filtering out the physical and useful solutions Eq. (3.7) we end up with  $M$  pairs of solutions  $\lambda_m(\pm)$ ;  $m = 1, \dots, M$ , where usually  $M \ll N_{\text{rs}}$ . We construct the normalized vectors  $\mathbf{u}_m(\pm)$  from the first  $N_{\text{rs}}$  elements of the eigenvectors of Eq. (3.7) and form the  $N_{\text{rs}} \times M$  matrices

$$\mathbf{U}(\pm) = (\mathbf{u}_1(\pm) \cdots \mathbf{u}_M(\pm)). \quad (3.8)$$

Choosing the cell  $i = 0$  as the origin, one then writes the general solution  $\Psi_0$  in this cell as a linear combination of these right- and left going modes

$$\Psi_0 = \Psi_0(+) + \Psi_0(-), \quad (3.9)$$

where

$$\Psi_0(\pm) = \mathbf{U}(\pm)\mathbf{a}(\pm) = \sum_{m=1}^M \mathbf{u}_m(\pm)a_m(\pm), \quad (3.10)$$

with  $\mathbf{a}(\pm)$  vectors of arbitrary coefficients of dimension  $M$ .

Defining the  $M \times M$  diagonal eigenvalue matrices by

$$(\mathbf{\Lambda}(\pm))_{nm} = \delta_{nm}\lambda_m(\pm), \quad (3.11)$$

and using the Bloch condition of Eq. (3.6), the solution in the other unit cells then can be expressed in a compact form

$$\Psi_i = \mathbf{U}(+)\mathbf{\Lambda}^i(+)\mathbf{a}(+) + \mathbf{U}(-)\mathbf{\Lambda}^i(-)\mathbf{a}(-). \quad (3.12)$$

In order to apply Ando's formalism [101], it is advantageous to slightly rewrite this. We define the  $N_{\text{rs}} \times N_{\text{rs}}$  matrices  $\mathbf{F}(\pm)$  and  $\tilde{\mathbf{F}}(\pm)$  by

$$\mathbf{F}(\pm)\mathbf{U}(\pm) = \mathbf{U}(\pm)\mathbf{\Lambda}(\pm), \quad (3.13)$$

$$\tilde{\mathbf{F}}(\pm)\mathbf{U}(\pm) = \mathbf{U}(\pm)\mathbf{\Lambda}^{-1}(\pm). \quad (3.14)$$

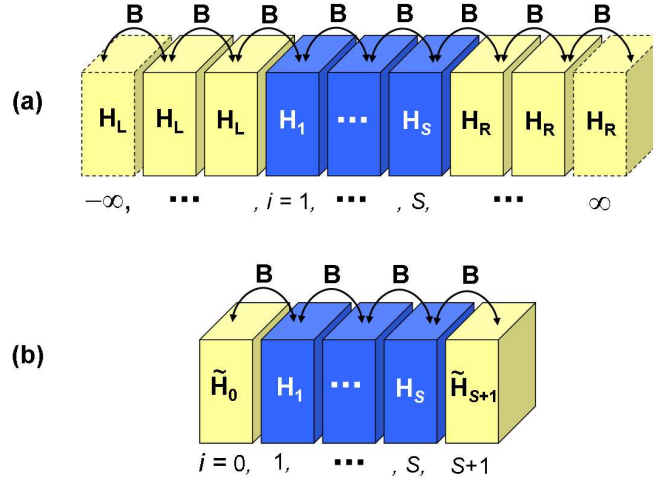


**Figure 3.2 :** (a) Schematic representation of a quantum wire. The left ( $L$ ) and right ( $R$ ) leads are ideal wires that span the cells  $i = -\infty, \dots, 0$  and  $i = S + 1, \dots, \infty$ , respectively. The scattering region spans cells  $i = 1, \dots, S$ . (b) The reduced problem spans the cells  $i = 0, \dots, S + 1$ , see Eq. (3.26).

Note that  $\tilde{\mathbf{F}}(\pm) \neq \mathbf{F}^{-1}(\pm)$  since the  $N_{\text{rs}} \times M$  matrices  $\mathbf{U}(\pm)$  are not square (typically  $M \ll N_{\text{rs}}$ ). This presents no problem, however, and explicit expressions for the matrices  $\tilde{\mathbf{F}}, \mathbf{F}$  are given in Appendix B.3. They allow Eq. (3.12) to be rewritten in recursive form

$$\Psi_{i+1} = \mathbf{F}(+) \Psi_i(+) + \mathbf{F}(-) \Psi_i(-), \quad (3.15)$$

$$\Psi_{i-1} = \tilde{\mathbf{F}}(+) \Psi_i(+) + \tilde{\mathbf{F}}(-) \Psi_i(-), \quad (3.16)$$

either of which allows one to construct the full solution for the ideal wire, once the boundary values are set, cf. Eq. (3.9).

### 3.2.3 Scattering problem

In a non-ideal quantum wire the potential is not periodic, which means that we have to solve the Schrödinger equation of Eq. (3.5) with  $\mathbf{H}_i$  depending upon the position  $i$  along the wire. The non-ideal region (the scattering region) is supposed to be finite, spanning the cells  $i = 1, \dots, S$ .<sup>2</sup> The left and right leads are ideal wires, spanning

<sup>2</sup>The size of the scattering region does not have to be an integer multiple of the size of the cell the leads. One can choose cells of a different size in the scattering region. One also chooses differently sized cells in the left and right leads in case the leads are different. We have not introduced cells of different size here in order not to complicate the notation, but the strategy for solving the scattering problem as outlined in Appendix B.4 also works in that case.

the cells  $i = -\infty, \dots, 0$  and  $i = S + 1, \dots, \infty$ , respectively. In the ideal wires  $\mathbf{H}_i$  does not depend on the position of the cell. However, the left lead can be different from the right one, so we use the subscript L(R) to denote the former(latter), i.e.  $\mathbf{H}_i = \mathbf{H}_L$ ,  $i < 1$  and  $\mathbf{H}_i = \mathbf{H}_R$ ,  $i > S$ . A schematic picture of the structure is shown in Fig. 3.2(a). We solve Eq. (3.5) over the whole space,  $i = -\infty, \infty$ , making use of the ideal wire solutions of the previous section to reduce the problem to essentially the scattering region only, see Fig. 3.2(b).

For the solution in the left lead the recursion relation of Eq. (3.16) can be used. This gives for the cell  $i = -1$

$$\begin{aligned}\Psi_{-1} &= \tilde{\mathbf{F}}_L(+)\Psi_0(+) + \tilde{\mathbf{F}}_L(-)\Psi_0(-) \\ &= [\tilde{\mathbf{F}}_L(+)-\tilde{\mathbf{F}}_L(-)]\Psi_0(+) + \tilde{\mathbf{F}}_L(-)\Psi_0,\end{aligned}\quad (3.17)$$

using Eq. (3.9). The vector  $\Psi_0(+)$  describes a wave coming in from the left. In a scattering problem this vector fixes the boundary condition. Eq. (3.17) allows Eq. (3.5) for  $i = 0$  to be written as

$$(E\mathbf{I} - \tilde{\mathbf{H}}_0)\Psi_0 + \mathbf{B}^\dagger\Psi_1 = \mathbf{Q}\Psi_0(+), \quad (3.18)$$

where

$$\begin{aligned}\tilde{\mathbf{H}}_0 &= \mathbf{H}_L - \mathbf{B}\tilde{\mathbf{F}}_L(-) \\ \mathbf{Q} &= \mathbf{B}[\tilde{\mathbf{F}}_L(-) - \tilde{\mathbf{F}}_L(+)].\end{aligned}\quad (3.19)$$

For the solution in the right lead we use the recursion relation of Eq. (3.15), which gives for the cell  $i = S + 2$

$$\Psi_{S+2} = \mathbf{F}_R(+)\Psi_{S+1}(+). \quad (3.20)$$

Here we have assumed that in the right lead we have only a right going wave, which corresponds to the transmitted wave. Eq. (3.20) allows Eq. (3.5) for  $i = S + 1$  to be written as

$$(E\mathbf{I} - \tilde{\mathbf{H}}_{S+1})\Psi_{S+1} + \mathbf{B}\Psi_S = 0, \quad (3.21)$$

where

$$\tilde{\mathbf{H}}_{S+1} = \mathbf{H}_R - \mathbf{B}^\dagger\mathbf{F}_R(+). \quad (3.22)$$

Eqs. (3.19) and (3.22) take care of the coupling of the scattering region to the left and right leads. Eq. (3.5) for  $i = 1, \dots, S$  plus Eqs. (3.18) and (3.21) form a complete set of equations from which the vectors  $\Psi_i; i = 0, \dots, S + 1$  can be determined describing the waves in the scattering region.

The scattering reflection and transmission coefficients can be deduced from the amplitudes immediately left and right of the scattering region, i.e.  $\Psi_0$  and  $\Psi_{S+1}$ . If we let the incoming wave consist of one specific mode,  $\Psi_0(+) = \mathbf{u}_{L,n}$ , i.e.  $a_m(+)$  =

$\delta_{mn}$  in Eq. (3.9), then the generalized reflection and transmission probability amplitudes  $r_{n'n}$  and  $t_{n'n}$  are defined by

$$\begin{aligned}\Psi_0(-) &= \sum_{n'=1}^{M_L} \mathbf{u}_{L,n'}(-) r_{n'n} \\ \Psi_{S+1}(+) &= \sum_{n'=1}^{M_R} \mathbf{u}_{R,n'}(+) t_{n'n}.\end{aligned}\quad (3.23)$$

Note that at this stage we include all evanescent and propagating modes since these form a complete set to represent the states in the leads. We assume the lead states to be amplitude normalized.

The reflection and transmission probability amplitudes  $r_{n'n}$  and  $t_{n'n}$  between all possible modes form a  $M_L \times M_L$  matrix  $\mathbf{R}$  and a  $M_R \times M_L$  matrix  $\mathbf{T}$ , respectively. All elements of these matrices can be found in one go by defining a  $N_{\text{rs}} \times M_L$  matrix of all possible incoming modes, i.e.

$$\mathbf{C}_0(+) = \mathbf{U}_L(+). \quad (3.24)$$

Analogous to Eq. (3.23) one then has

$$\begin{aligned}\mathbf{C}_0(-) &= \mathbf{C}_0 - \mathbf{C}_0(+) = \mathbf{U}_L(-)\mathbf{R} \\ \mathbf{C}_{S+1}(+) &= \mathbf{C}_{S+1} = \mathbf{U}_R(+)\mathbf{T}.\end{aligned}\quad (3.25)$$

Eqs. (3.18), (3.5) and (3.21) then become

$$\begin{cases} (\mathbf{E}\mathbf{I} - \tilde{\mathbf{H}}_0)\mathbf{C}_0 + \mathbf{B}^\dagger\mathbf{C}_1 = \mathbf{Q}\mathbf{U}_L(+) \\ (\mathbf{E}\mathbf{I} - \mathbf{H}_i)\mathbf{C}_i + \mathbf{B}\mathbf{C}_{i-1} + \mathbf{B}^\dagger\mathbf{C}_{i+1} = 0 \\ (\mathbf{E}\mathbf{I} - \tilde{\mathbf{H}}_{S+1})\mathbf{C}_{S+1} + \mathbf{B}\mathbf{C}_S = 0, \end{cases} \quad (3.26)$$

$i = 1, \dots, S$ . Solving this set of equations for  $\mathbf{C}_i$ ;  $i = 0, \dots, S + 1$  gives all possible waves. From Eq. (3.25) one can then extract the generalized reflection and transmission matrices  $\mathbf{R}$  and  $\mathbf{T}$ . An efficient technique for solving the equations is discussed in Appendix B.4.

In order to calculate the total transmission one has to select the transmission matrix elements that refer to propagating modes and discard the ones that refer to evanescent modes. This is easy, since the propagating modes have  $|\lambda| = 1$ , see the discussion above Eq. (3.8). The total transmission of Eq. (3.1) is then given by

$$T(E) = \sum_{n=1, n'=1}^{m_L, m_R} \frac{v_{R,n'} a_{x,L}}{v_{L,n} a_{x,R}} |t_{n'n}|^2, \quad (3.27)$$

where  $v_{R,n'}$  and  $v_{L,n}$  are the velocities in the  $x$ -direction of the right propagating waves in the right and left lead in the modes  $n'$  and  $n$ , respectively, and  $m_L, m_R$  are the number of such modes;  $a_{x,L}$  and  $a_{x,R}$  are the slice thickness of left and right

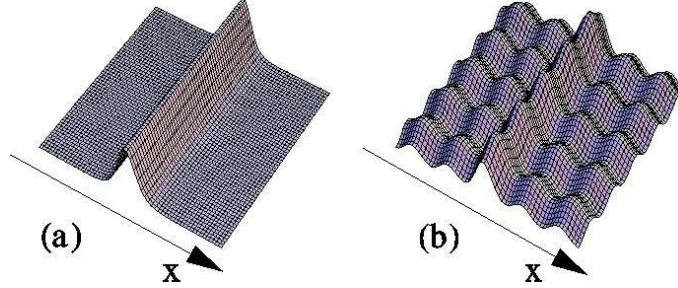


**Figure 3.3** : The potential of Eq. (3.29) in the  $xy$ -plane for the cases (a)  $V_0 = 0$  and (b)  $V_0 = V_1$ .

leads<sup>3</sup>. Introducing the velocities results from flux normalizing the modes, which is required by current conservation [62]. The velocities are given by the expression

$$v_n = \frac{2a_x}{\hbar} \text{Im} [\lambda_n \mathbf{u}_n^\dagger \mathbf{B}^\dagger \mathbf{u}_n], \quad (3.28)$$

where subscripts L(R) need to be added for the left(right) leads. Eq. (3.28) is derived in Appendix B.5. The sign of the calculated velocities is used to distinguish right from left propagating modes.

### 3.2.4 Computational costs

Our computational method can be summarized as follows. First, Eq. (3.7) is solved in its reduced form, Eq. (B.8), to obtain the modes for both leads. The computing costs of this step scale as  $N_{\text{id}}^3$ , where  $N_{\text{id}} = \max(2N, L - N) \cdot W_y \cdot W_z$ , see Appendix B.2. These costs are small compared to the costs of solving the scattering problem. The next step involves the selection of the physically relevant modes  $\mathbf{u}_m$  and separate them into left (+) and right (-) going modes. The velocities are calculated using Eq. (3.28) and are used to distinguish left from right propagating states. Evanescent states are classified as growing (+) or decaying (-) on account of their eigenvalue. Subsequently, the  $\mathbf{F}$ -matrices are constructed, Eq. (3.13), and the matrix elements that define the boundary conditions on the scattering region are set, see Eqs. (3.19) and (3.22). The computing costs of these steps are minor.

The transmission matrix  $\mathbf{T}$  is obtained by solving Eq. (3.26) using the algorithm of Appendix B.4. This is the most time consuming step. It scales as  $S \cdot N_{\text{rs}}^3$ , where  $N_{\text{rs}} = L \cdot W_y \cdot W_z$  is the number of grid points in the unit cell and  $S$  is the number of unit cells in the scattering region. Note that the scaling is linear with respect to the size  $S$  of the scattering region, which means that this algorithm can be classified as  $O(N)$ . Finally, the total transmission and the conductance can be obtained from Eqs. (3.27) and (3.1).

<sup>3</sup>The current per mode is given by velocity  $\times$  density. Since we normalize a mode in a slice, its density is given by  $1/\text{thickness of the slice}$ .

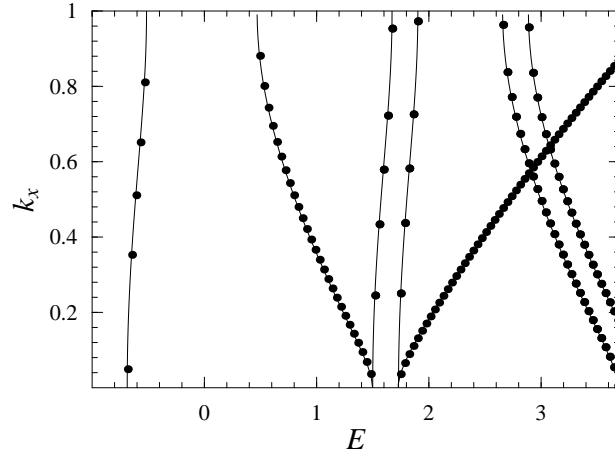


**Figure 3.4** : The calculated wave number  $k_x$  (in units of  $\pi/a$ ) as function of the energy  $E$  (in units of  $V_0$ ) for an ideal wire. The points indicate the numerical results obtained with  $L, W_y, W_x = 8$  and  $N = 4$ . The solid line indicates the exact solution of the Mathieu problem.

### 3.3 Results

#### 3.3.1 Numerical tests

In order to test the accuracy of our method we consider a system described by the model potential

$$V(\mathbf{r}) = V_0 [\cos(2\pi x/a) + \cos(2\pi y/a) + \cos(2\pi z/a)] + \frac{V_1}{\cosh^2(\pi x/a)}. \quad (3.29)$$

The  $V_0$  term describes an ideal wire by a simple three dimensional periodic potential with periods  $a_x = a_y = a_z = a$ . The  $V_1$  term describes a barrier in the propagation direction and is a simple model for a tunnel junction. The potential is plotted in Fig. 3.3. We solve the scattering problem for this system numerically in three dimensions by the method outlined in Sec. 3.2. Our results can be verified, however, since this potential is in fact separable and limiting cases can be solved analytically. The solutions in the  $y$ - and  $z$ -directions are Mathieu functions [154]. If  $V_1 = 0$  then the solutions in the  $x$ -direction are also Mathieu functions. If  $V_1 \neq 0$  but  $V_0 = 0$  the scattering problem can be solved analytically [24]. Finally, if  $V_1 \neq 0$  and  $V_0 \neq 0$  the solution in the  $x$  direction can be obtained using the separability of the potential and a standard numerical solver for the resulting ordinary differential equation in the  $x$ -direction [155]. In the following the latter will be called the “exact” numerical solution.

Table 3.1:  $k_x(E)$  (in units of  $\pi/a$ ) at values of  $E$  (in units of  $V_0$ ) in the lowest two bands and in the first band gap of Fig. 3.4; in the band gap we find  $k_x = 1 + i\kappa_x$ .

$N$	$L$	$k_x(-0.6)$	$k_x(1.0)$	$\kappa_x(0.3)$
1	7	0.694906	0.283091	0.283549
	10	0.608958	0.322712	0.304238
	14	0.571387	0.342011	0.312259
	100	0.533341	0.359187	0.319658
	1000	0.533084	0.359425	0.319688
4	5	0.544347	0.355049	0.317777
	7	0.533962	0.358927	0.319476
	10	0.533149	0.359389	0.319673
	14	0.533087	0.359425	0.319687
6	7	0.533228	0.359337	0.319658
	10	0.533086	0.359425	0.319688
	14	0.533082	0.359428	0.319688
Exact		0.533082	0.359428	0.319688

As a first test we consider an ideal wire, i.e.  $V_1 = 0$  in Eq. (3.29). The potential is separable and we can write the energy as  $E(k_x, k_y, k_z) = \epsilon_{n_x}(k_x) + \epsilon_{n_y}(k_y) + \epsilon_{n_z}(k_z)$ , where  $\epsilon_n(k)$ ;  $k = -\pi/a, \dots, \pi/a$ ;  $n = 0, 1, \dots$  are the eigenvalues of the Mathieu problem [154]. Fig. 3.4 shows part of the analytical band structure for  $(k_x, k_y, k_z) = (0, 0, 0) \rightarrow (\pi/a, 0, 0)$ . It essentially consists of a superposition of one-dimensional band structures  $\epsilon_{n_x}(k_x)$  offset by energies  $\epsilon_{n_y}(0) + \epsilon_{n_z}(0)$ ;  $n_y, n_z = 0, 1, \dots$

The numerical band structure is obtained by solving Eq. (3.7) in its reduced form, Eq. (B.8). To obtain the results shown in Fig. 3.4 we set  $\mathbf{k}_{\parallel} = (k_y, k_z) = (0, 0)$ , cf. Eq. (B.4), and determine the eigenvalues  $\lambda$  in Eq. (3.7) as a function of  $E$ . For the propagating states one can write  $\lambda = \exp(ik_x a)$ . Plotting the calculated wave number  $k_x$  as function of the energy  $E$  then allows to compare the results with the analytical band structure. The numerical results shown in Fig. 3.4 are obtained using a grid of  $L, W_y, W_z = 8$  points per period and a FDA with  $N = 4$ . Although this grid is relatively coarse, we obtain a relative accuracy on  $k_x$  of  $10^{-3}$ .

This perhaps surprising accuracy is entirely due to the use of a high-order FDA. To illustrate this, Table 3.1 shows the convergence of  $k_x$  at a number of energies  $E$  as a function of the order  $N$  of the FDA and the number of grid points  $L$ . These particular results were obtained using the separability of the potential and solving the problem numerically in the  $x$ -direction only, while using analytical solutions for the  $y$ - and  $z$ -directions. For  $N = 6$  and  $L = 14$  the results are converged to within  $10^{-7}$  of the exact result. This is in sharp contrast to the results obtained with a simple first order ( $N = 1$ ) FDA, where a similar convergence can only be obtained at the cost of using two orders of magnitude more grid points. Using such a large number of grid points in three dimensions is entirely prohibitive because of the high computational costs involved. For example, aiming at a moderate accuracy of  $10^{-2}$ , it



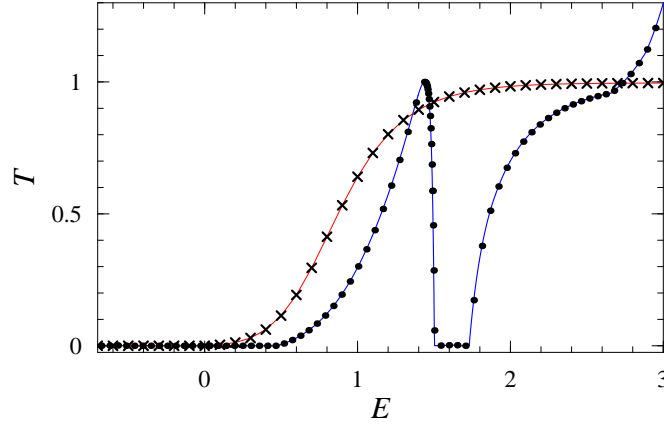


**Figure 3.5** : The total transmission as function of energy (in units of  $V_1$ ) for the two cases  $V_0 = 0$  (crosses) and  $V_0 = V_1$  (dots). In both cases  $\mathbf{k}_{\parallel} = (0, 0)$ . The solid lines represent the analytical solution for  $V_0 = 0$  and the “exact” numerical solution for  $V_0 = V_1$ .

is observed that for  $N = 4$  and  $L = 5$  the results are markedly better than for  $N = 1$  and  $L = 14$ . Yet in a three dimensional calculation, without using the separability of the potential, the computing time required for the latter is two orders of magnitude larger than for the former. It means that in order to solve a general non-separable three dimensional problem with reasonable accuracy and computational costs, it is vital to use a high-order FDA.

Next we consider the scattering problem and calculate the total transmission for the case where  $V_1 \neq 0$ . The size of the scattering region is set to  $Sa$  and outside this region the scattering potential (the last term of Eq. (3.29)) is set to zero. With  $S = 6$  the results are extremely well converged. As an example we have calculated the transmission at normal incidence, i.e.  $\mathbf{k}_{\parallel} = (k_y, k_z) = (0, 0)$ . The crosses marked  $V_0 = 0$  in Fig. 3.5 represent the numerical results for the transmission of the corresponding potential, obtained with a  $L, W_y, W_z = 8$  grid and a  $N = 4$  FDA. This scattering problem can also be solved analytically [24], and the analytical and numerical transmission probabilities agree within  $10^{-4}$ .

Fig. 3.5 also shows the transmission for the case where  $V_0 = V_1$  as calculated numerically using the same parameters as before, i.e.  $S = 6$ ;  $L, W_y, W_z = 8$ ;  $N = 4$ . This scattering problem can only be solved semi-analytically; Mathieu solutions are used in  $y$ - and  $z$ -directions, and the (ordinary) differential equation for the  $x$ -direction is solved “exactly” using an accurate standard numerical solver [155]. Again the “exact” and numerical transmission probabilities agree within  $10^{-4}$ . Compared to the  $V_0 = 0$  case it is observed that the influence of the periodic potential of the leads

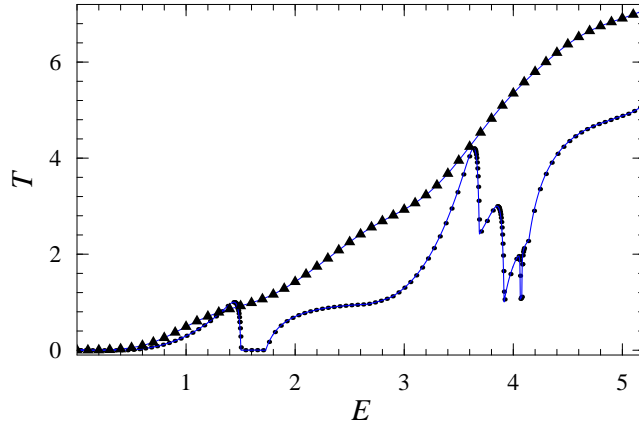


**Figure 3.6** : The total transmission as function of energy (in units of  $V_1$ ) for the two cases  $\mathbf{k}_{\parallel} = (0, 0)$  (dots) and  $\mathbf{k}_{\parallel} = (0.47, 0.21)\pi/a$  (triangles). In both cases  $V_0 = V_1$ . The solid lines represent the “exact” numerical solution.

upon the transmission is large. For  $V_0 = V_1$  the electronic states in the leads are far from free electron-like, see Fig. 3.4. In particular, the transmission drops to zero if the energy is inside a band gap, because there are no lead states of that energy.

The numerical calculations accurately capture the transmission curve over a large energy range, as is shown in Fig. 3.6. The transmission generally increases with energy due to the increasing number of channels, see Fig. 3.4. Since the density of states peaks at the band edges, the transmission peaks at the corresponding energies. The transmission depends very much upon  $\mathbf{k}_{\parallel}$  as can be observed in Fig. 3.6, where the transmission for normal incidence,  $\mathbf{k}_{\parallel} = (0, 0)$ , can be compared to that for  $\mathbf{k}_{\parallel} = (0.47, 0.21)\pi/a$  (an arbitrary point in the Brillouin zone). The difference between the two curves can be easily understood from the band structure of the leads. In particular, for  $\mathbf{k}_{\parallel} = (0.47, 0.21)\pi/a$  there are no band gaps for  $E > 0.14V_0$ .

To demonstrate the convergence of the numerical calculations, Fig. 3.7 shows the total transmission as function of the sampling density  $L = W_y = W_z$  for a simple  $N = 1$  and a high-order  $N = 4$  FDA. The results shown are for one particular  $\mathbf{k}_{\parallel} = (k_y, k_z) = (0.47, 0.21)\pi/a$  and energy  $E = 0.895 V_0$ , but the convergence at other  $\mathbf{k}_{\parallel}$ -points and energies is very similar. The number of propagating channels at this  $\mathbf{k}_{\parallel}$ -point and energy is two, but the total transmission is only  $T = 0.132$ , which means that the barrier is largely reflecting. We conclude that the accuracy of the three-dimensional calculation depends very strongly upon the order of the FDA. For  $N = 1, L = 15$ , the transmission is converged on a scale of  $10^{-2}$  only, but for  $N = 4$  it is converged on a scale of  $10^{-3}$  already for  $L = 8$ , see the inset of Fig. 3.7. A high-order FDA thus enables the use of a much coarser real-space grid. Since the

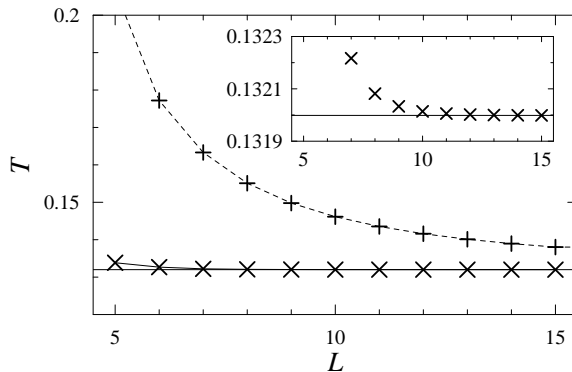


**Figure 3.7** : The total transmission  $T$  as function of the grid size  $L = W_y = W_z$  for a simple  $N = 1$  FDA, ‘+’ top curve, and for a  $N = 4$  FDA, ‘x’ bottom curve. The horizontal line represents the “exact” value  $T = 0.132$ . The inset shows the  $N = 4$  curve on a finer scale for  $T$ .

computational costs scale with the number of real-space grid points  $N_{\text{rs}} = L^3$  as  $N_{\text{rs}}^3 = L^9$ , this demonstrates the strength of using a high order FDA.

### 3.3.2 Sodium atomic wires

We have calculated the electronic transport in sodium atomic wires as examples of more complex systems. Our model of a sodium wire consists of left and right leads composed of bulk (bcc) sodium metal terminated by a (100) surface, connected by a straight wire of sodium atoms, as is shown in Fig. 3.8. The atoms in the leads are positioned according to the bcc structure of bulk sodium, with the cell parameter fixed at the experimental value of  $7.984 a_0$  [156]. The atoms in the wire are fixed at their (bulk) nearest neighbor distance of  $6.915 a_0$ . Since geometry relaxation at the Na(100) surface is very small [157], and calculations using jellium electrodes have shown that the conductance of a sodium wire is not very sensitive to its geometry [158], we have refrained from optimizing the geometry. Perpendicular to the wire we apply periodic boundary conditions using a  $2 \times 2$  lateral supercell, which has a lattice parameter of  $15.968 a_0$ .

If DFT is used to model the electronic structure, Eq. (3.2) corresponds to the Kohn-Sham equation. The one-electron potential  $V(\mathbf{r})$  in this equation is then given by the sum of the nuclear Coulomb potentials or pseudopotentials, and the electronic Hartree and exchange-correlation potentials. The latter two depend upon the electronic charge density. In linear response the charge density remains that of the ground state, allowing the electronic potentials to be obtained from a self-consistent ground state calculation. In these calculations we employ supercells containing a slab

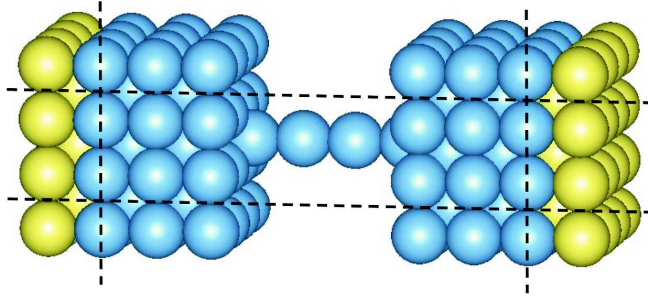


**Figure 3.8** : Structure of an atomic wire consisting of 4 sodium atoms between two sodium leads terminated by (100) surfaces. The scattering region is bounded by the vertical lines and the lateral supercell by the horizontal lines. Bulk atoms are indicated by yellow (light grey) balls and atoms in the scattering region by blue (dark grey) balls, respectively.

of 13 layers to represent the bulk and surface of the leads, and a wire of  $n$  atoms, see Fig. 3.8. We use the local density approximation [19], and represent the ion cores of the sodium atoms by a local pseudopotential [45]. The  $s$ -part of the pseudopotential for sodium, generated with a core radius  $r_c = 2.95 a_0$  is used as local potential. Tests using a non-local pseudopotential with  $s$ - and  $p$ -parts gave a virtually identical electronic structure for bulk sodium, indicating that the use of a local potential is a good approximation for sodium. The valence electronic wave functions are expanded in a plane wave basis set with a kinetic energy cutoff of 16 Ry. The lateral Brillouin zone is sampled with a  $8 \times 8$   $\mathbf{k}_{\parallel}$ -point grid, using a temperature broadening with  $kT_{el} = 0.1$  eV [55].

We want to calculate the conductance for various lengths of the atomic wire, so for each length  $n$  we perform a self-consistent supercell calculation to generate the one-electron potential. By expressing the latter in a plane wave basis, Fourier interpolation can be used to obtain a representation on any real-space grid required for the transport calculations, cf. Eq. (3.4). An example of the effective potential for valence electrons of a sodium atomic wire is shown in Fig. 3.9.

For the transport calculations we use a scattering region comprising the atomic wire and the surface regions of the left and right leads. Both surface regions consist of 5 atomic layers, see Fig. 3.8. Periodic boundary conditions and a  $2 \times 2$  lateral supercell perpendicular to the wire are applied. The potential in the scattering region is extracted from the slab calculations. Outside the scattering region we assume that the leads consist of bulk sodium. The potential for the leads and the value of the Fermi energy are extracted from a bulk calculation. The average bulk potential is lined up with the average potential in the middle of the supercell slab [159]. We have checked that the spatial dependence of the bulk potential is virtually identical to that of the potential in the middle of the slab. This means that the connection

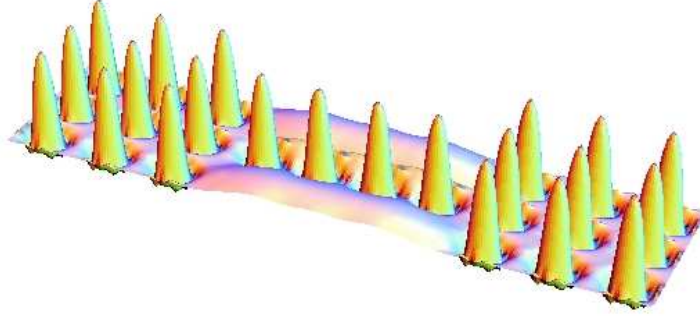


**Figure 3.9** : The effective potential for valence electrons in the  $xy$ -plane of the sodium atomic wire shown in Fig 3.8. Most prominent are the strongly repulsive core regions and the attractive valence regions of the atoms. The difference between the maximum and minimum values of this potential is 32.4 eV. The Fermi level is at 8.5 eV above the potential minimum.

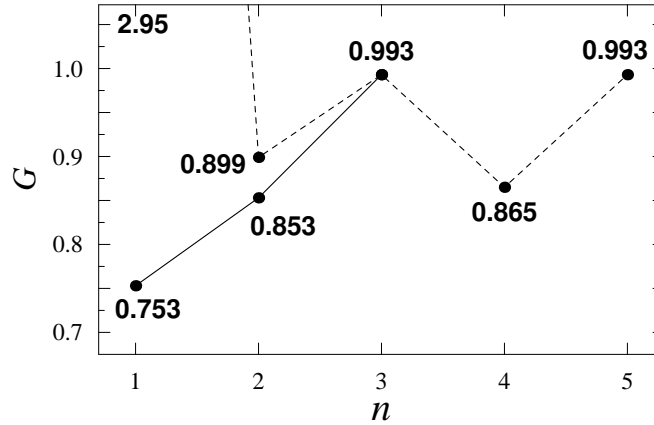
between the leads and the scattering region is smooth. There are no discontinuities in the potential in the boundary regions that could cause spurious reflections.

Fig. 3.10 shows the calculated conductance  $G(E_F)$  at the Fermi level as a function of the length  $n$  of the sodium atomic wire. The conductance is calculated using a grid spacing along  $x, y$  and  $z$  directions of  $h_{x,y,z} = 0.67 a_0$  (giving  $L = 6, W_y = W_z = 24$ ) and a FDA of order  $N = 4$ .<sup>4</sup> The  $2 \times 2$  lateral Brillouin zone is sampled by a  $12 \times 12$  uniform  $\mathbf{k}_{\parallel}$ -point grid. With these parameters the calculated conductances have converged to well within  $10^{-3} G_0$  (where  $G_0 = e^2/(\pi\hbar)$ ). We have aimed at a high accuracy here, but coarser grids can give acceptable results. A spacing  $h_{x,y,z} = 0.80$ , which gives  $N_{rs} = L \cdot W_y \cdot W_z = 5 \cdot 20 \cdot 20$  grid points per cell, combined with a  $6 \times 6$   $\mathbf{k}_{\parallel}$ -point sampling gives a conductance that deviates less than  $2 \cdot 10^{-3}$  from the highly accurate results.

All wires have a conductance close to unity, except the one-atom ( $n = 1$ ) wire. The high conductance for the one-atom wire is foremost due to tunneling between the left and right leads through vacuum. The latter can be calculated by omitting the wire and otherwise keeping the geometry fixed. Tunneling through vacuum leads to a conductance of  $2.20 G_0$  per  $2 \times 2$  surface cell. Vacuum tunneling decreases fast with the distance between left and right lead surfaces. At a distance corresponding to the two-atom wire it gives a conductance of  $0.047 G_0$ ; at distances corresponding to longer wires this conductance is negligible. Subtracting these vacuum tunneling values gives the lower curve in Fig. 3.10.

With the exception of the one-atomic wire, the conductances are close to unity.

<sup>4</sup>The number of cells  $S$  required for the scattering region of a  $n$ -atomic wire is approximately  $n_L + n_R + n$ , where  $n_L, n_R$  is the number of unit cells that define the surface regions of left and right electrodes. The number of grid points per cell is  $N_{rs} = L \cdot W_y \cdot W_z = 3456$ .



**Figure 3.10** : Top curve: conductance  $G(E_F)$  at the Fermi level (in units of  $e^2/\pi\hbar$ ) of a sodium atomic wire as a function of the number of atoms  $n$  in the wire. Bottom curve: conductance of a sodium atomic wire relative to vacuum tunneling conductance between two electrodes without wire.

This is perhaps not surprising, since within a tight-binding model atomic wires consisting of a monovalent atom like sodium are expected to have one open channel. For perfectly transmitting contacts this would give a conductance of  $1 G_0$  [160]. Our calculated conductances for  $n > 1$  are less than 15% smaller than this value, demonstrating that this transmission is indeed very high. The conductance of the one-atomic wire, relative to the vacuum tunneling conductance at this distance, is significantly lower than unity. The electronic structure of a single atom between two electrodes is substantially distorted from the simple single open channel model [136, 137].

On a finer scale we find evidence of an even-odd oscillation in the conductance obtained in previous studies [136, 137, 161–164]. The conductance for wires with  $n$  even tends to be lower than for those with  $n$  odd. In simple tight-binding terms odd-numbered atomic wires have a non-bonding level that tends to line up with the Fermi level of the leads, which gives a high transmission. For an even-numbered atomic wire on the other hand the Fermi level tends to fall in the gap between the bonding and anti-bonding levels of the wire, resulting in a lower transmission [165]. The size of the even-odd oscillation in the conductance depends of course upon the nature of the contacts between the atomic wire and the leads. Good contacts broaden the levels of the atomic wire into wide resonances, which tends to suppress the even-odd oscillation. Our wires have good contacts, but the even-odd oscillation remains distinctly visible.

Somewhat surprisingly, the size of the even-odd oscillation is however quite sensitive to the accuracy of the sodium potential used as input for the transport calculations. Extracting this potential from a self-consistent ground state calculation

requires the ground state energy to be converged at the scale of  $10^{-6}$ - $10^{-7}$  Hartrees. A weaker convergence criterion of  $10^{-5}$  Hartrees yields a potential that can change the conductance by up to 5 % and can even suppress the even-odd oscillation almost completely.

### 3.4 Summary

We have formulated and implemented a new numerical technique for calculating electronic transport in quantum wires and tunnel junctions in the linear response regime, starting from Landauer's scattering formalism. It is based upon a real-space grid representation of the scattering problem. Dividing space into left and right ideal leads and a scattering region, the problem is solved by *wave function matching* (WFM). First all propagating and evanescent Bloch modes of the leads are calculated. Subsequently the states in the scattering region are forced to match to the Bloch modes of the leads. This directly leads to the transmission matrix, which contains the transmission probability amplitudes between all modes of the left and right leads, and to the conductance. The computing costs of this algorithm scale linearly with the size of the scattering region.

It is shown that the use of a high-order finite-difference approximation for the kinetic energy operator leads to a high accuracy and efficiency. This is demonstrated for a model potential by benchmarking the technique against analytical and numerically "exact" solutions. The method is then applied to calculate the conductance in sodium atomic wires, where the potential in the wire and in the bulk sodium leads is obtained from self-consistent DFT calculations.





## Chapter 4

# Electronic transport through sodium nanowires

We study the stability of conductance oscillations in monatomic sodium wires with respect to structural variations. The geometry, the electronic structure and the electronic potential of sodium wires suspended between two sodium electrodes are obtained from self-consistent density functional theory calculations. The conductance is calculated within the framework of the Landauer-Büttiker formalism, using the mode matching technique as formulated recently in a real-space finite-difference scheme [Phys. Rev. B **70**, 195402 (2004)]. We find a regular even-odd conductance oscillation as a function of the wire length, where wires comprising an odd number of atoms have a conductance close to the quantum unit  $G_0 = e^2/\pi\hbar$ , and even-numbered wires have a lower conductance. The conductance of odd-numbered wires is stable with respect to geometry changes in the wire or in the contacts between the wire and the electrodes; the conductance of even numbered wires is more sensitive. Geometry changes affect the spacing and widths of the wire resonances. In case of odd-numbered wires the transmission is on-resonance, and hardly affected by the resonance shapes, whereas for even-numbered wires the transmission is off-resonance and sensitive to the resonance shapes. Predicting amplitude of the conductance oscillation requires a first-principles calculation based upon a realistic structure of the wire and the leads. A simple tight-binding model is introduced to clarify these results.

### 4.1 Introduction

Recent progress in fabricating conductors of atomic dimensions has stimulated a large number of experimental and theoretical studies on these nanoscale devices [61]. Conductors whose cross section contains only a small number of atoms are commonly called “atomic wires”. Clear evidence that the fundamental limit of a one atom cross section can be reached, has been presented for gold atomic wires [166, 167]. Over the last decade the electronic transport in atomic wires made of various metals

has been characterized in great detail experimentally [82, 168–178]. Such wires have conductances of the order of the quantum unit  $G_0 = e^2/\pi\hbar$ , so the description of their transport properties, as well as of their atomic and electronic structures, requires a full quantum-mechanical treatment [62].

Simple theoretical schemes have been proposed, in which the atomic wire is described by a jellium [179, 180] or a tight-binding model [133]. At present a first-principles approach based on density functional theory (DFT) gives the most advanced description of the geometry and electronic structure of atomic wires. Several theoretical methods that combine the Landauer-Büttiker formalism with DFT, have been developed in order to solve the quantum transport problem in terms of scattering amplitudes [70, 108, 134, 136, 138, 139, 149, 181]. Alternatively, a Green's function formalism is commonly used for solving the transport problem [83, 84, 97–99, 141–144, 182–186]. Both these approaches are in fact completely equivalent in the case of noninteracting electrons [71].

Atomic wires that have a cross section of just one atom, so-called “monatomic” wires, are the ultimate examples of quasi one-dimensional systems. Here the effects of a reduced dimensionality are expected to be most pronounced. A priori the existence of monatomic wires is not obvious. Such free standing one-dimensional structures might be unstable because of the low coordination number of the atoms in the wire. Molecular dynamics simulations based upon an effective medium model [187] or a tight-binding model [188, 189] have been used to study the stability of a wire as a function of its elongation. Since such simulations use highly simplified interatomic potentials, they aim at providing a qualitative understanding of the wire formation. A more quantitative description can be provided by first principles DFT calculations [190–194], but then only relatively small systems can be handled. A multitude of different structures have been studied, such as dimerized, zigzag and helical wires [195–203].

One of the most striking features of monatomic wires is the non-monotonic behavior of the conductance as a function of the number of atoms in the wire. Such a behavior has been predicted by Lang for wires consisting of monovalent atoms [137]. His model assumes a chain of atoms suspended between two planar semi-infinite jellium electrodes. The conductance predicted by this model is much lower than the quantum unit, which disagrees with experiments on monovalent atomic chains [166, 168, 171]. However, the model can be modified in a simple way by adding a basis consisting of three atoms on top of the jellium electrodes [158]. This reduces the charge transfer between the wire and leads and it reduces spurious reflections at the wire-electrode interfaces. The conductance of a one-atom wire is then close to the quantum unit, in agreement with experiment.

From the Friedel sum rule it can be shown that the conductance of an atomic chain consisting of monovalent atoms exhibits a regular oscillation with respect to the number of atoms in the chain [161]. Moreover, assuming mirror reflection and time-reversal symmetries together with local charge neutrality of the wire, the conductance of wires with an odd number of atoms is expected to be very close to the quantum unit [204, 205]. The period of the conductance oscillation then equal to two atoms. This has been confirmed in conductance calculations for wires connected to jellium

leads via an atomic basis [163].

The oscillating behavior of the conductance as a function of the wire length has been observed experimentally in gold wires [82], and a small parity effect has recently been found in silver wires [206]. Oscillations have also been observed in wires consisting of atoms with a higher valency [166]. The oscillation period depends upon the valency; e.g., for monatomic aluminium wires calculations predict that the period of oscillation is equal to four atoms, which is determined by the filling factor of the valence band of the infinite wire [165]. The transport properties of very short ( $< 4$  atoms) aluminium wires depend on the details of the charge transfer between the wires and the leads.

Since the discovery of the parity effect in wires of monovalent atoms there has been a discussion on how sensitive the conductance oscillation is to the geometry of the wire and the contacts. The general arguments given in Ref. [161] suggest that the conductance for odd-numbered wires should always be higher than for even-numbered ones, provided that the wires are locally charge neutral. For a sodium wire connected to (artificial) fcc sodium electrodes the charge transfer has been estimated and it is found to be rather small [164]. Conductance calculations based upon a scattering approach have recently been performed for short sodium wires attached to sodium electrodes with a more realistic bcc structure [70,207]. The phase of the conductance oscillation obtained in these calculations, is consistent with that found in the jellium electrode calculations [161,163].

Other studies predict however that the conductance oscillation found in wires of monovalent atoms is very sensitive to the geometry. Even the phase of the oscillation can be reversed such that even-numbered wires have a larger conductance than odd-numbered ones [162,208–210]. Using the Friedel sum rule to calculate the conductance of a wire connected to jellium electrodes it has been found in Ref. [162] that the phase of the conductance oscillation is reversed if the jellium leads become sufficiently sharp. This has not been confirmed by later calculations using a scattering approach to calculate the conductance [184], which give results that are consistent with Lang's findings for planar jellium electrodes [137]. If an atomic basis is used to connect the wire and the jellium electrodes [184], then the conductance oscillation is similar to that observed in previous calculations, i.e. odd-numbered chains have a higher conductance than even-numbered ones.

From strictly one-dimensional LCAO-DFT calculations, i.e. sodium chains coupled to one-dimensional metallic leads, it has been argued that there is a critical distance between the wire and the leads where the conductance oscillation changes its phase and even numbered chains become more conductive than odd-numbered ones [208]. A change of phase has also been predicted to occur upon elongating the wire by adding atoms. In short wires the odd-numbered chains then have the higher conductance and in long wires the even-numbered ones have the higher conductance. A similar effect has been also claimed recently for particular atomic configurations in calculations using three-dimensional leads [210]. A similar change of phase has been also found in Ref. [209], but the authors note that the three-dimensional tight-binding approach used in their calculations most likely does not describe this subtle parity effect.

In conclusion, some of the results that appeared in the literature regarding the even-odd conductance oscillation in monatomic wires seem to be contradictory. In this Chapter we present the results of conductance calculations for monatomic sodium wires in order to investigate the effect of the wire geometry and the wire-lead coupling on the conductance oscillation. Since sodium has a simple electronic structure, a sodium wire is one of the simplest examples of a atomic chain. As such it is an important reference system for studying wires with a more complicated electronic structure, and it can be used as a system for benchmarking theoretical and computational techniques. We perform first-principles conductance calculations based on the mode-matching technique [70] on sodium wires spanned between sodium electrodes, while varying the atomic configuration of the wire and that of the wire-lead contacts. The entire system consisting of the wire and the semi-infinite electrodes, is treated fully atomistically.

We find that the parity effect, i.e. the even-odd conductance oscillation, is very robust with respect to changing the structure of the wire and to varying the strength of the coupling between the wire and the leads. We study the conductance of long wires, and find no tendency to a phase change in the even-odd oscillation. The conductance is analyzed using the electronic levels of free-standing wires in order to interpret the parity effect in terms of transmission resonances. In addition, we analyze our first-principles results using a simple tight-binding model. In particular we show that local charge neutrality of the sodium wires provides a strong constraint on the phase of the conductance oscillation for all atomic structures considered. In the absence of a significant charge transfer between the wire and the leads, a transmission resonance is pinned at the Fermi energy for wires containing an odd number of atoms which leads to a conductance close to one quantum unit. Obtaining quantitative values for the conductance, particularly for even-numbered wires, requires well-converged first-principles calculations using a realistic structure of the wire and the leads.

The structure of this Chapter is as follows. In Sec. 4.2 we discuss the geometry of infinite and finite sodium wires. The even-odd oscillation of the conductance is discussed in general terms in Sec. 4.3. We investigate the effects on the conductance of varying the wire geometry and the contacts between wire and leads in Sec. 4.4. Current-voltage characteristics are analyzed in Sec. 4.5. In Sec. 4.6 we compare our results to those obtained in previous studies. A summary and conclusions are presented in the last section. The important technical details of  $\mathbf{k}$ -point sampling is discussed in Appendix C.1.

## 4.2 Structure of sodium wires

In this section we investigate possible structures of sodium monatomic wires by DFT total energy calculations in combination with geometry optimizations. DFT total energies are calculated with the PW91 generalized gradient approximation (GGA) functional [29] and the projector augmented wave (PAW) method [48, 49], as implemented in the Vienna *Ab initio* Simulation Package (VASP) [211–213]. We use a

Table 4.1: Na-Na nearest neighbor bond length (in  $a_0$ ) for sodium wires, bulk sodium and the sodium dimer compared to all-electron calculations and to experiment. For the zigzag chain also the bond angle is given.

	this work	all electron	experiment
linear	6.30	-	-
zigzag	6.85 (57°)	-	-
bulk	6.88	6.90 (Ref. [214])	6.91 (Ref. [215])
dimer	5.88	5.85 (Ref. [216])	5.82 (Ref. [217])

standard frozen core PAW potential and a plane wave basis set with a kinetic energy cutoff of 24 Ry. A Methfessel-Paxton smearing is applied in integrations over the Brillouin zone with a smearing parameter  $\sigma = 0.1$  eV. First we discuss the structure of the infinite wire, and then that of finite wires connected to bcc sodium electrodes.

### 4.2.1 Infinite wires

We use an orthorhombic supercell with cell parameters perpendicular to the wire direction of 17 Å. Parallel to the wire the cell parameter is optimized using 24  $\mathbf{k}$ -points to sample the Brillouin zone along the wire direction for a cell containing two atoms.

First we consider a linear wire; its optimized Na-Na bond length is given in Table 4.1. We have checked that symmetry breaking, in the form of a Peierls distortion, is negligible for Na-Na bond lengths near the equilibrium interatomic distance. This agrees with calculations for other monatomic wires [198,199]. Only for sodium wires that are stretched to interatomic distances  $\gtrsim 6.91a_0$  does a Peierls distortion take place, accompanied by a metal-insulator transition. In order to test the accuracy of the calculations we have also calculated the optimized Na-Na bond length in bulk sodium and in the sodium dimer. The accuracy is found to be better than 1% as compared to the experimental values, see Table 4.1.

One-dimensional chains are often unstable with respect to a deformation in the transverse direction, which results in a zigzag structure. Only if the interatomic distance exceeds a critical value, is a linear configuration preferred [198]. Indeed we find that a sodium wire with a zigzag structure has a lower energy; its geometry is presented in Table 4.1. It is in reasonable agreement with the one obtained in a previous DFT-LDA calculation [218]. A bond angle of  $\sim 60^\circ$  is typically found also in other monatomic wires [203]. Upon stretching the wire a transformation from a zigzag to a linear geometry takes place as soon as the interatomic atomic distance in the linear wire becomes  $\gtrsim 6.5a_0$ . In Ref. [198] a zigzag structure was found in gold and copper wires, whereas in potassium and calcium wires it existed only under compression. The stability of the zigzag geometry has therefore been related to the presence of directional  $d$ -bonds in gold and copper. However, our finding that a sodium wire behaves similarly, suggests that the occurrence of a zigzag geometry is

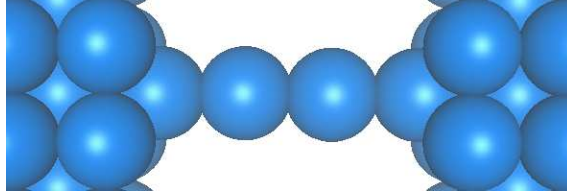


**Figure 4.1** : Supercell representing a 2 atom sodium wire between two sodium leads terminated by (001) surfaces. The wire is connected to electrodes via an apex atom placed on top of each electrode in a hollow site.

not a result of  $d$ -bonds only.

Whereas the lowest energy structure is paramagnetic, in Ref. [218] two additional local minima have been found corresponding to ferromagnetic structures with magnetic moments  $\sim 0.02 \mu_B$  and  $0.12 \mu_B$ , respectively. Our lowest energy (zigzag and linear) structures are always paramagnetic. A magnetic ordering occurs for zigzag structures when the Fermi level crosses two energy bands instead of just one band, but the magnetism disappears rapidly as soon as the wire is stretched sufficiently. Small magnetic moments have also been found in calculations on gold wires [218,219]. No trace of magnetic effects has been observed in recent conductance measurements, which were performed both in weak and in strong magnetic fields [220]. Since both experiment and theory favor non-magnetic structures, we will only consider non-magnetic sodium wires in the following.

#### 4.2.2 Finite wires

In this section we discuss the structure of a finite monatomic sodium wire suspended between two electrodes. A reasonable approach is to study the structure of the wire near its equilibrium geometry, which corresponds to the most stable chemical bonding. We use the equilibrium geometry of the infinite linear wire as a starting point for finite wires. The electrodes consist of bulk Na in the (001) orientation. To calculate the structure we use a periodic supercell that consists of a slab of 5 layers of sodium for the electrodes. On top of each electrode surface an apex atom is placed in a hollow site and a linear wire bridges the two apex atoms as shown in Fig. 4.1. We use a  $12 \times 12 \times 4$   $\mathbf{k}$ -point sampling of the supercell. During the geometry optimization the atoms in the wire, the apex atoms and the atoms in the top surface layer are allowed to relax.

The results of the geometry optimization for wires of different lengths are given in Table 4.2. We will discuss the most prominent features of the wire geometries starting from the electrodes. All structures have mirror symmetry with respect to a plane through the center of the wire, parallel to the electrode surface. We emphasize that this symmetry is not imposed upon the system, but is the result of the geometry optimization. The top layer of the electrode relaxes slightly outwards; the distance

Table 4.2: Optimized bond lengths (in  $a_0$ ) for a Na wire suspended between Na electrodes. The columns indicate the number of atoms in a wire. The row labels  $i$ - $j$  indicate the distance between the  $i$ 'th and  $j$ 'th atom in a wire;  $\bar{d}$  is the average bond length. A-1 indicates the distance between the apex atom and the wire, L1-A the distance between the apex atom and the surface layer, and L1-L2 the distance between the two top layers of the electrode. The in-plane Na-Na bond length in the top layer is given in the bottom row.

bonds	1	2	3	4	5	6	7	8	9
1-2		6.35	6.45	6.34	6.41	6.34	6.41	6.33	6.37
2-3			6.45	6.46	6.45	6.45	6.43	6.44	6.44
3-4				6.34	6.45	6.36	6.41	6.37	6.40
4-5					6.41	6.45	6.41	6.45	6.42
5-6						6.34	6.43	6.37	6.42
6-7							6.41	6.44	6.40
7-8								6.33	6.44
8-9									6.37
$\bar{d}$	-	6.35	6.45	6.38	6.43	6.39	6.42	6.39	6.41
A-1	6.53	6.59	6.51	6.54	6.49	6.51	6.47	6.48	6.46
L1-A	3.72	3.64	3.60	3.58	3.52	3.52	3.45	3.43	3.38
L2-L1	4.03	4.03	4.02	4.03	4.02	4.03	4.02	4.06	4.02
in-plane	8.17	8.19	8.20	8.23	8.23	8.25	8.26	8.26	8.31

between the top two layers, L1-L2 $\sim 4.03a_0$ , is somewhat larger than the bulk value  $3.99a_0$ . The distance between the apex atom and the surface L1-A decreases with the length of the wire, which indicates a growing bond strength. The distance between the apex atom and the first atom of the wire A-1 is always larger than the maximum bond length between atoms in the wire. This indicates that bonding within the wire is stronger than bonding to the electrodes. For gold wires the opposite has been found, i.e. the A-1 distance is shorter than the average bond length [192].

Focusing upon the interatomic distances between atoms in the wire, Table 4.2 clearly shows that even-numbered wires exhibit dimerization, i.e. an alternation between short and long bonds. A similar tendency is found in odd-numbered chains, but they have a topological defect, i.e. a "kink", in the center of the wire. The average bond length in even as well as odd-numbered wires of  $\sim 6.40a_0$  is larger than the optimized bond length of  $6.30a_0$  in the infinite wire. The infinite chain does not show a dimerization until the average bond length is larger than  $\sim 6.91a_0$  (see the previous section). This strongly suggests that dimerization in finite chains is enforced by its boundaries. A qualitatively similar behavior has also been found in finite gold wires [192].

Since dimerization of a finite wire is associated with its bonding to the electrodes, one needs to check how sensitive the dimerization pattern is to the connection between wire and electrode. We have performed calculations on larger lateral supercells, and

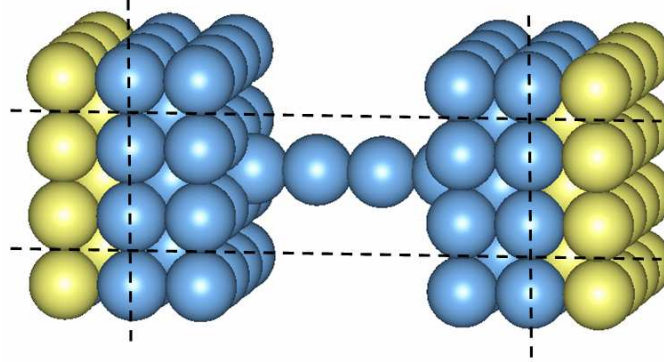


**Figure 4.2** : Structure of an atomic wire consisting of 2 sodium atoms between two sodium leads terminated by (001) surfaces. The boundaries of the supercell is indicated by dashed lines. Bulk atoms are indicated by yellow (light grey) balls and atoms in the scattering region by blue (dark grey) balls, respectively.

have also made the connection more gradual by putting a base of four atoms between the electrode surface and the apex atom. These structural variations give essentially the same bonding pattern in the wires, i.e. even-numbered wires are dimerized, and odd-numbered wires additionally have a kink in the center. The distance  $A-1$  between apex atom and wire stays larger than the interatomic distances in the wire. These distances can be modified by stretching or compressing the wire, but the dimerization pattern is robust. In conclusion, the optimized wire structures presented in Table 4.2 can be considered as typical structures that are formed by sodium finite chains suspended between two semi-infinite electrodes.

### 4.3 Conductance oscillation

Our calculations of the conductance are based on the mode-matching technique and use a real-space finite-difference representation of the Kohn-Sham Hamiltonian and the wave functions [70]. As a first step, the one-electron self-consistent potentials of the bulk leads and the scattering region containing the wire are obtained from DFT calculations. Subsequently the scattering problem is solved at the Fermi energy by matching the modes in the leads to the wave function in the scattering region. The conductance  $G$  can be expressed in terms of normalized transmission amplitudes  $t_{n,n'}$  using the Landauer-Büttiker formula [67]

$$G = G_0 \sum_{n,n'} |t_{n,n'}|^2, \quad (4.1)$$

where  $n$  and  $n'$  label the right-going modes in the left and right leads, respectively and  $G_0 = e^2/\pi\hbar$ . An efficient implementation of a high-order finite-difference scheme



for solving the scattering problem is discussed in Ref. [70].

More specifically, the one-electron potentials of the leads and the scattering regions are extracted from two DFT calculations for bulk bcc sodium and for the supercell shown in Fig. 4.2, respectively. For these calculations we use a local Troullier-Martins pseudopotential [45] with a core radius  $r_c = 2.95 a_0$ ; only the  $3s$  electrons of sodium are treated as valence electrons. All plane waves are included up to a kinetic energy cutoff of 16 Ry. We use  $32 \times 32 \times 32$   $\mathbf{k}$ -points to sample the Brillouin zone (BZ) of the cubic unit cell of bulk bcc sodium. In our supercell calculations,  $8^2$   $\mathbf{k}$ -points are used to sample the BZ in the case of a  $2 \times 2$  supercell, and  $6^2$   $\mathbf{k}$ -points in the case of a  $3 \times 3$  supercell. In all cases a Methfessel-Paxton smearing with  $\sigma = 0.1$  eV is applied. Total energies are converged to within  $5 \cdot 10^{-7}$  Hartrees.

One assumes that the leads outside the scattering region are perfectly crystalline bulk material. At the edges of the scattering region, the potential should join smoothly to the potentials of the bulk leads. We have checked that this is the case. Enlarging the scattering region by including two extra atomic layers into each lead changes the results reported for the conductance only by  $\sim 1.5\%$  for even-numbered wires and  $\lesssim 0.5\%$  for odd-numbered wires. The Fermi energy is extracted from the bulk calculation. The only parameters in calculating the conductance within the mode-matching finite-difference scheme are the order  $N$  of the finite-difference approximation of the kinetic energy (i.e., the second derivative) and the spacing  $h_{x,y,z}$  between the real-space grid points. We use  $N = 4$  and  $h_{x,y,z} = 0.80a_0$ ; for details and convergence tests we refer to Ref. [70]. The total transmission is averaged over the  $\mathbf{k}_{\parallel}$ -point grid of the lateral BZ of the supercell. To calculate the transmission it is important to apply a proper  $\mathbf{k}_{\parallel}$ -point sampling. This will be discussed in Appendix C.1. Most calculations are done for a  $2 \times 2$  lateral supercell. Enlarging the supercell changes the conductance only marginally as will be discussed in Sec. 4.4.2.

The electron transport in the crystalline leads is ballistic, i.e. an electron goes through the leads without any scattering. The transport properties of a monatomic wire suspended between two leads depend upon three factors; the number of atoms in the chain, the geometry of the wire, and the contact between wire and leads. In Sec. 4.4 we will discuss how these factors influence the conductance. In the present section we will analyze the conductance of monatomic sodium wires in a reference geometry, where all Na-Na bond lengths are chosen to be equal to the bulk value  $6.91a_0$ , see Table 4.1. As in the previous section we attach a finite atomic wire to the leads via two apex atoms, which then have a coordination number 5. All atoms in the wire have a coordination number 2.

### 4.3.1 First-principles calculations

The calculated conductance as a function of the number of atoms in the atomic chain is given in Fig. 4.3. Since a sodium atom has valence one, both the infinite sodium chain and bulk sodium have a half-filled band, and the infinite wire has one conducting channel at the Fermi level.<sup>1</sup> The conductance of the infinite chain is then

<sup>1</sup>The Fermi level can cross two energy bands for a strongly deformed chain with zigzag structure. In that case the chain has two conducting channels.

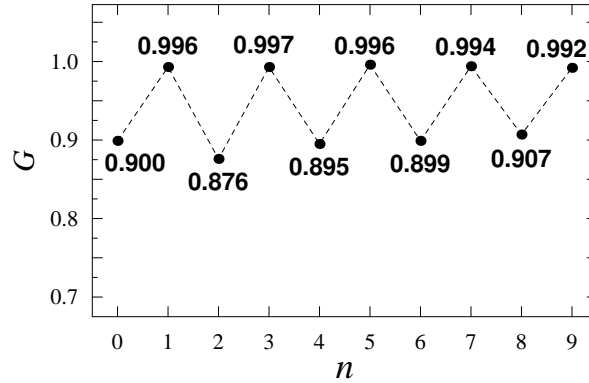


**Figure 4.3** : Conductance (in units of  $G_0$ ) as a function of the number of atoms in the atomic chain. All atomic bond lengths in the system are equal to the bulk value  $d = 6.91$  (a.u.).

equal to the quantum unit  $G_0$ , and the conductance of finite wires is  $\leq G_0$ . As can be observed in Fig. 4.3 the conductance exhibits a regular oscillation as a function of the number of atoms in the wire. The conductance is very close to  $G_0$  for odd-numbered wires, and for even-numbered wires it is  $\sim 10\%$  lower. Such a behavior of the conductance in atomic-sized conductors is very different from ohmic behavior in macroscopic conductors; it expresses the quantum nature of the electron transport at the nanoscale.

In order to interpret the even-odd oscillation we have calculated the conductance as a function of energy for wires of different length. The results for monatomic wires consisting of four and five atoms are shown in Fig. 4.4. Resonant peaks in the conductance can be clearly identified. Qualitatively they correspond to energy levels of a free-standing Na wire, which are shifted and broadened into resonances by the interaction of the wire with the leads. To illustrate this, the calculated energy levels of free-standing wires of four and five atoms are shown as bars in Fig. 4.4. The levels are sufficiently close to the resonant energies to warrant an interpretation of the conductance in terms of a transmission through levels of the wire. As is clearly observed in Fig. 4.4, the Fermi level is in between two resonant peaks for a four atom wire and right on top of a resonance for a five atom wire. By calculating the conductance as a function of energy for wires of different length it can be shown that this observation can be generalized. The Fermi level is between resonances for even-numbered wires and on top of a resonance for odd-numbered wires.

An intuitive picture of the transmission through the energy levels is then presented by Fig. 4.5. Odd-numbered wires have a highest occupied molecular orbital (HOMO) that is half filled. Perfect transmission through this state takes place if the Fermi level aligns with the HOMO. In even-numbered wires the HOMO is completely filled

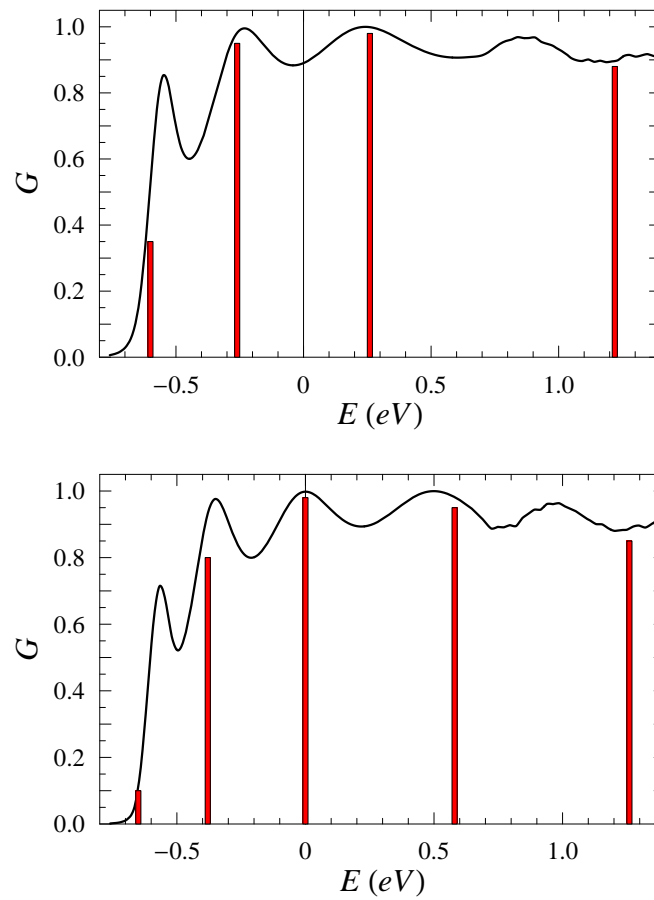


**Figure 4.4** : Conductance (in units of  $G_0$ ) as a function of energy for monatomic wires consisting of four (top figure) and five (bottom figure) atoms. The bars correspond to the energy levels of free-standing wires.  $E = 0$  corresponds to the Fermi level.

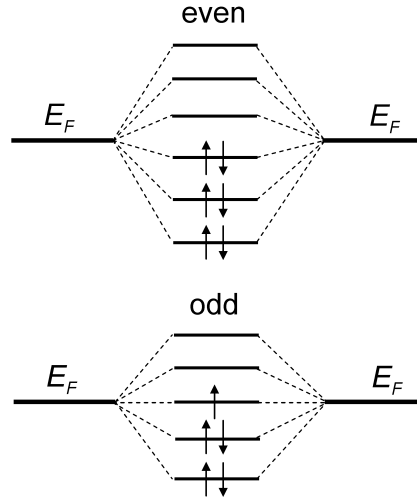


**Figure 4.5** : Energy levels for odd and even-numbered wires. The Fermi level is in the middle of the HOMO-LUMO gap for even-numbered wires, and it aligns with the HOMO level for odd-numbered wires.

and separated by a gap from the LUMO (lowest unoccupied molecular orbital) level. The Fermi level is then in the HOMO-LUMO gap. The position of the Fermi level with respect to the HOMO level leads to the off and on resonant behavior of the conductance as a function of the wire length, which gives rise to a regular even-odd oscillation of the conductance. In the next section we will study this intuitive model in somewhat more detail by means of a simple tight-binding model.

### 4.3.2 Tight-binding model

To support the intuitive picture presented in the previous section we use a simple tight-binding model as shown in Fig. 4.6, in which the leads are modeled as quasi one-dimensional systems described by effective parameters. Here  $\varepsilon_0$ ,  $\beta$  are the on-site energies and nearest neighbor hopping coefficients of the leads, and  $\varepsilon'_0$ ,  $\beta'$  are the corresponding parameters of the wire. The coupling between the left (right) electrode and the atomic chain is given by the hopping coefficient  $\beta_c$  ( $\beta'_c$ ).

If the system has mirror symmetry, the coupling is symmetric, i.e.  $\beta_c = \beta'_c$ . The leads and the chain are made of the same material (sodium). If one assumes that all atoms are neutral (local charge neutrality), then it is not unreasonable to set  $\varepsilon_0 = \varepsilon'_0$ . The conductance can be calculated analytically for this model by the mode matching technique [71]. The modes can be labeled by a wave number  $k$  in 1D Brillouin zone of the leads. The familiar relation  $E = \varepsilon_0 + 2\beta \cos(ka)$  gives for a half filled band the Fermi energy  $E_F = \varepsilon_0$  and the Fermi wavenumber  $k_F = \pi/2a$ . The parameter  $\beta$  can be used as a scaling parameter. In the following all energy parameters  $\varepsilon_0, \varepsilon'_0, \beta', \beta_c, \beta'_c$

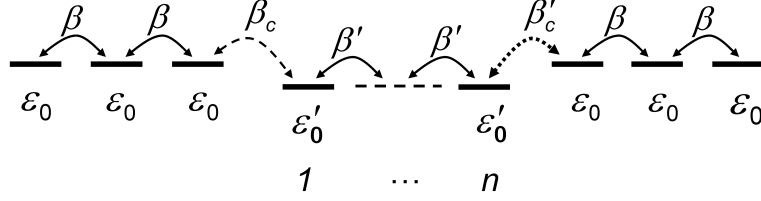


**Figure 4.6 :** Tight-binding representation of the  $n$ -atomic wire attached to two semi-infinite one-dimensional leads.

are in units of  $\beta$ . The conductance at the Fermi energy of a wire consisting of  $n$  atoms is given by

$$\begin{aligned} G &= G_0 && n \text{ odd;} \\ &= G_0 \frac{4\beta_c^4/\beta'^2}{[1 + \beta_c^4/\beta'^2]^2}; && n \text{ even.} \end{aligned} \quad (4.2)$$

The conductance for odd-numbered wires is equal to the quantum unit, and it is smaller than the quantum unit for even-numbered wires (unless  $\beta_c^2 = \beta'$ ). This corresponds to the situation shown in Fig. 4.5.

It is instructive to study some other consequences of the tight-binding model. If  $\Delta\varepsilon = \varepsilon_0 - \varepsilon'_0 \neq 0$  then a charge transfer will take place between the leads and the wire. The conductance calculated at the Fermi energy for a one-site wire ( $n = 1$ ) and a two-site wire ( $n = 2$ ) become, respectively,

$$G = G_0 \frac{4\beta_c^4}{\Delta\varepsilon^2 + 4\beta_c^4} \leq 1, \quad (4.3)$$

$$G = G_0 \frac{4\beta_c^4\beta'^2}{[\beta_c^4 + (\beta' + \Delta\varepsilon)^2][\beta_c^4 + (\beta' - \Delta\varepsilon)^2]}. \quad (4.4)$$

According to Eq. (4.3) a non-zero  $\Delta\varepsilon$  suppresses the transmission through a one-site wire. The transmission is shifted “off resonance” and the conductance becomes smaller than the quantum unit. However, the coupling between wire and lead also causes a broadening of the resonance, which is proportional to  $\beta_c$ . This broadening partially compensates for the decrease of the conductance. If the coupling is sufficiently strong, i.e.  $4\beta_c^4 \gg \Delta\varepsilon^2$ , then the conductance is again close to the quantum unit. In the limit of weak coupling, i.e.  $4\beta_c^4 \ll \Delta\varepsilon^2$ , the conductance goes to zero with decreasing  $\beta_c$  for any non-zero  $\Delta\varepsilon$ . The conductance as a function of  $\beta_c$  is shown in Fig. 4.7 for two different values of  $\Delta\varepsilon$ .

The conductance of a two-site wire, see Eq. (4.4), behaves qualitatively different as a function of the coupling strength  $\beta_c$ . In the weak coupling limit, i.e.  $\beta_c^4 \ll (\beta' \pm \Delta\varepsilon)^2$ , corresponding to  $\beta_c < 1$  in Fig. 4.7(a) and (b), the conductance goes to zero with decreasing  $\beta_c$  and the decrease is faster than for a one-site wire. Note

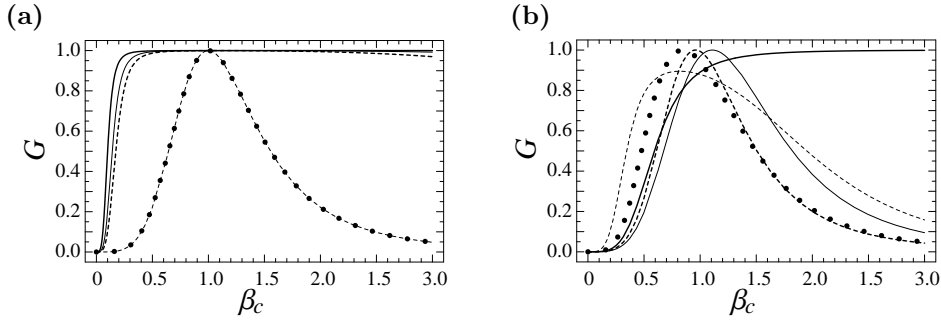


**Figure 4.7 :** (a) Conductance (in units of  $G_0$ ) at the Fermi energy as a function of  $\beta_c$  (in units of  $\beta$ ) for wires with  $n = 1$  (thick solid line), 2 (large dots), 3 (thin solid), 4 (dashed), and 5 (thick dashed) atoms;  $\Delta\varepsilon = 0.02$ ;  $\beta' = 1$ , (b) As figure (a) with  $\Delta\varepsilon = 0.7$ ;  $\beta' = 1$ .

that this only holds for  $\Delta\varepsilon \ll \beta'$ . If  $\Delta\varepsilon \sim \beta'$  then the conductance decreases more slowly with decreasing  $\beta_c$  for a two-site wire than for a one-site wire, see the range  $\beta_c < 1$  in Fig. 4.7(b). If the coupling between wire and lead is strong, i.e.  $\beta_c^4 \gg (\beta' \pm \Delta\varepsilon)^2$ , corresponding to  $\beta_c > 1$  in Figs. 4.7(a) and (b), then the conductance always decreases with increasing  $\beta_c$ . This is due to a phenomenon called “pair annihilation” of resonances [204], which happens if the resonance widths become larger than the spacing between the resonances. In a one-site wire this cannot happen, since there is only one resonance. Between the strong and weak coupling regimes there is a value of  $\beta_c$  (close to 1) where the conductance of a two-site wire is equal to the quantum unit, see Fig. 4.7.

The conductance of longer wires, i.e.  $n > 2$ , can be interpreted along the same lines. For small  $\Delta\varepsilon$ , the odd numbered wires resemble the one-site wire and the even-numbered wires resemble the two-site wire, as shown in Fig. 4.7. For a very large range of coupling strengths  $\beta_c$  one obtains an even-odd oscillation in the conductance of nearly constant amplitude. The conductance of odd-numbered chains is close to the quantum unit and that of even-numbered chains is smaller by an amount that depends upon the coupling between wire and lead. Apparently, this is the case that corresponds to the results of our first-principles calculations, see Fig. 4.3.

If  $\Delta\varepsilon$  becomes larger, the conductance of all wires as a function of  $\beta_c$  becomes qualitatively similar to that of the two-site wire, see Fig. 4.7(b). The amplitude and even the phase of the conductance oscillation as a function of the wire length then strongly depends upon the coupling  $\beta_c$  of the wire to the lead. For instance, if  $\beta_c \lesssim 0.7$  in Fig. 4.7(b), the conductance of even-numbered wires is higher than that of odd-numbered wires and all conductances are smaller than the quantum unit. Note that if  $\Delta\varepsilon$  is significant, it will be accompanied by a significant charge transfer between wire and leads. Whether this situation occurs can be studied by self-consistent first-principles calculations.

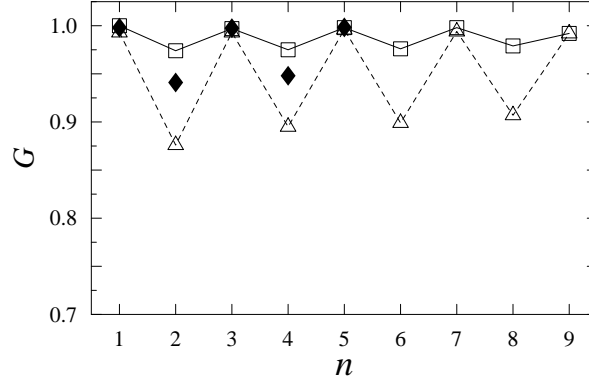


**Figure 4.8** : Conductance (in units of  $G_0$ ) as a function of the number of atoms in the wire. The triangles correspond to stretched wires with  $d = 6.91a_0$ , squares to compressed wires with  $d = 5.82a_0$ , and diamonds to the wires with  $d = 6.30a_0$ .

## 4.4 Stability of conductance oscillation

First-principles calculations on a reference geometry give a regular even-odd oscillation of the conductance as a function of the wire length, as discussed in the previous section. The odd-numbered wires have the highest conductance, close to the quantum unit  $G_0$ . The simplified tight-binding model suggests that the geometry might influence the amplitude and even the phase of the conductance oscillation. In Sec. 4.2 we have shown that monatomic sodium wires can have a linear, zigzag or dimerized geometry, depending upon the boundary conditions. In this section we study the influence of the wire geometry upon the conductance. In particular, we focus on the question whether the phase of the even-odd conductance oscillation is robust to modifications of the wire geometry.

### 4.4.1 Tension/compression of linear wires

We consider a uniform tension or compression of the wire. As in the previous section the Na-Na distance between atoms in the wire is kept at a uniform value  $d$  and the distance  $d_c$  between the apex atom and the wire is equal to  $d$ . As reference we use the results shown in Fig. 4.3 where  $d = 6.91a_0$ , which corresponds to the bond length in bulk sodium. If we take the equilibrium bond length  $d = 6.30a_0$  of the infinite linear wire as a characteristic bond length, then  $d = 6.91a_0$  corresponds to a wire under tension, i.e. a stretched wire. A wire with  $d = 5.82a_0$ , which corresponds to the equilibrium bond length of a  $\text{Na}_2$  molecule, is a wire under compression.

The results of first principles calculations of the conductance as a function of the wire length for  $d = 5.82, 6.30, 6.91a_0$  are presented in Fig. 4.8. In all cases the

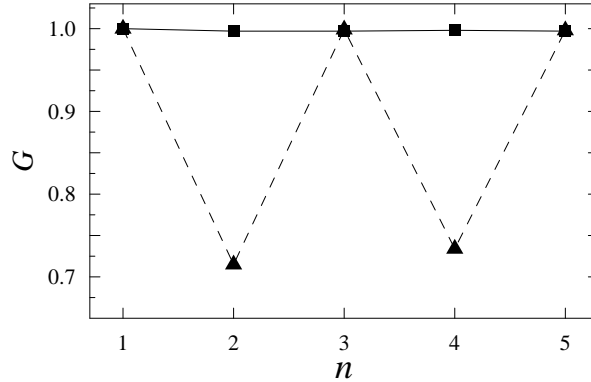


**Figure 4.9** : Conductance (in units of  $G_0$ ) as a function of the number of atoms in the wire. The triangles correspond to wires with  $d = 5.82a_0$  and  $d_c = 6.91_0$  and the squares to wires with  $d = 6.91a_0$  and  $d_c = 5.82a_0$ .

conductance exhibits a regular even-odd oscillation and the conductance of the odd-numbered wires is close to the quantum unit. The conduction of the even-numbered wires is smaller than the quantum unit and it depends only weakly on the number of atoms in the wire. According to the tight-binding analysis in Sec. 4.3.2, this suggests that the charge transfer between wire and lead, represented by  $\Delta\varepsilon$  in Eqs. (4.3) and (4.4) is very small, see Fig. 4.7.

The amplitude of the oscillation decreases with decreasing  $d$ . Two opposing effects influence the conductance if we decrease the interatomic spacing  $d$  in the wire. Firstly, the spacing between the resonant levels increases. In tight-binding terms the parameter  $\beta'$  increases, which tends to decrease the conductance of even-numbered wires, see Eq. (4.2). Secondly, since  $d_c = d$ , the resonances become broader if we decrease the distance between the wire and the lead. Again in tight-binding terms the parameter  $\beta_c$  increases, which tends to increase the conductance of even-numbered wires, cf. Eq. (4.2).<sup>2</sup> According to Fig. 4.8 the effect of the resonance broadening upon the conductance is larger than the effect of increased resonance spacing.

One can strengthen this analysis by varying the interatomic distance  $d$  in the wire, and the distance  $d_c$  between the apex atom and the wire independently. Fig. 4.9 shows the calculated conductance for a wire with  $d < d_c$ , i.e.  $d = 5.82a_0$  and  $d_c = 6.91_0$ . The conductance oscillations are quite large, which can be attributed to the increased resonance spacing discussed in the previous paragraph. A small  $d$  results in a large spacing between the resonant levels of the wire. Therefore, the

<sup>2</sup>This conclusion is based on an additional assumption that resonances around the Fermi level are not annihilated by a strong coupling between the wire and the leads. Otherwise, the conductance for even-numbered wires decreases if we increase the coupling parameter  $\beta_c$  (resonance widths) by decreasing the distance between the wire and the lead.



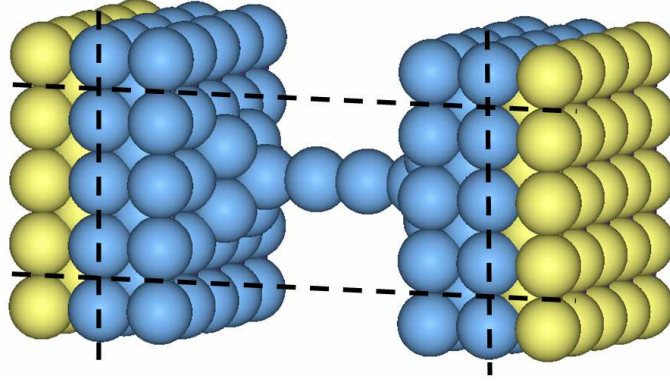


**Figure 4.10** : Structure of an atomic wire consisting of 2 sodium atoms between two sodium leads terminated by (001) surfaces. The atomic wire is connected to each surface via a five atom pyramid. The boundaries of the  $3 \times 3$  supercell are indicated by dashed lines. Bulk atoms are indicated by yellow (light grey) balls and atoms in the scattering region by blue (dark grey) balls, respectively.

transmission of even numbered wires, which is off resonance at the Fermi level, is low, whereas the transmission of odd-numbered wires stays on resonance and is high.

If we calculate the conductance for a wire with  $d > d_c$ , i.e.  $d = 6.91a_0$  and  $d_c = 5.82a_0$ , we see in Fig. 4.9 that the conductance oscillation is strongly suppressed. It can be attributed to the resonance broadening. If the coupling between the wire and the lead is strong, the resonances of the wire are wide. The transmission in even-numbered wires is then relatively high, whereas the transmission in odd-numbered wires stays close to the quantum unit. Fig. 4.9 shows that in case of a strong coupling between wire and lead the amplitude of the even-odd oscillation in the conductance can become very small. According to the tight-binding model, Eq. (4.2), this happens if  $\beta_c^4/\beta'^2 \approx 1$ . Note that such a strong coupling is less likely for sodium monatomic wires with optimized geometries, because the results discussed in Sec. 4.2 indicate that  $d < d_c$ . According to Ref. [192]  $d > d_c$  in gold monatomic chains, which might explain the small amplitude of the conductance oscillation found experimentally in gold wires [82].

In conclusion, stretching or compressing the wire changes the amplitude of the conductance oscillation, but it preserves its phase and conserves the close to unit value of the conductance for odd numbered wires.

#### 4.4.2 Contact geometry

The coupling between the wire and the leads could be influenced by the detailed geometry of the two contacts between the wire and the leads [161]. Since the geometries of the wire-lead contacts are not known from experiment, it makes sense to

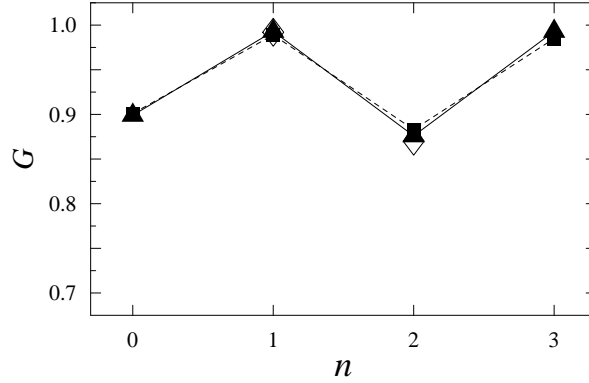


**Figure 4.11** : Conductance (in units of  $G_0$ ) as a function of the number of atoms in the atomic wire. Squares refer to the  $3 \times 3$  supercell with five atom pyramid contacts, diamonds to the  $3 \times 3$  supercell with one apex atom contacts, and triangles to the  $2 \times 2$  supercell one apex atom contacts.

study the sensitivity of the calculated conductances to these geometries. So far in our calculations we have modeled both contacts by one apex atom placed in a hollow site on the (001) surface in a  $2 \times 2$  lateral supercell. A more “gradual” contact is formed by a five atom pyramid placed on (001) surface, as is shown in Fig. 4.10. This requires using (at least) a  $3 \times 3$  supercell. To check that the size of the supercell does not influence the results, we have also done calculations for a  $3 \times 3$  supercell with one apex atom contacts. The calculated conductances are shown in Fig. 4.11. The conductance of monatomic sodium wires seems to be relatively insensitive to the contact geometry. At the same time it shows that the results obtained with the  $2 \times 2$  supercell are converged.

Another way of modifying the contacts is to remove the apex atoms and position the first and the last atom of the wire on top of an atom in the (001) surface layer. The calculated conductances are shown in Figs. 4.12(a) and (b) for the interatomic distances  $d = d_c = 6.91a_0$  and  $d = d_c = 5.82a_0$ , respectively. The results obtained with these “direct” wire-surface contacts look very similar to the ones obtained with one apex atom contacts, see Fig. 4.8. The amplitude of the even-odd oscillation is somewhat smaller for the “direct” coupling. According to the analysis presented in Sec. 4.4.1 this indicates a stronger coupling between wire and leads, or in tight-binding terms, a larger  $\beta_c$ , cf. Eq. 4.2. Note that the conductance of one-atom wires in Fig. 4.12 is higher than  $G_0$  due to direct tunneling between the electrodes.

One can also break the symmetry and use a direct contact between the wire and one of the leads, and a one apex atom contact between the wire and the other lead. The calculated conductances are again given in Fig. 4.12. A comparison with symmetric direct contacts and symmetric one apex atom contacts, see Fig. 4.8, shows

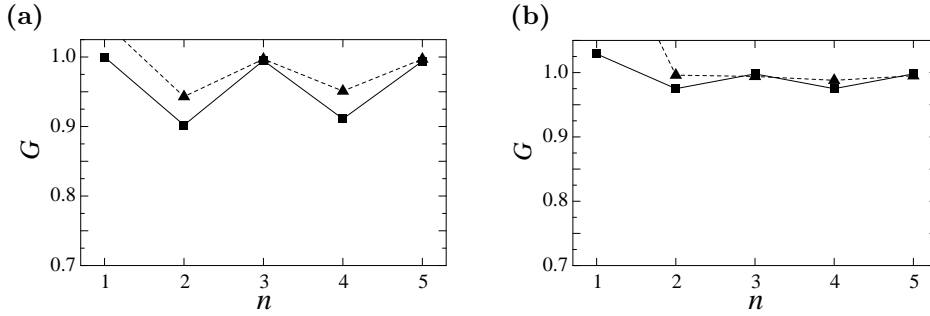


**Figure 4.12** : (a) Conductance (in units of  $G_0$ ) as a function of the number of atoms in the atomic wire with interatomic distance  $d = d_c = 6.91a_0$ . The triangles (dashed line) correspond to “direct” contacts between wire and leads. The squares (solid line) correspond to a direct contact at one end of the wire and a one apex atom contact at the other end, (b) As figure (a) with  $d = d_c = 5.82a_0$ .

that the phase of the even-odd conductance oscillation is the same and the amplitude is in between that of the two symmetric cases. It means that, besides the already mentioned stronger coupling between wire and lead for the “direct” contact, this symmetry breaking has little effect on the conductance.

We conclude that varying the geometries of the contacts between wire and leads does not have a large effect on the regular even-odd oscillation of the conductance.

#### 4.4.3 Wire geometry: zigzag wires and dimerization

In Sec. 4.2 we studied the geometry of infinite zigzag chains. In principle, a structural zigzag deformation could modify the conductance of a finite monatomic wire [161, 221]. Fig. 4.13 shows the calculated conductance of a wire with one apex atom contacts and bond lengths  $d = d_c = 6.91a_0$  to which a zigzag distortion pattern is applied with an amplitude corresponding to 15% of the bond length. Here the conductance calculations for zigzag and linear wires have been performed for the scattering region in Fig. 4.2 enlarged by adding 2 layers of sodium to each lead. Compared to straight wires, the conductance of zigzag even-numbered wires changes by  $\lesssim 3\%$ , whereas the conductance of odd-numbered wires is hardly affected at all. Such small effects are in line with results reported previously [161, 221].

According to the results obtained in Sec. 4.2 finite straight wires with equidistant atoms can spontaneously break their symmetry by dimerization. The conductance of optimized broken symmetry structures is discussed in the next section. Here we study the influence of an excessive symmetry breaking. We apply a regular dimerization pattern to the wire, which consists of an alternation between long and short bonds with bond lengths  $d = 6.91a_0$  and  $d = 5.82a_0$ , respectively. Continuing this pattern into the contacts this means that even-numbered wires have short  $d_c = 5.82a_0$  contact

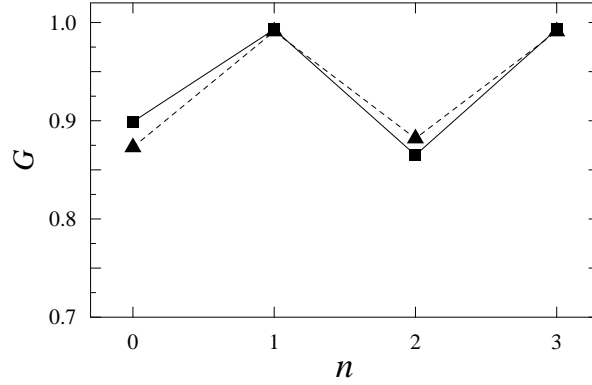


**Figure 4.13** : Conductance (in units of  $G_0$ ) as a function of the number of atoms in the atomic wire. Dashed line and filled rectangles correspond to zigzag wires; straight line and filled squares to linear wires with  $d = 6.91$  (a.u.).

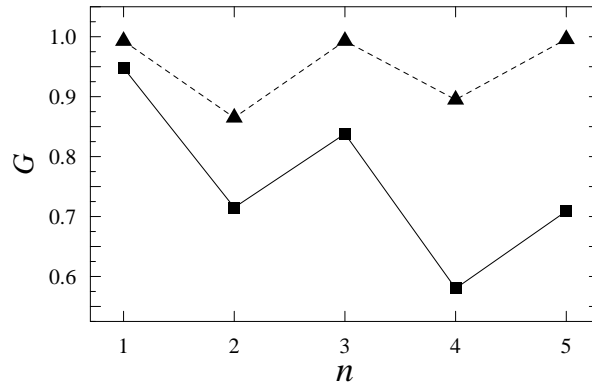


**Figure 4.14** : Conductance (in units of  $G_0$ ) as a function of the number of atoms in the atomic wire. The squares correspond to dimerized wires with alternating bond lengths of  $6.91a_0$  and  $5.82a_0$ ; as a reference, the triangles correspond to wires with a uniform bond length  $6.91a_0$ .

to both leads, whereas odd-numbered wires have one short  $d_c = 5.82a_0$  contact and one long  $d_c = 6.91a_0$  contact. The results are shown in Fig. 4.14.

This curve can be analyzed using the tight-binding model introduced in Sec. 4.3.2. Assuming charge neutrality, i.e.  $\Delta\varepsilon = 0$ , we need to generalize Eq. 4.2 to the case where the coupling  $\beta_c$  to the left and  $\beta'_c$  to the right leads are different. In addition,

dimerization in the wire leads to an alternation of two hopping coefficients  $\beta'$  and  $\beta''$ . The conductance of an  $n$ -atomic wire is then given by

$$\begin{aligned}
 G &= G_0 \frac{4 \left(\frac{\beta_c}{\beta'_c}\right)^2 \left(\frac{\beta''}{\beta'}\right)^{n-1}}{\left[1 + \left(\frac{\beta_c}{\beta'_c}\right)^2 \left(\frac{\beta''}{\beta'}\right)^{n-1}\right]^2} & n \text{ odd;} \\
 &= G_0 \frac{4 \left(\frac{\beta_c \beta'_c}{\beta'}\right)^2 \left(\frac{\beta''}{\beta'}\right)^{n-2}}{\left[1 + \left(\frac{\beta_c \beta'_c}{\beta'}\right)^2 \left(\frac{\beta''}{\beta'}\right)^{n-2}\right]^2} & n \text{ even.}
 \end{aligned} \tag{4.5}$$

One notes from Eq. 4.5 that even the shortest odd numbered wire,  $n = 1$  has a conductance smaller than the quantum unit if  $\beta_c \neq \beta'_c$ . This is observed in our first principles results, where the conductance of the  $n = 1$  wire is  $0.95G_0$ , see Fig. 4.14. Furthermore, Eq. 4.5 show that the conductance of both even-numbered and odd-numbered wires decreases as a function of increasing  $n$  if  $\beta' \neq \beta''$ . Also this is clearly observed in our first principles calculations. Dimerization of an infinite wire creates a gap in the density of states, so in general one expects that the conductance drops as a function of the wire length. For instance, a decreasing conductance for longer wires has been observed experientially for platinum, but its nature has not been clarified yet [82].

Finally, although the conductance for even and odd-numbered wires decreases as a function of wire length, its even-odd oscillation is preserved. Assuming  $\beta''/\beta' = \beta_c/\beta'_c = x$  for odd-numbered wires and  $\beta''/\beta' = \beta_c/\beta = \beta'_c/\beta' = y$  for even-numbered wires the conductances of the tight-binding model, Eq. 4.5, can be fitted to the first-principles results. This yields the parameter ratio's  $x \approx 0.81$  and  $y \approx 0.76$  for the odd and even numbered dimerized wires presented in Fig. 4.14.

#### 4.4.4 Optimized geometry

In previous sections we studied the influence of the structure of a monatomic wire upon its conductance by varying interatomic distances corresponding to values ranging from the Na dimer  $5.82a_0$  to the Na bulk  $6.91a_0$  values. In this section we discuss the conductance for wires with optimized geometries, which were obtained in Sec. 4.2. Fig. 4.15 shows the results from the first-principles calculations. As a reference, it also shows the results for wires with equidistant atoms corresponding to the geometry of an infinite wire.

It can be observed that the amplitude of the conductance oscillation is for wires with optimized geometry is larger than for the reference wires. This results from a slight decoupling of the wire from electrodes, since for the optimized wires  $d_c > \bar{d}$ , see Table 4.2 and the discussion in Sec. 4.4.2. As can be seen from Fig. 4.15, the phase of the even-odd conductance oscillation is also observed for optimized geometries. Moreover, despite the presence of a topological defect in the center of the odd-numbered wires, the conductance of odd-numbered wires is close to the

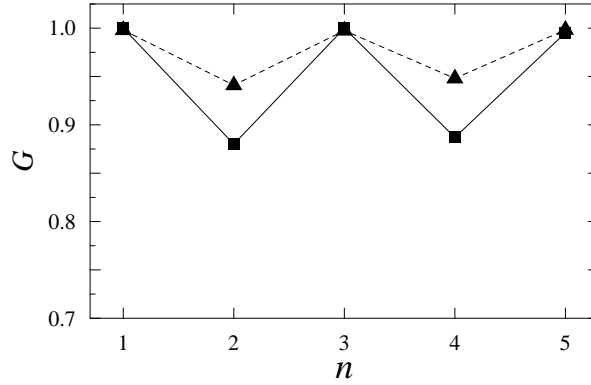


**Figure 4.15** : Conductance (in units of  $G_0$ ) as a function of the number of atoms in the atomic wire. The triangles correspond to linear wires with  $d = 6.30a_0$  and the squares to wires with optimized geometry.

quantum unit. This is actually predicted by the tight-binding model for any odd-numbered wire whose geometry has mirror symmetry with respect to a plane through the center and perpendicular to the wire, provided  $\Delta\varepsilon = 0$ .

One might expect the conductance for even-numbered wires to decrease with the length of the wire, due to the effect of dimerization as discussed in the previous section. This does not show in Fig. 4.15, because the dimerization in the optimized geometry is much weaker. Therefore, the effect will show up only in wires that are much longer.

## 4.5 Beyond linear response

In the linear response regime the current and therefore the conductance are fully determined by the electrons at the Fermi energy. If a finite bias  $V$  is applied then the current is given by

$$I = G_0 \int_{E_F - V/2}^{E_F + V/2} T(E, V) dE, \quad (4.6)$$

where the transmission coefficient  $T(E, V)$  depends on the energy of electron  $E$  and the voltage  $V$ . The differential conductance is defined as  $G(V) = dI/dV$ .

In this section we discuss some of the consequences of a finite bias. We make the approximation  $T(E, V) \approx T(E)$ , which is valid for a relatively small voltage in the limit that the electronic structure of the wire is not changed by the voltage. Examples of transmissions as a function of energy are given in Fig. 4.4 for atomic wires with the “reference” geometry  $d = d_c = 6.91a_0$ . The corresponding  $I$ - $V$  curves,

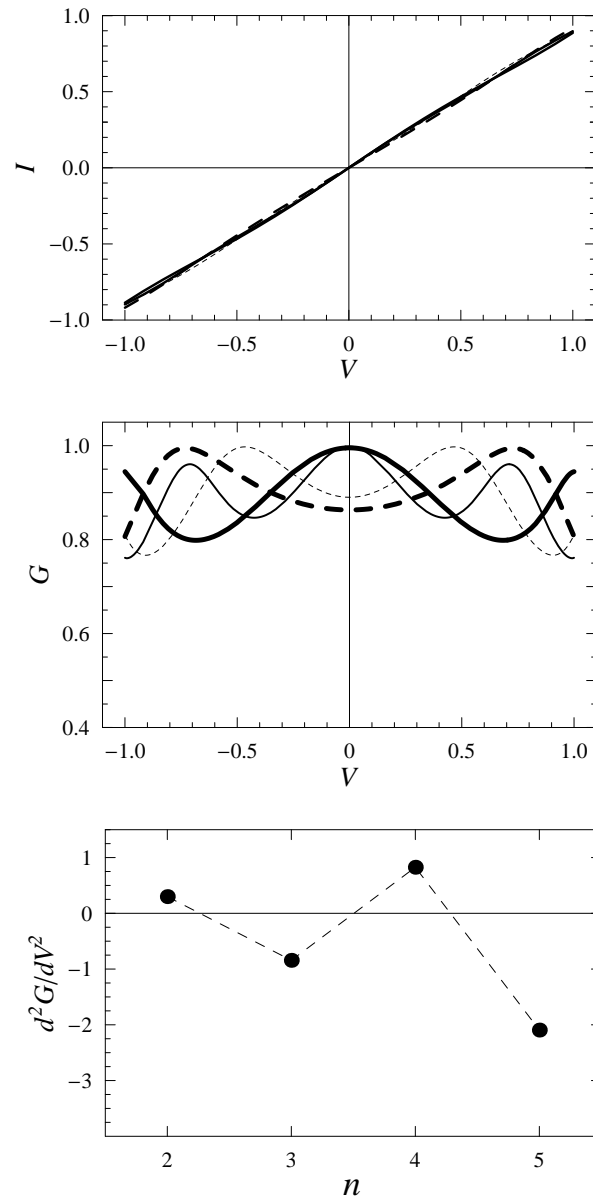


**Figure 4.16** : Current-voltage characteristics for two (thick dashed line), three (thick line), four (thin dashed line) and five (thin line) atomic wires with  $d = d_c = 6.91$  a.u.. The top, middle and bottom figures contain  $I$ - $V$  curves, the differential conductance  $G(V) = dI/dV$  as a function of  $V$  and the second derivative of the conductance  $d^2G(0)/dV^2$  as a function of the number of atoms, respectively.

calculated from Eq. (4.6), are given in Fig. 4.16. From the  $I$ - $V$  curves we calculate the differential conductance and the second derivative of the conductance, which are also presented in Fig. 4.16.

The conductance varies by less than 5% for biases up to  $\sim \pm 0.2\text{V}$ , which one might call the linear response regime. The conductance decreases monotonically for odd-numbered wires and it increases monotonically for even-numbered wires for biases up to  $\sim 0.5\text{V}$ . The oscillating behavior of the conductance at higher biases results from the resonant peaks in the transmission. At biases larger than  $\sim 0.5\text{V}$  the non self-consistent procedure probably becomes increasingly inaccurate [163].

An important characteristic of the conductance curve that can be measured experimentally, is its second derivative at the Fermi energy. If the transmission near the Fermi energy  $E_F = 0$  is approximated by a polynomial function  $T(E) = T(0) + T(0)'' E^2$  then the differential conductance is  $G(V) = G_0 [T(0) + T(0)'' V^2/4]$ . In Sec. 4.3 we interpreted the even-odd conductance oscillation of the conductance in terms of switching between off- and on-resonance behavior. If this is true then the second derivative of the conductance  $d^2G/d^2V = T(0)''/2$  must be positive for even-numbered wires and negative for odd-numbered wires at the Fermi energy, as shown in Fig. 4.16. At the same time the first derivative is zero.

## 4.6 Discussion

In this section we compare our results to those obtained in previous studies. The oscillating behavior of the conductance of monatomic sodium wires was first suggested from calculations using planar jellium electrodes [137]. The conductance of both even and odd-numbered wires is then significantly lower than the quantum unit and the conductance of even-numbered wires is larger than that of odd-numbered ones. Both of these features are likely to be artifacts of using jellium electrodes, since adding atomic bases between wire and jellium leads reverses the phase of the conductance oscillation and makes the conductance of odd-numbered wires approach the quantum unit [158,163]. Calculations using tip-shaped jellium electrodes predict that the phase of the conductance oscillation critically depend upon the sharpness of the tips [162], although this effect is disputed in recent calculations [184].

Using atomistic electrodes with a bulk structure our calculations show that the conductance has a regular even-odd oscillation, in which the conductance of the odd-numbered wires in optimized structures is close to the quantum unit and that of even-numbered wires is approximately 10% lower. Only the latter is modified substantially if the geometry of the wire or the contacts between wire and electrodes are changed within reasonable bounds. Apparently jellium electrodes cause reflections of electrons trying to enter the wire, which results in the artifacts discussed above. The amplitude of the conductance oscillation we find, is smaller by  $\sim 67\%$  than that obtained using jellium electrodes plus atomic bases. This would indicate that atomic bases do not completely remove the reflections caused by the jellium electrodes.

Calculations based upon one-dimensional metal electrodes predict that it is possible to change the phase of the conductance oscillation by varying the coupling



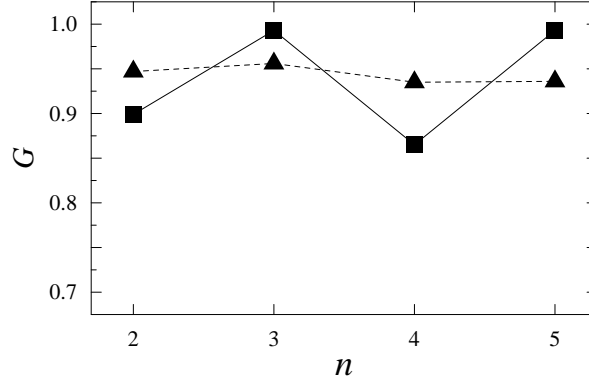


**Figure 4.17** : Conductance (in units of  $G_0$ ) as a function of the number of atoms in the atomic wire. Triangles and squares correspond to using a potential obtained from a total energy calculation with energy convergence criterion set to  $\Delta E = 2 \cdot 10^{-5}$  and  $5 \cdot 10^{-7}$  Hartrees, respectively.

between the wire and the electrodes [208]. We did not observe such an effect for three-dimensional atomistic electrodes. In a recent calculation it is found that the conductance of odd-numbered wires decreases sharply with increasing wire length, and even the phase of the conductance oscillation can be reversed in long wires [210]. This is not confirmed by our calculations, where the conductance of odd-numbered wires stays close to the quantum unit and the phase of the oscillation is stable. Experiments on the even-odd conductance oscillation in monovalent gold wires do not reveal a decrease of the conductance in odd-numbered wires, and the conductance stays close to the quantum unit [82].

Other studies seem to indicate that the phase of the even-odd conductance oscillation does not depend very sensitively upon the structure of the electrodes, since the same phase is observed in calculations using bcc electrodes oriented in the (111) direction [161], and in calculations using electrodes with an artificial fcc structure [164]. The amplitude of the oscillation is much more sensitive, however. A previous study on sodium wires suspended between sodium electrodes gives an amplitude of only 1%, which is an order of magnitude smaller than what we find using similar geometries [207]. Although we don't know what the cause of this difference is, we observe that the amplitude of the even-odd conductance oscillation is sensitive to the one-electron potential used in solving the scattering problem. This potential is obtained from a self-consistent electronic structure calculation. Such calculations frequently use a convergence criterion applied to the total energy. However, since a variational principle does not apply to the one-electron potential, the convergence criterion should be much stricter in order to converge the potential.

As an illustration, Fig. 4.17 shows the conductance of sodium wires calculated

from a potential obtained with the usual energy convergence criterion, compared to one obtained with a stricter energy convergence criterion. We have checked that the result does not change anymore if the convergence criterion is even made stricter. This figure clearly shows that changes in the potential that are caused by small charge transfers can markedly influence the amplitude of the even-odd conductance oscillation.

## 4.7 Summary and Conclusions

We have performed first-principles calculations to study the stability of even-odd conductance oscillations in a sodium monatomic wire with respect to structural variations. An infinite sodium wire can be linear and consists of equidistant atoms or dimers of atoms, or it can have a zigzag structure, depending upon the tension or compression applied to the wire. The geometry of finite sodium wires, suspended between two sodium electrodes, is influenced by boundary effects. Wires comprising an even or odd number of atoms are dimerized, but odd-numbered wires have a topological defect in the center.

In the linear response regime the conductance is determined by the electrons at the Fermi energy. The conductance of sodium wires shows a distinct even-odd oscillation. The odd-numbered wires have a conductance close the quantum unit  $G_0 = e^2/\pi\hbar$  and even numbered wires have a lower conductance. This oscillation is remarkably robust, as we show by systematically varying the structure of the wires and the geometry of the contacts between the wires and the electrodes. The phase of the oscillation is not affected by these structural variations, i.e. odd-numbered wires have a higher conductance than even-numbered ones. Moreover, odd numbered wires have a conductance close to the quantum unit, unless the structural deformation of the wire becomes very large and the contact to the left lead is markedly different from that to the right lead. The conductance of even-numbered wires is much more sensitive to the wire geometry. Increasing the interatomic distances in the wire and/or strengthening the contacts between wire and leads increases the conductance of even-numbered wires; increasing the asymmetry between the interatomic distances or between left and right contacts decreases the conductance.

These results can be interpreted on the basis of resonant transmission. For odd-numbered wires the Fermi energy coincides with a resonance in the transmission, whereas for even-numbered wires the Fermi energy is between two resonances. Changing the geometry of the wire or the contacts affects the spacing between the resonances and their widths and therefore it affects the conductance of even numbered wires; decreasing the spacing and/or increasing the widths increases the conductance. Since for odd numbered wires the Fermi level is pinned at a resonance, their conductance is affected much less by changing the wire geometry.

We have formulated a simple tight-binding model to analyze these results. It shows that the even-odd conductance oscillation is stable with respect to structural variations, unless the on-site energies for atoms in the wire are substantially different from the on-site energies of atoms in the leads. Note that a large difference in on-site

energies is necessarily accompanied by a significant charge transfer between the wire and the leads. The results of the first principles calculations demonstrate that this is not the case. For wires with equidistant atoms that have mirror symmetry with respect to a plane perpendicular to the wire, Eq. (4.2) shows that if all on-site energies are identical, the conductance of odd-numbered wires is one quantum unit, whereas that of even numbered wires is determined by the ratio of the wire-lead coupling and the atom-atom coupling within the wire. Breaking the mirror symmetry, Eq. (4.5) shows that the conductance of odd numbered wires becomes smaller than one unit. The symmetry breaking has to be large, however, in order to have a sizable effect on the conductance.

We have also calculated the current-voltage characteristics of sodium wires in the low bias regime. The differential conductance clearly shows a non-monotonic behavior. In particular, the second derivative of the conductance has an alternating sign as a function of the number of atoms in the wire; even-numbered wires have a positive second derivative and odd-numbered wires a negative one. This effect can be ascribed to the resonant nature of the transmission. It could be used to establish the resonant behavior of the even-odd conductance oscillation experimentally.

Comparison to other work shows that simple jellium electrodes do not reproduce the even-odd conductance oscillation correctly. Using atomic bases yields the correct phase of the oscillation. The conductance of odd-numbered wires is rather stable with respect to varying the atomic structure, but that of even-numbered wires is sensitive to structural details and the quality of the one-electron potential.



## Appendix A

# Appendix to Chapter 2

### A.1 Velocity matrix

In this appendix we will prove that

$$\mathbf{V}(\pm)_{m,n} = \frac{\hbar}{a} v_m(\pm) \delta_{m,n}, \quad (\text{A.1})$$

for the expression introduced for the velocity matrices in Sec. 2.5.4, Eq. (2.59). Here,  $a$  is the translation period along the wire and, for right- respectively left-propagating states,  $v_n(\pm)$  is the Bloch velocity in the direction of the quantum wire. For evanescent states  $v_n(\pm) = 0$ .

For ease of notation we drop the index  $\pm$  in the following. From Eq. (2.4) and its complex conjugate one has

$$\begin{aligned} -\mathbf{u}_m^\dagger \mathbf{B} \mathbf{u}_n + \lambda_n \mathbf{u}_m^\dagger (E\mathbf{I} - \mathbf{H}) \mathbf{u}_n - (\lambda_n)^2 \mathbf{u}_m^\dagger \mathbf{B}^\dagger \mathbf{u}_n &= 0, \\ -\mathbf{u}_m^\dagger \mathbf{B}^\dagger \mathbf{u}_n + \lambda_m^* \mathbf{u}_m^\dagger (E\mathbf{I} - \mathbf{H}) \mathbf{u}_n - (\lambda_m^*)^2 \mathbf{u}_m^\dagger \mathbf{B} \mathbf{u}_n &= 0. \end{aligned} \quad (\text{A.2})$$

Multiplying the first equation by  $\lambda_m^*$ , the second by  $\lambda_n$  and subtracting the two gives

$$\begin{aligned} [\lambda_n \mathbf{u}_m^\dagger \mathbf{B}^\dagger \mathbf{u}_n - \lambda_m^* \mathbf{u}_m^\dagger \mathbf{B} \mathbf{u}_n] (1 - \lambda_m^* \lambda_n) &= 0 \Leftrightarrow \\ -i \mathbf{V}_{m,n} (1 - \lambda_m^* \lambda_n) &= 0, \end{aligned} \quad (\text{A.3})$$

according to Eq. (2.59). So if  $\lambda_m^* \lambda_n \neq 1$  then  $\mathbf{V}_{m,n} = 0$ .

The velocity matrices contain, by construction, either right- or left-going modes. For right-going evanescent modes one has  $|\lambda| < 1$ , for left-going evanescent modes  $|\lambda| > 1$ , so  $\lambda_m^* \lambda_n \neq 1$  if  $n$  and/or  $m$  denotes an evanescent mode; thus  $\mathbf{V}_{m,n} = 0$ . For propagating states,  $|\lambda_m| = 1$  and one can write  $\lambda_m = \exp(ik_m a)$ . It is obvious that if  $k_m \neq k_n$ , then  $\lambda_m^* \lambda_n \neq 1$  and again  $\mathbf{V}_{m,n} = 0$ .

This argument does not hold for the diagonal matrix elements of propagating states, and also not for degenerate propagating states, i.e. if  $\lambda_m = \lambda_n$ . In the latter case we take the derivative  $d/dE$  of the first line of Eq. (A.2). The coefficients

of the terms in  $d\mathbf{u}_n/dE$  and  $d\mathbf{u}_m^\dagger/dE$  vanish because  $\mathbf{u}_n$  and  $\mathbf{u}_m^\dagger$  satisfy the eigenvalue equation Eq. (2.4) and its complex conjugate, respectively, and  $\lambda_n^* = 1/\lambda_n$  for propagating states. Collecting the remaining terms gives

$$\begin{aligned} -\frac{d\lambda_n}{dE} [\lambda_n \mathbf{u}_m^\dagger \mathbf{B}^\dagger \mathbf{u}_n - \lambda_n^* \mathbf{u}_m^\dagger \mathbf{B} \mathbf{u}_n] + \lambda_n \mathbf{u}_m^\dagger \mathbf{u}_n &= 0 \Leftrightarrow \\ i \frac{d\lambda_n}{dE} \mathbf{V}_{m,n} + \lambda_n \mathbf{u}_m^\dagger \mathbf{u}_n &= 0, \end{aligned} \quad (\text{A.4})$$

where we emphasize that for  $m \neq n$  this only holds for degenerate propagating states. Without loss of generality, degenerate states can be chosen orthogonal, i.e.  $\mathbf{u}_m^\dagger \mathbf{u}_n = 0$  for  $m \neq n$ . Since  $d\lambda_n/dE \neq 0$ , it then follows that  $\mathbf{V}_{m,n} = 0$  if  $m \neq n$ .

The diagonal matrix elements  $m = n$  for propagating states are also given by Eq. (A.4). Setting  $n = m$  and using the fact that the states are normalized, i.e.  $\mathbf{u}_n^\dagger \mathbf{u}_n = 1$  gives the expression

$$\mathbf{V}_{n,n} = i \lambda_n \frac{dE}{d\lambda_n}. \quad (\text{A.5})$$

Since for propagating states we can write  $\lambda_n = \exp(ika)$  and the Bloch velocity is defined as  $v_n = \hbar^{-1} dE/dk$ , this then proves both Eq. (A.1) and Eq. (2.5).

It is straightforward to derive an alternative expression for the velocity matrices in terms of the advanced matrices

$$\mathbf{V}(\pm) = i [\mathbf{U}^{a\dagger}(\mp) \mathbf{B}^\dagger \mathbf{U}^a(\mp) \mathbf{\Lambda}^{a\dagger}(\mp) - \mathbf{\Lambda}^{a\dagger}(\mp) \mathbf{U}^{a\dagger}(\mp) \mathbf{B} \mathbf{U}^a(\mp)]. \quad (\text{A.6})$$

Multiplying from the left by  $[\mathbf{\Lambda}^{a\dagger}]^{-1}$  and from the right by  $[\mathbf{\Lambda}^a]^{-1}$  this expression is seen to be equivalent to

$$\mathbf{V}(\pm) = i [\{\mathbf{\Lambda}^{a\dagger}(\mp)\}^{-1} \mathbf{U}^{a\dagger}(\mp) \mathbf{B}^\dagger \mathbf{U}^a(\mp) - \mathbf{U}^{a\dagger}(\mp) \mathbf{B} \mathbf{U}^a(\mp) \{\mathbf{\Lambda}^a(\mp)\}^{-1}]. \quad (\text{A.7})$$

## A.2 Projector matrix

In order to prove Eq. (2.63), we start from Eq. (2.14) and rewrite it using Eq. (2.42) as

$$\mathbf{Q}_0 = \mathbf{B}_L \mathbf{F}_L^{-1}(+) - [\mathbf{F}_L^{a\dagger}(-)]^{-1} \mathbf{B}_L^\dagger. \quad (\text{A.8})$$

In the following we will drop the subscript L for ease of notation. Multiplying (A.8) on the left with the identity operator  $\mathbf{I} = \sum \mathbf{u}_n(+) \tilde{\mathbf{u}}_n^\dagger(+)$  and on the right with  $\mathbf{I} = \sum \tilde{\mathbf{u}}_m^a(-) \mathbf{u}_m^{a\dagger}(-)$  yields

$$\mathbf{Q}_0 = \sum_{m,n=1}^N \tilde{\mathbf{u}}_m^a(-) \tilde{\mathbf{u}}_n^\dagger(+) \left[ \frac{1}{\lambda_n(+)} \mathbf{u}_m^{a\dagger}(-) \mathbf{B} \mathbf{u}_n(+) - \frac{1}{\lambda_m^{a*}(-)} \mathbf{u}_m^{a\dagger}(-) \mathbf{B}^\dagger \mathbf{u}_n(+) \right], \quad (\text{A.9})$$

where use has been made of Eqs. (2.6), (2.7) and (2.36).

By similar arguments as those leading to Eq. (A.3) it follows that  $[\dots] = 0$ , unless  $\lambda_m^a(-) = 1/\lambda_n^*(+)$ . From Eq. (2.36) it follows that this is true if  $n = m$  and  $n$  denotes a propagating mode. In addition, for every (+) evanescent mode  $n$  with eigenvalue  $\lambda_n(+)$ , there is one (-) evanescent mode with eigenvalue  $\lambda_n(-) = 1/\lambda_n^*(+)$  [112]. Again it follows from Eq. (2.36) that only the  $m = n$  terms are non-zero for evanescent modes in Eq. (A.9). This equation then simplifies to

$$\begin{aligned} \mathbf{Q}_0 &= \sum_{n=1}^{N_p} \tilde{\mathbf{u}}_n^a(-) \tilde{\mathbf{u}}_n^\dagger(+)\left[\frac{1}{\lambda_n(+)} \mathbf{u}_n^\dagger(+)\mathbf{B}\mathbf{u}_n(+)-\lambda_n(+)\mathbf{u}_n^\dagger(+)\mathbf{B}^\dagger\mathbf{u}_n(+)\right] \\ &+ \sum_{n=N_p+1}^N \tilde{\mathbf{u}}_n^a(-) \tilde{\mathbf{u}}_n^\dagger(+)\left[\frac{1}{\lambda_n(+)} \mathbf{u}_n^\dagger(-)\mathbf{B}\mathbf{u}_n(+)-\lambda_n(+)\mathbf{u}_n^\dagger(-)\mathbf{B}^\dagger\mathbf{u}_n(+)\right], \end{aligned} \quad (\text{A.10})$$

where the first summation is over the  $N_p$  propagating modes and the second summation is over the  $N - N_p$  evanescent modes.

The projector matrix  $\mathbf{P}$  is defined by Eq. (2.62). In the product  $\mathbf{Q}_0\mathbf{P}$  only the first summation in Eq. (A.10) survives. Moreover, since  $[\dots] = i\mathbf{V}_{n,n}$  according to Eq. (A.3), we have

$$\mathbf{Q}_0\mathbf{P} = i \sum_{n=1}^{N_p} \tilde{\mathbf{u}}_n^a(-) \tilde{\mathbf{u}}_n^{a\dagger}(-) \mathbf{V}_{n,n}(+). \quad (\text{A.11})$$

Together with Eq. (2.61) this then proves Eq. (2.63).





## Appendix B

# Appendix to Chapter 3

### B.1 H and B matrices

In this section the matrices  $\mathbf{H}_i$  and  $\mathbf{B}$ , introduced in Sec. 3.2.1, are presented explicitly. In order not to complicate the notation the subscript  $i$  is dropped; all quantities refer to a single cell. For a wire with a finite cross-section in the  $yz$  plane, the matrix  $\mathbf{H}$  is real and symmetric and has the form

$$\mathbf{H} = \begin{pmatrix} \mathbf{h}_1 & -\boldsymbol{\beta}_1 & \dots & -\boldsymbol{\beta}_N & 0 & \dots & 0 & 0 \\ -\boldsymbol{\beta}_1 & \mathbf{h}_2 & \dots & -\boldsymbol{\beta}_{N-1} & -\boldsymbol{\beta}_N & \dots & 0 & 0 \\ \vdots & \vdots & \vdots & \vdots & \vdots & \vdots & \vdots & \vdots \\ 0 & 0 & \dots & 0 & 0 & \dots & \mathbf{h}_{L-1} & -\boldsymbol{\beta}_1 \\ 0 & 0 & \dots & 0 & 0 & \dots & -\boldsymbol{\beta}_1 & \mathbf{h}_L \end{pmatrix}. \quad (\text{B.1})$$

Here  $N$  is the order of the finite-difference formula used, see Eq. (3.3). We assume that the  $x$ -axis is in the direction of the wire.  $L$  is the number of grid points in the  $x$ -direction of the unit cell defined by the periodic potential.

The submatrices  $\mathbf{h}_n$  and  $\boldsymbol{\beta}_n$  are of dimension  $W_y \times W_z$ , which is the number of grid points in the cross section of the wire. Denoting  $(k, l) = k + (l - 1)W_y$ ;  $k = 1, \dots, W_y$ ;  $l = 1, \dots, W_z$  as the compound index covering the grid points in the cross section, the non-zero elements of these matrices are easily derived from Eq. (3.4).

$$\begin{aligned} (\mathbf{h}_j)_{(k,l),(k,l)} &= V_{j,k,l} - (t_0^x + t_0^y + t_0^z) \\ (\mathbf{h}_j)_{(k,l),(k+n,l)} &= -t_n^y, \quad n \neq 0 \\ (\mathbf{h}_j)_{(k,l),(k,l+n')} &= -t_{n'}^z, \quad n' \neq 0 \\ (\boldsymbol{\beta}_j)_{(k,l),(k,l)} &= t_j^x, \end{aligned} \quad (\text{B.2})$$

where  $-N \leq n, n' \leq N$  and  $1 \leq k, k + n \leq W_y$ ;  $1 \leq l, l + n' \leq W_z$ ;  $1 \leq j \leq N$ . Note that in writing down these matrices we have assumed that  $N < L, W_y, W_z$ . In practical calculations on realistic systems this will always be the case.

The matrix  $\mathbf{B}$  has the same dimension as  $\mathbf{H}$ , but it is upper triangular

$$\mathbf{B} = \begin{pmatrix} 0 & \dots & 0 & \beta_N & \beta_{N-1} & \dots & \beta_1 \\ 0 & \dots & 0 & 0 & \beta_N & \dots & \beta_2 \\ \vdots & \vdots & \vdots & \vdots & \vdots & \vdots & \vdots \\ 0 & \dots & 0 & 0 & 0 & \dots & \beta_N \\ \vdots & \vdots & \vdots & \vdots & \vdots & \vdots & \vdots \\ 0 & \dots & 0 & 0 & 0 & \dots & 0 \end{pmatrix}. \quad (\text{B.3})$$

For a wire that is periodic in the  $yz$  plane, the wave functions in Eq. (3.4) must obey Bloch conditions. That is,  $\Psi_{j,k+W_y,l} = e^{ik_y a_y} \Psi_{j,k,l}$  and  $\Psi_{j,k,l+W_z} = e^{ik_z a_z} \Psi_{j,k,l}$ , where  $a_y, a_z$  are the periods in the  $y$  and  $z$  directions, and  $(k_y, k_z) = \mathbf{k}_{\parallel}$  is the Bloch wave vector in the  $yz$  plane. These Bloch conditions in the  $yz$  plane can be taken into account by defining the blocks

$$\begin{aligned} (\mathbf{h}'_j)_{(k,l),(k+W_y+n,l)} &= -t_n^y e^{-ik_y a_y}, \quad n = -N, \dots, -k \\ (\mathbf{h}'_j)_{(k,l),(k-W_y+n,l)} &= -t_n^y e^{ik_y a_y}, \quad n = W_y - k, \dots, N \\ (\mathbf{h}'_j)_{(k,l),(k,l+W_z+n')} &= -t_{n'}^z e^{-ik_z a_z}, \quad n' = -N, \dots, -l \\ (\mathbf{h}'_j)_{(k,l),(k,l-W_z+n')} &= -t_{n'}^z e^{ik_z a_z}, \quad n' = W_z - l, \dots, N. \end{aligned} \quad (\text{B.4})$$

The matrix  $\mathbf{H}(\mathbf{k}_{\parallel})$ , which is obtained by substituting  $\mathbf{h}_j$  by  $\mathbf{h}_j + \mathbf{h}'_j; j = 1, \dots, L$  in Eq. (B.1) describes a wire that is periodic in the  $yz$  plane with solutions corresponding to a Bloch vector  $\mathbf{k}_{\parallel}$ . This matrix is (complex) Hermitian.

## B.2 Ideal wire

For an ideal wire, which has a periodic potential along the wire, Eq. (3.7) has to be solved to find the propagating and the evanescent waves. The precise form of the submatrices in Eqs. (B.1) and (B.3) is not important in the following discussion. For ease of notation we only mention the dimensions  $L$  (the number of grid points in the  $x$ -direction) and  $N$  (the order of the finite-difference expression) explicitly and treat the wire as quasi one-dimensional. To find the dimensions of the matrices in the three-dimensional case, one simply has to multiply the dimensions mentioned below by  $W_y \times W_z$ .

Eq. (3.7) is a generalized eigenvalue problem of dimension  $2L$ . Because the matrix  $\mathbf{B}$  is singular it has a number of trivial solutions  $\lambda = 0$  and  $\lambda = \infty$ . By using a partitioning technique we will eliminate these trivial solutions and reduce the problem to the  $2N$  non-trivial solutions. The key point is to split the vectors  $\Psi_i$  into two parts containing the first  $L - N$  and last  $N$  elements, respectively. The two parts are denoted by the subscripts 1 and 2. Splitting the matrices  $\mathbf{H}$  and  $\mathbf{B}$  in the same way one gets

$$\Psi_i = \begin{pmatrix} \Psi_{i,1} \\ \Psi_{i,2} \end{pmatrix}; \quad \mathbf{H} = \begin{pmatrix} \mathbf{H}_{11} & \mathbf{H}_{12} \\ \mathbf{H}_{21} & \mathbf{H}_{22} \end{pmatrix}; \quad \mathbf{B} = \begin{pmatrix} 0 & \mathbf{B}_{12} \\ 0 & \mathbf{B}_{22} \end{pmatrix}. \quad (\text{B.5})$$

Note the special form of the matrix  $\mathbf{B}$ .

This splitting allows Eq. (3.7) to be written in the form

$$\begin{pmatrix} EI_{11} - \mathbf{H}_{11} & -\mathbf{H}_{12} & 0 & \mathbf{B}_{12} \\ -\mathbf{H}_{21} + \lambda \mathbf{B}_{21}^\dagger & EI_{22} - \mathbf{H}_{22} + \lambda \mathbf{B}_{22}^\dagger & 0 & \mathbf{B}_{22} \\ \mathbf{I}_{11} & 0 & -\lambda \mathbf{I}_{11} & 0 \\ 0 & \mathbf{I}_{22} & 0 & -\lambda \mathbf{I}_{22} \end{pmatrix} \times \begin{pmatrix} \Psi_{i,1} \\ \Psi_{i,2} \\ \Psi_{i-1,1} \\ \Psi_{i-1,2} \end{pmatrix} = 0, \quad (\text{B.6})$$

From this expression it is clear that the component  $\Psi_{i-1,1}$  only enters the problem in a trivial way as  $\Psi_{i-1,1} = 1/\lambda \times \Psi_{i,1}$ . It can be eliminated by deleting the third row and column in Eq. (B.6).

Furthermore the first row of the matrix does not depend upon the eigenvalue  $\lambda$ . Writing out the multiplication for the first row explicitly, one finds an expression for  $\Psi_{i,1}$

$$\Psi_{i,1} = (EI_{11} - \mathbf{H}_{11})^{-1} (\mathbf{H}_{12} \Psi_{i,2} - \mathbf{B}_{12} \Psi_{i-1,2}). \quad (\text{B.7})$$

This can be used to eliminate  $\Psi_{i,1}$  from Eq. (B.6) to arrive at the equation

$$\left[ \begin{pmatrix} \mathbf{A}_{11} & \mathbf{A}_{12} \\ \mathbf{I}_{22} & 0 \end{pmatrix} - \lambda \begin{pmatrix} \mathbf{S}_{11} & \mathbf{S}_{12} \\ 0 & \mathbf{I}_{22} \end{pmatrix} \right] \begin{pmatrix} \Psi_{i,2} \\ \Psi_{i-1,2} \end{pmatrix} = 0, \quad (\text{B.8})$$

with

$$\begin{aligned} \mathbf{A}_{11} &= EI_{22} - \mathbf{H}_{22} - \mathbf{H}_{21} (EI_{11} - \mathbf{H}_{11})^{-1} \mathbf{H}_{12} \\ \mathbf{A}_{12} &= -\mathbf{H}_{21} (EI_{11} - \mathbf{H}_{11})^{-1} \mathbf{B}_{12} \\ \mathbf{S}_{11} &= -\mathbf{B}_{22}^\dagger - \mathbf{B}_{21}^\dagger (EI_{11} - \mathbf{H}_{11})^{-1} \mathbf{H}_{12} \\ \mathbf{S}_{12} &= -\mathbf{B}_{21}^\dagger (EI_{11} - \mathbf{H}_{11})^{-1} \mathbf{B}_{12}. \end{aligned} \quad (\text{B.9})$$

Eq. (B.8) is a generalized eigenvalue problem of dimension  $2N$  that can be solved using standard numerical techniques [110]. In general it gives  $2N$  eigenvalues  $\lambda_m$  and eigenvectors  $\mathbf{u}_m$ . As mentioned in the text, some of these solutions are non-physical [152, 153], others represent extremely fast growing or decaying waves. Both of these classes of unwanted solutions are easily filtered out by demanding that  $1/\delta < |\lambda| < \delta$ , where  $\delta$  is some threshold value. We use this criterion to select the physically relevant solutions, which are then separated into  $M$  right-going and  $M$  left-going solutions. These are used to construct the matrices of Eqs. (3.8) and (3.11) which contain all the information required to describe the ideal wire.

The computational cost of solving Eq. (B.8) scales as  $(2N)^3$ , whereas the cost of computing the matrices of Eq. (B.9) basically scales as  $(L - N)^3$  (which is the cost of the matrix inversion involved). Depending on the relative sizes of  $L$  and  $N$  one of these two steps is dominant.

### B.3 F matrices

In this section explicit expression for the matrices  $\mathbf{F}$  and  $\tilde{\mathbf{F}}$  are given, see Eqs. (3.13) and (3.14). Following Eq. (3.8), we denote the propagating and evanescent modes of the ideal wire by  $\mathbf{u}_m; m = 1, \dots, M$ , where  $M < N_{\text{rs}}$  and  $N_{\text{rs}}$  is the dimension of the vectors. For clarity of notation we omit the labels  $\pm$  for right- and left-going modes here. As in Eq. (3.8) we form the  $N_{\text{rs}} \times M$  matrix

$$\mathbf{U} = (\mathbf{u}_1 \cdots \mathbf{u}_M) \quad (\text{B.10})$$

$$= \begin{pmatrix} u_{11} & \cdots & u_{1M} \\ \vdots & & \vdots \\ u_{N_{\text{rs}}1} & \cdots & u_{N_{\text{rs}}M} \end{pmatrix}. \quad (\text{B.11})$$

The mode vectors  $\mathbf{u}_m$  are in general non-orthogonal and we can form the  $M \times M$  (positive definite) overlap matrix with elements

$$S_{mn} = \mathbf{u}_m^\dagger \mathbf{u}_n \equiv \langle \mathbf{u}_m | \mathbf{u}_n \rangle. \quad (\text{B.12})$$

This allows us to construct the dual basis  $\tilde{\mathbf{u}}_m; m = 1, \dots, M$

$$\tilde{\mathbf{u}}_m = \sum_{n=1}^M S_{mn}^{-1} \mathbf{u}_n, \quad (\text{B.13})$$

with properties

$$\langle \tilde{\mathbf{u}}_m | \mathbf{u}_n \rangle = \langle \mathbf{u}_m | \tilde{\mathbf{u}}_n \rangle = \delta_{mn}. \quad (\text{B.14})$$

Now define the  $M \times N_{\text{rs}}$  matrix

$$\begin{aligned} \tilde{\mathbf{U}} &= (\tilde{\mathbf{u}}_1 \cdots \tilde{\mathbf{u}}_M)^\dagger \\ &= \begin{pmatrix} \tilde{u}_{11}^* & \cdots & \tilde{u}_{N_{\text{rs}}1}^* \\ \vdots & & \vdots \\ \tilde{u}_{1M}^* & \cdots & \tilde{u}_{N_{\text{rs}}M}^* \end{pmatrix}. \end{aligned} \quad (\text{B.15})$$

$\tilde{\mathbf{U}}$  is called the pseudo-inverse of  $\mathbf{U}$ ; note that  $\tilde{\mathbf{U}}\mathbf{U} = \mathbf{I}_M$ , where  $\mathbf{I}_M$  is the  $M \times M$  identity matrix [110].

Defining the matrix

$$\mathbf{F} = \mathbf{U}\Lambda\tilde{\mathbf{U}}, \quad (\text{B.16})$$

it is easy to show that it is a solution to Eq. (3.13).  $\mathbf{F}$  is in fact a matrix that projects onto the space spanned by the modes, as is easily demonstrated by writing Eq. (B.16) as

$$\mathbf{F} = \sum_{m=1}^M |\mathbf{u}_m\rangle \lambda_m \langle \tilde{\mathbf{u}}_m|, \quad (\text{B.17})$$

making use of Eqs. (3.11) and (B.10)-(B.15). In a similar way a solution to Eq. (3.14) is formed by

$$\tilde{\mathbf{F}} = \mathbf{U}\mathbf{\Lambda}^{-1}\tilde{\mathbf{U}} = \sum_{m=1}^M |\mathbf{u}_m\rangle\lambda_m^{-1}\langle\tilde{\mathbf{u}}_m|. \quad (\text{B.18})$$

Note that  $\tilde{\mathbf{F}} = \mathbf{F}^{-1}$  only if  $M = N_{\text{rs}}$ , but since  $M \leq N \times W_x \times W_y < N_{\text{rs}}$  (see the previous section) this will never be the case.

## B.4 Scattering problem

The scattering problem is described by Eq. (3.26). It is conveniently written in matrix form as

$$\begin{pmatrix} \mathbf{A}_0 & \mathbf{B}^\dagger & 0 & \dots & 0 \\ \mathbf{B} & \mathbf{A}_1 & \mathbf{B}^\dagger & \dots & 0 \\ 0 & \mathbf{B} & \mathbf{A}_2 & \dots & 0 \\ \vdots & \vdots & \vdots & \ddots & \vdots \\ 0 & 0 & 0 & \dots & \mathbf{A}_{S+1} \end{pmatrix} \begin{pmatrix} \mathbf{C}_0 \\ \mathbf{C}_1 \\ \mathbf{C}_2 \\ \vdots \\ \mathbf{C}_{S+1} \end{pmatrix} = \begin{pmatrix} \mathbf{D} \\ 0 \\ 0 \\ \vdots \\ 0 \end{pmatrix}, \quad (\text{B.19})$$

with

$$\begin{aligned} \mathbf{A}_0 &= E\mathbf{I} - \tilde{\mathbf{H}}_0 \\ \mathbf{A}_i &= E\mathbf{I} - \mathbf{H}_i, \quad i = 1, \dots, S \\ \mathbf{A}_{S+1} &= E\mathbf{I} - \tilde{\mathbf{H}}_{S+1} \\ \mathbf{C}_0 &= \mathbf{U}_L(+)+\mathbf{U}_L(-)\mathbf{R} \\ \mathbf{C}_{S+1} &= \mathbf{U}_R(+)\mathbf{T} \\ \mathbf{D} &= \mathbf{Q}\mathbf{U}_L(+). \end{aligned} \quad (\text{B.20})$$

All the blocks  $\mathbf{A}$ - $\mathbf{D}$  are  $N_{\text{rs}} \times N_{\text{rs}}$  matrices. Eq. (B.19) represents a set of linear equations, which can be solved directly using a standard algorithm. However, the dimension of this problem is  $N_{\text{tot}} = N_{\text{rs}} \cdot (S + 2)$ , which can be rather large. Since the computing cost scales as  $N_{\text{tot}}^3$  the direct route is not very practical.

It is however quite straightforward to construct an algorithm for which the computing cost scales as  $N_{\text{rs}}^3 \cdot S$ , i.e. only linearly with the size  $S$  of the scattering region. One has to make optimal use of the block tridiagonal form of the matrix in Eq. (B.19). The algorithm is a block form of Gaussian elimination. The first (and most time consuming) step of this algorithm is transforming the matrix into upper block triangular form by iteration

$$\left. \begin{aligned} \mathbf{A}'_0 &= \mathbf{A}_0; \quad \mathbf{D}'_0 = \mathbf{D}; \\ \mathbf{A}'_i &= \mathbf{A}_i - \mathbf{B}\mathbf{A}'_{i-1}\mathbf{B}^\dagger \\ \mathbf{D}'_i &= -\mathbf{B}\mathbf{A}'_{i-1}\mathbf{D}'_{i-1} \end{aligned} \right\} i = 1, \dots, S + 1. \quad (\text{B.21})$$

The inverse matrices  $\mathbf{A}'_{i-1}$  in this algorithm are actually not needed explicitly. Instead at each step one solves the sets of linear equations

$$\mathbf{A}'_{i-1}\tilde{\mathbf{B}}_i = \mathbf{B}^\dagger; \mathbf{A}'_{i-1}\tilde{\mathbf{D}}_i = \mathbf{D}'_{i-1}, \quad (\text{B.22})$$

by a standard algorithm, i.e.  $LU$  decomposition of  $\mathbf{A}'_{i-1}$  followed by back substitution, to obtain the matrices  $\tilde{\mathbf{B}}_i$  and  $\tilde{\mathbf{D}}_i$  [110]. This allows the steps in Eq. (B.21) to be rewritten as

$$\mathbf{A}'_i = \mathbf{A}_i - \mathbf{B}\tilde{\mathbf{B}}_i; \mathbf{D}'_i = -\mathbf{B}\tilde{\mathbf{D}}_i. \quad (\text{B.23})$$

The solution to Eq. (B.19) can now be found by back substitution

$$\left. \begin{aligned} \mathbf{C}_{S+1} &= \mathbf{A}'_{S+1}\mathbf{D}'_{S+1} \\ \mathbf{C}_i &= \tilde{\mathbf{D}}_{i+1} - \tilde{\mathbf{B}}_{i+1}\mathbf{C}_{i+1} \end{aligned} \right\} i = S, \dots, 0. \quad (\text{B.24})$$

Again one does not need  $\mathbf{A}'_{S+1}$  explicitly, but like Eq. (B.22) one can solve the equivalent set of linear equations. The reflection and transmission matrices  $\mathbf{R}$  and  $\mathbf{T}$  can be extracted using the special form of the matrices  $\mathbf{C}_0$  and  $\mathbf{C}_{S+1}$ , see Eq. (B.20).

Very often one is only interested in the transmission matrix. In that case one only uses the first step of the back substitution, Eq. (B.24), which can be written as

$$\mathbf{A}'_{S+1}\mathbf{U}_R(+)\mathbf{T} = \mathbf{D}'_{S+1}. \quad (\text{B.25})$$

This is a set of linear equations for the transmission probability amplitudes  $\mathbf{T}$ , which can be solved using a standard numerical techniques [110].

The time consuming steps consist of solving Eq. (B.22), the computing costs of which scale as  $N_{\text{rs}}^3$ .<sup>1</sup> Using Eq. (B.23) in Eq. (B.21) requires performing  $S+1$  of such steps and subsequently solving Eq. (B.25) scales as  $N_{\text{rs}}^3$ . Note that the full algorithm scales linearly with the size  $S$  of the scattering region.

## B.5 Velocities

In this section we give a short derivation of the expression for the velocities, Eq. (3.28). It is straightforward to show that the vectors  $\mathbf{u}_m$  of Eq. (3.8) are a solution of the quadratic eigenvalue equation

$$\lambda_m(E\mathbf{I} - \mathbf{H})\mathbf{u}_m + \mathbf{B}\mathbf{u}_m + \lambda_m^2\mathbf{B}^\dagger\mathbf{u}_m = 0. \quad (\text{B.26})$$

This quadratic eigenvalue equation of dimension  $N_{\text{rs}}$  is completely equivalent to the linear problem of dimension  $2N_{\text{rs}}$  of Eq. (3.7). If  $\mathbf{u}_m$  is a right eigenvector of Eq. (B.26) belonging to the eigenvalue  $\lambda_m$ , then by complex conjugation of this equation one shows that  $\mathbf{u}_m^\dagger$  is a left eigenvector belonging to the eigenvalue  $1/\lambda_m^*$ .

<sup>1</sup>One can make use of the special form of the  $\mathbf{H}$  and  $\mathbf{B}$  matrices, cf. Eqs. (B.1) and (B.3) to subdivide the blocks of the matrix in Eq. (B.19). This can speed up the algorithm by an order of magnitude. However, the overall scaling still is as  $N_{\text{rs}}^3 \cdot S$ .

For a propagating state  $|\lambda_m| = 1$ , so  $\lambda_m = 1/\lambda_m^*$ , which means that these left and right eigenvectors belong to the same eigenvalue.

We now start from

$$\lambda_m \mathbf{u}_m^\dagger (E\mathbf{I} - \mathbf{H})\mathbf{u}_m + \mathbf{u}_m^\dagger \mathbf{B}\mathbf{u}_m + \lambda_m^2 \mathbf{u}_m^\dagger \mathbf{B}^\dagger \mathbf{u}_m = 0, \quad (\text{B.27})$$

and take the derivative  $d/dE$  of this expression. All the terms with  $d\mathbf{u}_m/dE$  and  $d\mathbf{u}_m^\dagger/dE$  drop out, because  $\mathbf{u}_m$  and  $\mathbf{u}_m^\dagger$  obey Eq. (B.26) and its complex conjugate, respectively. The remaining terms can be collected and slightly rewritten using Eq. (B.26); the result is

$$\begin{aligned} & -\frac{d\lambda_m}{dE} (\lambda_m^{-1} \mathbf{u}_m^\dagger \mathbf{B}\mathbf{u}_m - \lambda_m \mathbf{u}_m^\dagger \mathbf{B}^\dagger \mathbf{u}_m) + \lambda_m \mathbf{u}_m^\dagger \mathbf{u}_m = \\ & 2i \frac{d\lambda_m}{dE} \text{Im} (\lambda_m \mathbf{u}_m^\dagger \mathbf{B}^\dagger \mathbf{u}_m) + \lambda_m = 0, \end{aligned} \quad (\text{B.28})$$

where the last line is obtained by making use of  $\lambda_m^{-1} = \lambda_m^*$  and the fact that the vectors are normalized,  $\mathbf{u}_m^\dagger \mathbf{u}_m = 1$ . Eq. (B.28) yields an expression for  $d\lambda_m/dE$ . For propagating states  $\lambda_m = e^{ik_x a_x}$  and thus

$$\frac{dk_x}{dE} = \frac{1}{ia_x \lambda_m} \frac{d\lambda_m}{dE} \quad (\text{B.29})$$

The usual definition of the Bloch velocity  $v_n = \hbar^{-1} dE/dk_x$  and the expression for  $d\lambda_m/dE$  extracted from Eq. (B.28) then give the expression for the velocity of Eq. (3.28).





## Appendix C

# Appendix to Chapter 4

### C.1 $\mathbf{k}_{\parallel}$ -point sampling

In this Appendix we discuss the effect of  $\mathbf{k}_{\parallel}$ -point sampling on the conductance. In modeling a conductor between two semi-infinite electrodes one usually assumes a supercell geometry in the lateral direction. The scattering region then consists of a periodic array of parallel wires, and the lateral supercell must be chosen large enough to prevent an interaction between these wires. To limit the computational demands the supercell is chosen as small as possible, without a significant loss of accuracy. According to the results obtained in Sec. 4.4.2, using a  $2 \times 2$  supercell is already sufficient for the Na system discussed here. We average the conductance over the 2D Brillouin zone (BZ)

$$G = \frac{1}{N_{\parallel}} \sum_{\mathbf{k}_{\parallel}} G_{\mathbf{k}_{\parallel}}, \quad (\text{C.1})$$

where  $N_{\parallel}$  is the number of  $\mathbf{k}_{\parallel}$ -points used for the BZ sampling. Calculating the conductance for an infinitely large supercell would include contributions from off-diagonal transmission amplitudes between different  $\mathbf{k}_{\parallel}$ . From our results we conclude that their contribution is small as compared to the contribution of the diagonal terms  $G_{\mathbf{k}_{\parallel}}$  already for a  $2 \times 2$  supercell.

The calculated conductance  $G_{\mathbf{k}_{\parallel}}$  as a function of  $\mathbf{k}_{\parallel}$  for four and five atomic wires is shown in Fig. C.1. The dispersion of the conductance is relatively small around the Fermi energy, which means that a coarse  $\mathbf{k}_{\parallel}$  grid,<sup>1</sup> or even a single  $\mathbf{k}_{\parallel}$ -point, is reasonable to calculate the conductance in linear response regime. This can be accidental, however, since Fig. C.1 demonstrates that the dispersion is quite large both for energies lower and for energies higher than the Fermi energy. Especially for higher energies a single  $\mathbf{k}_{\parallel}$ -point is clearly insufficient for calculating the conductance. This regime becomes important if current-voltage characteristics are calculated, because

---

<sup>1</sup>The results discussed in sections have been obtained using a  $6 \times 6$  grid in the BZ (6  $\mathbf{k}_{\parallel}$ -points in the irreducible BZ).

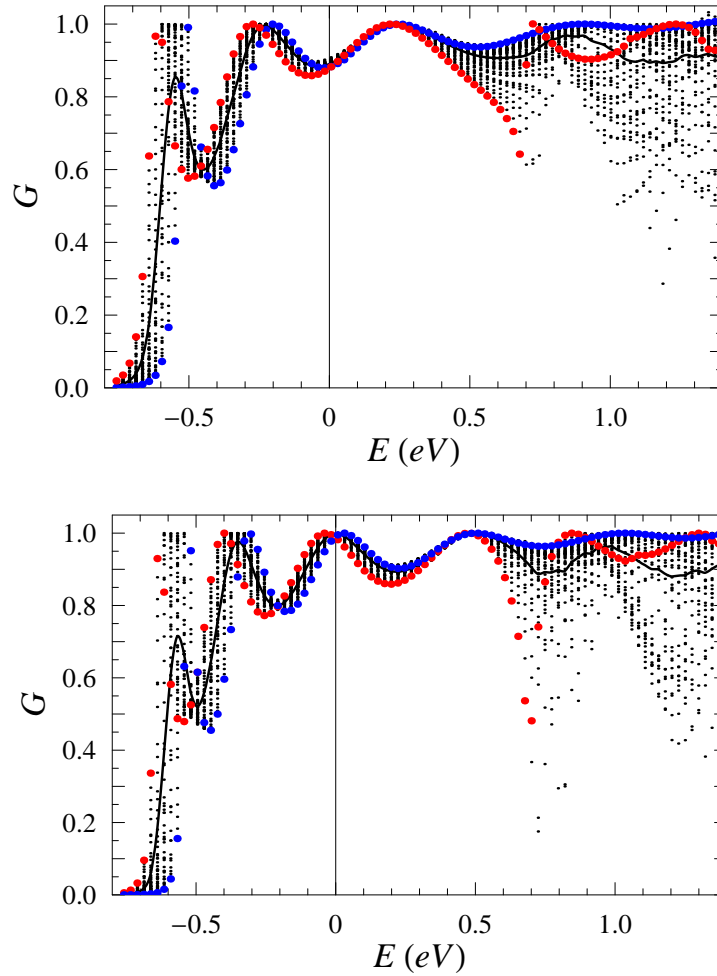


**Figure C.1** : Conductance (in units of  $G_0$ ) as a function of energy for four (top) and five (bottom) atomic wires. The dots correspond to the conductance for various  $\mathbf{k}_{\parallel}$ -points of a  $20 \times 20$  grid in the BZ (55  $\mathbf{k}_{\parallel}$ -points in the irreducible BZ). The thick line is the averaged conductance. The red (light grey) and blue (dark grey) dots correspond to  $\mathbf{k}_{\parallel} = (0, 0)$  and  $(0.5, 0.5)$ , respectively.

---

such calculations require an integration over a wide energy range. The large dispersion at higher energies is related to an increased number of van Hove singularities in the leads [222]. This suggests that  $\mathbf{k}_{\parallel}$ -point sampling can be important for leads containing atoms with a valency higher than one [222], because the number of van Hove singularities is then usually also higher due to more complicated band structure.



# Bibliography

- [1] A. A. Abrikosov, L. P. Gorkov, and I. E. Dzyaloshinski, *Methods of Quantum Field Theory in Statistical Physics* (Dover, New York, 1963).
- [2] E. M. Lifshits and L. P. Pitaevskii, *Statistical Physics*, Course of Theoretical Physics Vol. 9, 3 ed. (Pergamon Press, 1980).
- [3] G. D. Mahan, *Many Particle Physics* (Plenum Press, New York, 1990).
- [4] A. L. Fetter and J. D. Walecka, *Quantum Theory of Many Particle Systems* (McGraw-Hill, Boston, 1971).
- [5] D. Pines, *Elementary Excitations in Solids* (W. A. Benjamin, INC., New York - Amsterdam, 1963).
- [6] L. Hedin, Phys. Rev. **139**, A796 (1965).
- [7] P. van Gelderen, P. A. Bobbert, P. J. Kelly, and G. Brocks, Phys. Rev. Lett. **85**, 2989 (2000).
- [8] G. Onida, L. Reining, and A. Rubio, Rev. Mod. Phys. **74**, 601 (2002).
- [9] N. E. Dahlen, R. van Leeuwen, and U. von Barth, Phys. Rev. A **73**, 012511 (2006).
- [10] G. Senatore and N. H. March, Rev. Mod. Phys. **66**, 445 (1994).
- [11] I. D. Feranchuk, L. I. Komarov, I. V. Nichipor, and A. P. Ulyanenko, Ann. Phys. **238**, 370 (1995).
- [12] J. C. Slater, Phys. Rev. **38**, 1109 (1931).
- [13] C. D. Sherrill and H. F. Schaefer, Adv. Quant. Chem. **34**, 143 (1999).
- [14] R. Shankar, Rev. Mod. Phys. **66**, 129 (1994).
- [15] W. M. C. Foulkes, L. Mitas, R. J. Needs, and G. Rajagopal, Rev. Mod. Phys. **73**, 33 (2001).
- [16] P. Hohenberg and W. Kohn, Phys. Rev. **136**, B864 (1964).

- 
- [17] W. Kohn and L. J. Sham, Phys. Rev. **140**, A1133 (1965).
- [18] R. O. Jones and O. Gunnarsson, Rev. Mod. Phys. **61**, 689 (1989).
- [19] J. P. Perdew and A. Zunger, Phys. Rev. B **23**, 5048 (1981).
- [20] K. Burke, J. Werschnik, and E. K. U. Gross, J. Chem. Phys. **123**, 062206 (2005).
- [21] R. Car and M. Parrinello, Phys. Rev. Lett. **55**, 2471 (1985).
- [22] E. Fermi, Z. Phys. **48**, 73 (1928).
- [23] C. Kittel, *Quantum Theory of Solids* (John Wiley and Sons, Inc., New York, 1963).
- [24] L. D. Landau and E. M. Lifschitz, *Quantum Mechanics: Non-relativistic Theory* (Pergamon Press, Oxford, 1981).
- [25] E. H. Lieb and B. Simon, Phys. Rev. Lett. **31**, 681 (1973).
- [26] D. M. Ceperley and B. J. Alder, Phys. Rev. Lett. **45**, 566 (1980).
- [27] P. A. M. Dirac, Proc. Royal Soc. (London) A **123**, 714 (1929).
- [28] E. P. Wigner, Phys. Rev. **46**, 1006 (1934).
- [29] J. P. Perdew *et al.*, Phys. Rev. B **46**, 6671 (1993).
- [30] M. C. Payne, M. P. Teter, D. C. Allan, T. A. Arias, and J. D. Joannopoulos, Rev. Mod. Phys. **64**, 1045 (1992).
- [31] J. Ihm, A. Zunger, and M. L. Cohen, J. Phys. C: Sol. State Phys. **12**, 4409 (1979).
- [32] D. Singh, *Plane waves, pseudopotentials and the LAPW method* (Kluwer Academic, 1994).
- [33] P. Ordejón, E. Artacho, and J. M. Soler, Phys. Rev. B **53**, R10441 (1996).
- [34] O. K. Andersen and O. Jepsen, Phys. Rev. Lett. **53**, 2571 (1984).
- [35] O. K. Andersen *et al.*, in, in *Electronic Structure and Physical Properties of Solids: The Uses of the LMTO Method*, edited by H. Dreyse, pp. 3–84, Springer Lecture Notes in Physics, New York, 2000.
- [36] T. L. Beck, Rev. Mod. Phys. **72**, 1041 (2000).
- [37] J. R. Chelikowsky, N. Troullier, and Y. Saad, Phys. Rev. Lett. **72**, 1240 (1994).
- [38] T. Ono and K. Hirose, Phys. Rev. B **82**, 5016 (1999).
- [39] T. Torsti *et al.*, Phys. Stat. Sol. B (2006), cond-mat/0601201.

- 
- [40] J. Ihm, A. Zunger, and M. L. Cohen, *J. Phys. C: Sol. State Phys.* **13**, 3095 (1980).
- [41] J. C. Phillips and L. Kleinman, *Phys. Rev.* **116**, 287 (1959).
- [42] L. Kleinman and D. M. Bylander, *Phys. Rev. Lett.* **48**, 1425 (1982).
- [43] D. R. Hamann, M. Schluter, and C. Chiang, *Phys. Rev. Lett.* **43**, 1494 (1979).
- [44] D. R. H. G. B. Bachelet and M. Schlüter, *Phys. Rev. B* **26**, 4199 (1982).
- [45] N. Troullier and J. L. Martins, *Phys. Rev. B* **43**, 1993 (1991).
- [46] D. Vanderbilt, *Phys. Rev. B* **41**, 7892 (1990).
- [47] K. Laasonen, A. Pasquarello, R. Car, C. Lee, and D. Vanderbilt, *Phys. Rev. B* **47**, 10142 (1993).
- [48] P. E. Blöchl, *Phys. Rev. B* **50**, 17953 (1994).
- [49] G. Kresse and D. Joubert, *Phys. Rev. B* **59**, 1758 (1999).
- [50] D. M. Wood and A. Zunger, *J. Phys. A: Math. Gen.* **18**, 1343 (1985).
- [51] S. Kirkpatrick, J. G. D. Gelatt, and M. P. Vecchi, *Science* **220**, 671 (1983).
- [52] A. Williams and J. Soler, *Phys. Rev. B* **32**, 562 (1987).
- [53] W. M. Press, B. P. Flannery, S. A. Teukolsky, and W. T. Vetterling, *Numerical Recipes* (Cambridge University Press, Cambridge, 1986), p. 301.
- [54] I. Štich, R. Car, M. Parrinello, and S. Baroni, *Phys. Rev. B* **39**, 4997 (1989).
- [55] J. Neugebauer and M. Scheffler, *Phys. Rev. B* **46**, 16067 (1992).
- [56] J. R. Chelikowsky, N. Troullier, K. Wu, and Y. Saad, *Phys. Rev. B* **50**, 11355 (1994).
- [57] Y. Saad, *Iterative Methods for Sparse Linear Systems*, 2 ed. (SIAM, Philadelphia, PA, 2003).
- [58] M. M. G. Alemany, M. Jain, L. Kronik, and J. R. Chelikowsky, *Phys. Rev. B* **69**, 075101 (2004).
- [59] T. Ono and K. Hirose, *Phys. Rev. B* **72**, 085115 (2005).
- [60] B. J. van Wees *et al.*, *Phys. Rev. Lett.* **60**, 848 (1988).
- [61] N. Agraït, A. L. Yeyati, and J. M. van Ruitenbeek, *Phys. Rep.* **377**, 81 (2003).
- [62] S. Datta, *Electronic Transport in Mesoscopic Systems* (Cambridge University Press, Cambridge, 1995).

- 
- [63] R. Landauer, IBM J. Res. Dev. **1**, 223 (1957).
- [64] R. Landauer, Phil. Mag. **21**, 863 (1970).
- [65] D. S. Fisher and P. A. Lee, Phys. Rev. B **23**, 6851 (1981).
- [66] E. N. Economou and C. M. Soukoulis, Phys. Rev. Lett. **46**, 618 (1981).
- [67] M. Büttiker, Y. Imry, R. Landauer, and S. Pinhas, Phys. Rev. B **31**, 6207 (1985).
- [68] M. Büttiker, Phys. Rev. Lett. **57**, 1761 (1986).
- [69] A. D. Stone and A. Szafer, IBM J. Res. Dev. **32**, 384 (1988).
- [70] P. A. Khomyakov and G. Brocks, Phys. Rev. B **70**, 195402 (2004).
- [71] P. A. Khomyakov, G. Brocks, V. Karpan, M. Zwierzycki, and P. J. Kelly, Phys. Rev. B **72**, 035450 (2005).
- [72] L. P. Kadanoff and G. Baym, *Quantum Statistical Mechanics* (Benjamin, New York, 1962).
- [73] L. V. Keldysh, Sov. Phys. JETP **20**, 1018 (1965), [Zh. Eksp. Teor. Fiz. **47**, 1515 (1964)].
- [74] J. Rammer and H. Smith, Rev. Mod. Phys. **58**, 323 (1986).
- [75] C. Caroli, R. Combescot, P. Nozières, and D. Saint-James, J. Phys. C: Sol. State Phys. **4**, 916 (1971).
- [76] Y. Meir and N. S. Wingreen, Phys. Rev. Lett. **68**, 2512 (1992).
- [77] N. W. Ashcroft and N. D. Mermin, *Solid State Physics* (Holt, Rinehart and Winston, New York, 1976).
- [78] A. B. Kunz, Phys. Rev. B **12**, 5890 (1975).
- [79] G. Stefanucci and C.-O. Almbladh, Phys. Rev. B **69**, 195318 (2004).
- [80] N. Sai, M. Zwolak, G. Vignale, and M. D. Ventra, Phys. Rev. Lett. **94**, 186810 (2005).
- [81] C. Toher, A. Filippetti, S. Sanvito, and K. Burke, Phys. Rev. Lett. **95**, 146402 (2005).
- [82] R. H. M. Smit, C. Untiedt, G. Rubio-Bollinger, R. C. Segers, and J. M. van Ruitenbeek, Phys. Rev. Lett. **91**, 076805 (2003).
- [83] Y. Xue, S. Datta, and M. A. Ratner, J. Chem. Phys. **115**, 4292 (2001).
- [84] M. Brandbyge, J. L. Mozos, P. Ordejón, J. Taylor, and K. Stokbro, Phys. Rev. B **65**, 165401 (2002).



- 
- [85] A. Pecchia and A. D. Carlo, Rep. Prog. Phys. **67**, 1497 (2004).
- [86] Y.-C. Chen and M. D. Ventra, **95**, 166802 (2005).
- [87] T. Frederiksen, M. Brandbyge, N. Lorente, and A.-P. Jauho, Phys. Rev. Lett. **93**, 256601 (2004).
- [88] M. Paulsson, T. Frederiksen, and M. Brandbyge, Phys. Rev. B **72**, 201101 (2005).
- [89] P. Delaney and J. C. Greer, Phys. Rev. Lett. **93**, 036805 (2004).
- [90] M. N. Baibich *et al.*, Phys. Rev. Lett. **61**, 2472 (1988).
- [91] G. Binasch, P. Grünberg, F. Saurenbach, and W. Zinn, Phys. Rev. B **39**, 4828 (1989).
- [92] K. M. Schep, J. B. A. N. van Hoof, P. J. Kelly, G. E. W. Bauer, and J. E. Inglesfield, Phys. Rev. B **56**, 10805 (1997).
- [93] J. B. A. N. van Hoof, K. M. Schep, A. Brataas, G. E. W. Bauer, and P. J. Kelly, Phys. Rev. B **59**, 138 (1999).
- [94] J. Kudrnovský *et al.*, Phys. Rev. B **62**, 15084 (2000).
- [95] K. Xia *et al.*, Phys. Rev. B **63**, 064407 (2001).
- [96] I. Riedel, P. Zahn, and I. Mertig, Phys. Rev. B **63**, 195403 (2001).
- [97] J. Taylor, H. Guo, and J. Wang, Phys. Rev. B **63**, 245407 (2001).
- [98] D. Wortmann, H. Ishida, and S. Blügel, Phys. Rev. B **66**, 075113 (2002).
- [99] K. S. Thygesen, M. V. Bollinger, and K. W. Jacobsen, Phys. Rev. B **67**, 115404 (2003).
- [100] P. Mavropoulos, N. Papanikolaou, and P. Dederichs, Phys. Rev. B **69**, 125104 (2004).
- [101] T. Ando, Phys. Rev. B **44**, 8017 (1991).
- [102] K. Nicolíć and A. MacKinnon, Phys. Rev. B **50**, 11008 (1994).
- [103] K. Xia, P. J. Kelly, G. E. W. Bauer, A. Brataas, and I. Turek, Phys. Rev. B **65**, 220401 (2002).
- [104] K. Xia, P. J. Kelly, G. E. W. Bauer, and I. Turek, Phys. Rev. Lett. **89**, 166603 (2002).
- [105] M. Zwierzycki, K. Xia, P. J. Kelly, and G. E. W. Bauer, Phys. Rev. B **67**, 092401 (2003).

- 
- [106] P. S. Krstić, X.-G. Zhang, and W. H. Butler, *Phys. Rev. B* **66**, 205319 (2002).
- [107] P. Sautet and C. Joachim, *Phys. Rev. B* **38**, 12238 (1988).
- [108] K. Xia, M. Zwierzycki, M. Talanana, P. J. Kelly, and G. E. W. Bauer, *Phys. Rev. B* **73**, 064420 (2006).
- [109] A. MacKinnon, *Z. Phys. B* **59**, 385 (1985).
- [110] G. Golub and C. F. van Loan, *Matrix Computations* (Johns Hopkins University Press, Baltimore, 1996).
- [111] F. Tisseur and K. Meerbergen, *SIAM Review* **43**, 235 (2001).
- [112] L. Molinari, *J. Phys. A: Math. Gen.* **30**, 983 (1997).
- [113] E. Godfrin, *J. Phys.: Condens. Matter.* **3**, 7843 (1991).
- [114] A. R. Williams, P. J. Feibelman, and N. D. Lang, *Phys. Rev. B* **26**, 5433 (1982).
- [115] I. Turek, V. Drchal, J. Kudrnovský, M. Šob, and P. Weinberger, *Electronic Structure of Disordered Alloys, Surfaces and Interfaces* (Kluwer, Boston-London-Dordrecht, 1997).
- [116] F. Guinea, C. Tejedor, F. Flores, and E. Louis, *Phys. Rev. B* **28**, 4397 (1983).
- [117] A. Messiah, *Quantum Mechanics* (North-Holland, Amsterdam, 1961).
- [118] S. Sanvito, C. J. Lambert, J. Jefferson, and A. M. Bratkovsky, *Phys. Rev. B* **59**, 11936 (1999).
- [119] A. Umerski, *Phys. Rev. B* **55**, 5266 (1997).
- [120] P. A. Khomyakov, (unpublished).
- [121] T. Kostyrko, *Phys. Rev. B* **62**, 2458 (2000).
- [122] H. U. Baranger and A. D. Stone, *Phys. Rev. B* **40**, 8169 (1989).
- [123] O. K. Andersen, O. Jepsen, and D. Glötzel, in, in *Highlights of Condensed Matter Theory*, edited by F. Bassani, F. Fumi, and M. P. Tosi, pp. 59–176, North-Holland, Amsterdam, 1985.
- [124] C. S. Wang and A. J. Freeman, *Phys. Rev. B* **24**, 4364 (1981).
- [125] J. A. Stroschio, D. T. Pierce, A. Davies, R. J. Celotta, and M. Weinert, *Phys. Rev. Lett.* **75**, 2960 (1995).
- [126] C. Uiberacker and P. M. Levy, *Phys. Rev. B* **64**, 193404 (2001).
- [127] C. Uiberacker and P. M. Levy, *Phys. Rev. B* **65**, 169904(E) (2002).

- 
- [128] O. Wunnicke *et al.*, Phys. Rev. B **65**, 064425 (2002).
- [129] W. H. Butler, X.-G. Zhang, T. C. Schulthess, and J. M. MacLaren, Phys. Rev. B **63**, 054416 (2001).
- [130] J. Mathon and A. Umerski, Phys. Rev. B **63**, 220403(R) (2001).
- [131] T. N. Todorov, G. A. D. Briggs, and A. P. Sutton, J. Phys.: Condens. Matter. **5**, 2389 (1993).
- [132] M. P. Samanta, W. Tian, S. Datta, J. I. Henderson, and C. P. Kubiak, Phys. Rev. B **53**, R7626 (1996).
- [133] E. G. Emberly and G. Kirczenow, Phys. Rev. B **58**, 10911 (1998).
- [134] K. Hirose and M. Tsukada, Phys. Rev. B **51**, 5278 (1995).
- [135] K. Hirose and M. Tsukada, Phys. Rev. B **51**, 5278 (1995).
- [136] N. D. Lang, Phys. Rev. B **52**, 5335 (1995).
- [137] N. D. Lang, Phys. Rev. Lett. **79**, 1357 (1997).
- [138] M. D. Ventra, S. T. Pantelides, and N. D. Lang, Phys. Rev. Lett. **84**, 979 (2000).
- [139] H. J. Choi and J. Ihm, Phys. Rev. B **59**, 2267 (1999).
- [140] Y. G. Yoon, M. S. C. Mazzoni, H. J. Choi, J. Ihm, and S. G. Louie, Phys. Rev. Lett. **86**, 688 (2001).
- [141] P. S. Damle, A. W. Ghosh, and S. Datta, Phys. Rev. B **64**, 201403 (2001).
- [142] M. B. Nardelli, J.-L. Fattebert, and J. Bernholc, Phys. Rev. B **64**, 245423 (2001).
- [143] J. J. Palacios, A. J. Pérez-Jiménez, E. Louis, E. SanFabián, and J. A. Vergés, Phys. Rev. B **66**, 035322 (2002).
- [144] J. Heurich, J. C. Cuevas, W. Wenzel, and G. Schön, Phys. Rev. Lett. **88**, 256803 (2002).
- [145] J. P. Vigneron and P. Lambin, J. Phys. A: Math. Gen. **12**, 1961 (1979).
- [146] J. P. Vigneron and P. Lambin, J. Phys. A: Math. Gen. **13**, 1135 (1980).
- [147] C. Berthod, F. Gagel, and K. Maschke, Phys. Rev. B **50**, 18299 (1994).
- [148] F. Gagel and K. Maschke, Phys. Rev. B **52**, 2013 (1994).
- [149] Y. Fujimoto and K. Hirose, Phys. Rev. B **67**, 195315 (2003).

- 
- [150] A. A. Starikov, I. I. Yakimenko, and K.-F. Berggren, *Phys. Rev. B* **67**, 235319 (2003).
- [151] F. Gygi and G. Galli, *Phys. Rev. B* **52**, R2229 (1995).
- [152] H.-O. Kreiss, *Math. Comp.* **26**, 605 (1972).
- [153] H. Brandén, Dept. of Information Technology, Uppsala Univ. Report No. 2000-026, 2000 (unpublished).
- [154] M. Abramowitz and I. A. Stegun, *Handbook of Mathematical Functions* (Dover, New York, 1965).
- [155] S. Wolfram, Mathematica, <http://documents.wolfram.com>.
- [156] C. S. Barrett, *Acta Crystallogr.* **9**, 671 (1956).
- [157] A. A. Quong *et al.*, *Phys. Rev. Lett.* **66**, 743 (1991).
- [158] N. Kobayashi, M. Brandbyge, and M. Tsukada, *Phys. Rev. B* **62**, 8430 (2000).
- [159] N. J. Fall, N. Binggeli, and A. Baldereschi, *J. Phys.: Condens. Matter.* **11**, 2689 (1999).
- [160] A. L. Yeyati, A. Martín-Rodero, and F. Flores, *Phys. Rev. B* **56**, 10369 (1997).
- [161] H.-S. Sim, H.-W. Lee, and K. J. Chang, *Phys. Rev. Lett.* **87**, 096803 (2001).
- [162] P. Havu, T. Torsti, M. J. Puska, and R. M. Nieminen, *Phys. Rev. B* **66**, 075401 (2002).
- [163] S. Tsukamoto and K. Hirose, *Phys. Rev. B* **66**, 161402 (2002).
- [164] Y. J. Lee *et al.*, *Phys. Rev. B* **69**, 125409 (2004).
- [165] K. S. Thygesen and K. W. Jacobsen, *Phys. Rev. Lett.* **91**, 146801 (2003).
- [166] A. I. Yanson, G. Rubio-Bollinger, H. E. van den Brom, N. Agrait, and J. M. Ruitenbeek, *Nature* **395**, 783 (1998).
- [167] H. Ohnishi, Y. Kondo, and K. Takayanagi, *Nature* **395**, 780 (1998).
- [168] J. M. Krans, J. M. van Ruitenbeek, V. V. Fisun, I. K. Yanson, and L. J. Jongh, *Nature* **375**, 767 (1995).
- [169] G. Rubio, N. Agrait, and S. Viera, *Phys. Rev. Lett.* **76**, 2302 (1996).
- [170] A. Yazdani, D. M. Eigler, and N. D. Lang, *Science* **272**, 1921 (1996).
- [171] A. I. Yanson, I. K. Yanson, and J. M. van Ruitenbeek, *Nature* **400**, 144 (1999).
- [172] R. H. M. Smit, C. Untiedt, A. I. Yanson, and J. M. van Ruitenbeek, *Phys. Rev. Lett.* **87**, 266102 (2001).

- 
- [173] S. K. Nielson *et al.*, Phys. Rev. Lett. **89**, 066804 (2002).
- [174] V. Rodrigues, T. Fuhrer, and D. Ugarte, Phys. Rev. Lett. **85**, 4124 (2000).
- [175] V. Rodrigues, J. Bettini, A. R. Rocha, L. G. C. Rego, and D. Ugarte, Phys. Rev. B **65**, 153402 (2002).
- [176] S. Csonka *et al.*, Phys. Rev. Lett. **90**, 116803 (2003).
- [177] A. I. Mares and J. M. van Ruitenbeek, Phys. Rev. B **72**, 205402 (2005).
- [178] A. Fujii, M. Tsutsui, S. Kurokawa, and A. Sakai, Phys. Rev. B **72**, 045407 (2005).
- [179] C. A. Stafford, D. Baeriswyl, and J. Bürki, Phys. Rev. Lett. **79**, 2863 (1997).
- [180] U. F. Urban *et al.*, Sol. State Comm. **131**, 609 (2004).
- [181] A. Smogunov, A. D. Corso, and E. Tosatti, Phys. Rev. B **70**, 045417 (2004).
- [182] A. Bagrets, N. Papanikolaou, and I. Mertig, Phys. Rev. B **70**, 064410 (2004).
- [183] S. V. Faleev, F. Léonard, D. A. Stewart, and M. van Schilfhaarde, Phys. Rev. B **71**, 195422 (2005).
- [184] P. Havu *et al.*, J. Chem. Phys. **124**, 054707 (2006).
- [185] Z. Li and D. S. Kosov, J. Phys.: Condens. Matter. **18**, 1347 (2006).
- [186] A. R. Rocha, V. M. García-Suárez, S. Bailey, C. L. J. Ferrer, and S. Sanvito, Phys. Rev. B **73**, 085414 (2006).
- [187] M. R. Sørensen, M. Brandbyge, and K. W. Jacobsen, Phys. Rev. B **57**, 3283 (1998).
- [188] E. Z. da Silva, A. J. R. da Silva, and A. Fazzio, Phys. Rev. Lett. **87**, 256102 (2001).
- [189] M. Dreher *et al.*, Phys. Rev. B **72**, 075435 (2005).
- [190] R. N. Barnett and U. Landman, Nature **387**, 788 (1997).
- [191] D. Sánchez-Portal *et al.*, Phys. Rev. Lett. **83**, 3884 (1999).
- [192] M. Okamoto and K. Takayanagi, Phys. Rev. B **60**, 7808 (1999).
- [193] H. Häkkinen, R. N. Barnett, A. G. Scherbakov, and U. Landman, J. Phys. Chem. **104**, 9063 (2000).
- [194] G. Rubio-Bollinger, S. R. Bahn, N. Agraït, K. W. Jacobsen, and S. Vieira, Phys. Rev. Lett. **87**, 026101 (2001).
- [195] L. D. Maria and M. Springborg, Chem. Phys. Lett. **323**, 293 (2000).

- [196] S. R. Bahn and K. W. Jacobsen, Phys. Rev. Lett. **87**, 266101 (2001).
- [197] E. Tosatti, S. Prestipino, S. Kostlmeier, A. D. Corso, and F. D. D. Tolla, Science **291**, 288 (2001).
- [198] D. Sánchez-Portal, E. Artacho, A. G. J. Junquera, and J. M. Soler, Surf. Sci. **482-485**, 1261 (2001).
- [199] P. Sen, S. Ciraci, A. Buldum, and I. P. Batra, Phys. Rev. B **64**, 195420 (2001).
- [200] M. Springborg and P. Sarkar, Phys. Rev. B **68**, 045430 (2003).
- [201] T. Ono and K. Hirose, Phys. Rev. B **68**, 045409 (2003).
- [202] E. Z. da Silva, F. D. Novaes, A. J. R. da Silva, and A. Fazzio, Phys. Rev. B **69**, 115411 (2004).
- [203] A. M. Asaduzzaman and M. Springborg, Phys. Rev. B **72**, 165422 (2005).
- [204] H.-W. Lee and C. S. Kim, Phys. Rev. B **63**, 075306 (2001).
- [205] Z. Y. Zeng and F. Claro, Phys. Rev. B **65**, 193405 (2002).
- [206] W. H. A. Thijssen, D. Marjenburgh, R. H. Bremmer, and J. M. van Ruitenbeek, Phys. Rev. Lett. **96**, 026806 (2006).
- [207] Y. Egami, T. Ono, and K. Hirose, Phys. Rev. B **72**, 125318 (2005).
- [208] R. Gutiérrez, F. Grossmann, and R. Schmidt, Acta Phys. Pol. B **32**, 443 (2001).
- [209] J. K. Viljas, J. C. Cuevas, F. Pauly, and M. Häfner, Phys. Rev. B **72**, 245415 (2005).
- [210] P. Major *et al.*, Phys. Rev. B **73**, 045421 (2006).
- [211] G. Kresse and J. Furthmüller, Phys. Rev. B **54**, 11169 (1996).
- [212] G. Kresse and J. Furthmüller, Comput. Mater. Sci. **6**, 15 (1996).
- [213] G. Kresse and J. Hafner, Phys. Rev. B **47**, 558 (1993).
- [214] J. P. Perdew *et al.*, Phys. Rev. B **48**, 4978 (1993).
- [215] R. N. G. Wychoff, *Crystal Structures* (Wiley, New York, 1964).
- [216] P. Calaminici, K. Jug, and A. M. Koster, J. Chem. Phys. **111**, 4613 (1999).
- [217] K. P. Huber and G. Herzberg, *Molecular Spectra and Molecular Structure*, Constants of Diatomic Molecules Vol. 4 (PrenticeHall, New York, 1979), p. 432.
- [218] A. Bergara, J. B. Neaton, and N. W. Ashcroft, Int. J. Quant. Chem. **91**, 239 (2003).

- [219] A. Delin and E. Tosatti, *Phys. Rev. B* **68**, 144434 (2003).
- [220] C. Untiedt, D. M. T. Dekker, D. Djukic, and J. M. van Ruitenbeek, *Phys. Rev. B* **69**, 081401 (2004).
- [221] Y. Egami, T. Sasaki, T. Ono, and K. Hirose, *Nanotechnology* **16**, S161 (2005).
- [222] K. S. Thygesen and K. W. Jacobsen, *Phys. Rev. B* **72**, 033401 (2005).





# Summary

Nanoelectronics is a fast developing field. Therefore understanding of the electronic transport at the nanoscale is currently of great interest. This thesis "*Electronic transport through nanowires: a real-space finite-difference approach*" aims at a general theoretical treatment of coherent electronic transport in mesoscopic and microscopic systems by means of Green's function and mode-matching techniques. A general method has been developed for conductance calculations on the basis of the mode-matching technique within the real-space high-order finite-difference scheme for representing a single electron equation. Testing of this real-space finite-difference approach for model systems has been done. This approach in combination with the density-functional formalism has been applied to the conductance calculations in nanowires. The stability of even-odd conductance oscillations in monatomic sodium wires with respect to structural variations has been investigated.

In **Chapter 1** we give a general introduction on the electronic structure and conductance calculation methods for atomic-sized conductors. The basic concepts of density functional theory that is used in this thesis for calculating the electronic structure of atomic-sized conductors, are presented. We discuss all approximations used to simplify density functional theory. In particular, we focus on the local density approximation for the exchange-correlation energy functional. Two implementations of the pseudopotential method, based on either the plane-wave or the finite-difference representation of the Kohn-Sham equation are described. In this thesis the plane-wave representation is used for solving the Kohn-Sham equation to calculate the one-electron potential, and the finite-difference representation is exploited for solving a scattering problem in this potential. To relate the scattering problem to the conductance calculations we make use of the Landauer-Büttiker formalism throughout the thesis. Therefore, a brief overview of this formalism is given in this introductory chapter. The approximations that are usually made in first-principles conductance calculations for atomic-sized conductors, are debated in detail. We mainly discuss the Hartree-Fock approximation and static density functional theory within the local density approximation.

In **Chapter 2** we discuss the relationship between two techniques for calculating the conductance of nanowires or interfaces. The first technique is based on the Landauer-Büttiker formalism and the mode matching scheme for calculating partial transmission probabilities that can be related to the conductance via Landauer's for-

mula. The partial transmission probabilities can be calculated from the scattering wave functions that are obtained by matching the wave functions in the conductor to the modes of ideal bulk leads. In this thesis an elegant mode-matching technique formulated by Ando is generalized to any Hamiltonian that can be represented in tight-binding form. The second technique considered is based on the Keldysh formalism and Caroli's formula that expresses the conductance in terms of the Green functions. We show how all the Green function results can be derived from the mode matching technique, and derive a compact expression for the transmission matrix elements. We also illustrate the relationship between the Green function and mode-matching techniques for an analytically solvable tight-binding model and for an Fe|vacuum|Fe tunnel junction which is studied numerically using first-principles calculations.

In **Chapter 3** we develop a general method for calculating coherent electronic transport in nanowires and tunnel junctions. This method is based upon a real-space high-order finite-difference representation of the single particle Hamiltonian and wave functions. In this case the single particle equation can be represented in tight-binding form. We use Landauer's formula to express the conductance as a scattering problem, and solve this problem by the mode-matching technique that is developed in Chapter 2. The real-space finite-difference method is tested on model tunnel junctions and applied to sodium atomic wires. In particular, we show that using a high-order finite-difference approximation of the kinetic energy operator provides a high accuracy at moderate computational costs. All computational details of the method are given in this chapter.

In **Chapter 4** we study the stability of conductance oscillations in monatomic sodium wires with respect to structural variations. We perform self-consistent density functional theory calculations to obtain the geometry, the electronic structure and the electronic potential of wires suspended between two sodium electrodes. The electronic transport is calculated within the real-space finite-difference approach as formulated in Chapter 3. We find a regular even-odd conductance oscillation as a function of the number of atoms in the wire. The odd-numbered wires have a conductance close to the quantum unit, and even-numbered wires have a lower conductance. Moreover, the conductance of odd-numbered wires is stable with respect to geometry changes in the wire or in the contacts between the wire and the electrodes. We show that the conductance of even-numbered wires is more sensitive to these structural variations. This difference between the odd and even-numbered wires is explained in terms of on/off-resonance behavior of the transmission. In case of odd numbered wires the transmission is on-resonance, and it is not sensitive to the resonance shapes or the energy level spacings in the wire. For even-numbered wires the transmission is off-resonance, and it is strongly affected by the resonance shapes and the energy level spacings. If the charge neutrality of the wire is maintained then the phase of the conductance oscillation can be obtained from simple model calculations, but predicting its magnitude requires a self-consistent first-principles calculation for a realistic structure of the wire and the leads. We introduce a simple tight-binding model to clarify these first-principles results. This model allows us for an analytical study of the problem. We demonstrate that the charge neutrality of the wire imposes a strong

constraint on the phase of the conductance oscillation. The actual effect of a charge transfer between the wire and the electrodes can not be predicted from a simple tight-binding model. Therefore, the first-principles calculations are needed to obtain the one-electron potential. We find that the conductance is rather sensitive to the quality of this potential, which has to be properly converged. Summarizing all the results obtained we show that the phase of the even-odd conductance oscillation is stable with respect to structural variations, indicating that the charge transfer is not significant to change the phase of conductance oscillations in all the cases considered. Therefore, we suggest that the controversial results that are reported on the phase of the conductance oscillation in the literature, originate from spurious charge transfer between the wire and the electrodes.



# Samenvatting

Nanoëlectronica is een zich snel ontwikkelend veld en elektronisch transport op nanoschaal trekt momenteel een grote belangstelling. Dit proefschrift, getiteld: *“Electronisch transport door nanodraden: een reële ruimte eindige verschillen benadering”*, beoogt een algemene theoretische beschrijving te geven van coherent elektronisch transport in microscopische systemen met behulp van Greense functie en “mode matching” technieken. Gebruik makend van mode matching wordt een methode ontwikkeld voor de berekening van de geleiding, welke gebaseerd is op een reële ruimte, hogere orde eindige verschillen representatie van een één-deeltjes vergelijking. Deze methode wordt getest op model systemen en, in combinatie met het dichtheidsfunctionaalformalisme, toegepast om de geleiding van nanodraden te berekenen. De stabiliteit van de even/oneven oscillatie van de geleiding in natrium nanodraden wordt onderzocht met betrekking tot structurele variaties.

In **hoofdstuk 1** wordt een algemene inleiding gegeven over de elektronenstructuur en de geleiding van atomaire geleiders. In dit proefschrift wordt dichtheidsfunctionaaltheorie gebruikt om de elektronenstructuur van atomaire geleiders te beschrijven. De basisconcepten van dichtheidsfunctionaaltheorie worden besproken, alsmede de veelvuldig toegepaste benaderingen in deze theorie, zoals de locale dichtheidsbenadering voor de verwisselcorrelatiefunctie. Twee implementaties van de pseudopotentiaalaanpak worden besproken, die respectievelijk gebaseerd zijn op een vlakke golven representatie en een eindige verschillen representatie van de Kohn-Sham vergelijking. In dit proefschrift wordt de vlakke golven representatie gebruikt om de Kohn-Sham vergelijking zelfconsistent op te lossen en de één-deeltjes potentiaal te genereren. De eindige verschillen representatie wordt toegepast om vervolgens het strooi probleem in deze potentiaal op te lossen. Het Landauer-Büttiker formalisme wordt gebruikt om het strooi probleem te relateren aan de geleiding. Een kort overzicht wordt gegeven van dit formalisme, alsmede van de doorgaans gebruikte benaderingen in de toepassing ervan op geleidingsberekeningen van atomaire geleiders, zoals de Hartree-Fock benadering of de locale dichtheidsbenadering in de context van statische dichtheidsfunctionaaltheorie.

**Hoofdstuk 2** behandelt de relatie tussen twee technieken om de geleiding van nanodraden en grensvlakken te berekenen. De eerste techniek is gebaseerd op het Landauer-Büttiker formalisme en het mode matching schema om transmissiewaarschijnlijkheidsamplitudes te berekenen, die via Landauer’s formule aan de geleiding gere-

lateerd kunnen worden. De transmissiewaarschijnlijkheidsamplitudes worden berekend door de golffunctie in het strooigebied te matchen aan de modes in de ideale bulk aanvoerdraden. In dit proefschrift wordt de mode matching methode zoals geformuleerd door Ando, gegeneraliseerd voor een iedere Hamiltoniaan die gerepresenteerd kan worden door een tight-binding vorm. De tweede techniek is gebaseerd op het Keldysh formalisme en maakt gebruik van Caroli's formules om de geleiding uit te drukken in Greense functies. We laten zien hoe de resultaten van dit Greense functie formalisme kunnen worden afgeleid uit de mode matching aanpak, en leiden een compacte uitdrukking af voor de elementen van de transmissiematrix. De relatie tussen de Greense functie en de mode matching technieken wordt geïllustreerd aan een analytisch oplosbaar model en aan een ijzer-vacuüm-ijzer tunneljunctie. Deze laatste wordt numeriek onderzocht met behulp van "first-principles" berekeningen.

In **hoofdstuk 3** wordt een praktische methode ontwikkeld om coherent elektronisch transport in nanodraden en tunneljuncties te berekenen. Deze methode is gebaseerd op een reële ruimte eindige verschillen representatie van de één-deeltjes Hamiltoniaan en golffuncties. De bijbehorende één-deeltjes vergelijking krijgt dan een tight-binding vorm. Landauer's formules worden gebruikt om de geleiding uit te drukken als een strooioprobleem, wat wordt opgelost met behulp van de mode matching techniek ontwikkeld in het vorige hoofdstuk. De methode wordt getest op model tunneljuncties en toegepast op natrium nanodraden. In het bijzonder wordt aangetoond dat het gebruik van een hogere orde eindige verschillen benadering van de kinetische energie operator gepaard gaat met een hoge nauwkeurigheid en gematigde rekenkosten. De technische details van deze rekenmethode worden behandeld in dit hoofdstuk.

De stabiliteit van geleidingsoscillaties in mono-atomaire natrium draden ten opzichte van structurele variaties wordt bestudeerd in **hoofdstuk 4**. Zelfconsistente dichtheidsfunctionaalberekeningen geven de geometrie, de elektronenstructuur en de potentiaal voor de elektronen van draden die tussen twee natriumelectrodes gespannen zijn. Het elektronisch transport wordt berekend met de methode zoals ontwikkeld in het vorige hoofdstuk. We vinden een regelmatige even/oneven oscillatie in de geleiding als functie van het aantal atomen in de draad. Draden bestaande uit een onveven aantal atomen hebben een geleiding dicht bij de quantumeenheid; draden met een even aantal atomen hebben een significant lagere geleiding. Daarenboven is de geleiding van de "oneven" draden stabiel onder veranderingen in de geometrie van de draden en van de contacten tussen de draden en de elektroden. De geleiding van de "even" draden is daarentegen gevoelig voor zulke structurele veranderingen. Dit verschil tussen even en oneven draden wordt verklaard uit het resonantiegedrag van de transmissie. De transmissie van oneven draden is resonant en dus niet gevoelig voor de lijnvorm van de resonantie, noch voor de afstand tussen de verschillende resonanties. De transmissie van even draden is niet resonant en wel gevoelig voor deze factoren. Het feit dat de draden hebben geen netto lading blijken te hebben, betekent dat de fase van de geleidingsoscillatie al wordt gevonden in simpele modelberekeningen. Om de amplitude van de oscillatie te verkrijgen is echter een nauwkeurige zelfconsistente first-principles berekening vereist voor een realistische structuur van de draad en de elektroden. We introduceren een simpel

analytisch tight-binding model om de first-principles resultaten te verhelderen. Dit model laat zien dat de ladingsneutraliteit van de draad een sterke beperking oplegt aan de fase van de geleidingsoscillatie. De grootte van de ladingsoverdracht tussen de draad en de elektroden kan niet worden afgeleid uit dit simpele model, maar volgt uit de first-principles berekeningen en, meer bepaald, uit de één-deeltjes potentiaal. De geleiding is gevoelig voor veranderingen in deze potentiaal en we stellen vast dat deze goed geconvergeerd moet zijn. Aangezien dat de fase van even/oneven geleidingsoscillatie stabiel is ten opzichte van structurele veranderingen, concluderen we dat de ladingsoverdracht tussen draad en elektrodes nihil is in alle onderzochte gevallen. De verschillen in de fase die gevonden worden in de literatuur suggereren verschillen in de ladingsoverdracht die het gevolg zouden kunnen zijn van niet geconvergeerde berekeningen.





## Заключение

Наноэлектроника - быстро развивающаяся область, поэтому изучение транспорта электрона в проводниках, имеющих размеры порядка нескольких нанометров, представляет огромный интерес. В данной работе *"Транспорт электрона через наноразмерные проводя: конечно-разностный метод в координатном пространстве"* было проведено теоретическое исследование когерентного транспорта электрона в мезоскопических и микроскопических системах, используя метод функций Грина и метод модовой сшивки волновой функции. Был разработан общий подход расчета проводимости, основанный на методе модовой сшивки и конечно-разностной схеме высокого порядка, примененной к одноэлектронному уравнению Шредингера. Разработанный метод апробирован на модельных системах, для которых известны точные аналитические или численные решения. Комбинируя данный метод с методом функционала плотности была рассчитана проводимость различных наноразмерных проводов. Также исследована стабильность осцилляций проводимости в натриевых моноатомных проводах по отношению к структурным изменениям в проводе и контактах между проводом и электродами.

В **первой главе** проведен обзор методов расчета электронной структуры и проводимости наноразмерных проводников. Изложены основные концепции метода функционала плотности, который использовался в данной работе для расчета электронной структуры проводников. Были обсуждены различные приближения, применяемые в практических расчетах по методу функционала плотности. В частности, подробно изложено приближение локальной плотности для обменно-корреляционного функционала. В данной главе описаны два метода решения уравнения Кона-Шэма в рамках метода псевдопотенциала. Первый метод основан на использовании импульсного представления, когда волновая функция разлагается в ряд Фурье, а второй - на конечно-разностной схеме высокого порядка. В данной работе импульсное представление использовалось для решения уравнения Кона-Шэма и определения одноэлектронного потенциала всей системы, состоящей из проводника и электродов. Затем при решении задачи рассеяния электрона в полученном потенциале применялся метод конечных разностей. Расчет проводимости осуществлялся по методу Ландауэра-Буттикера, который устанавливает связь между проводимостью наноразмерного проводника и амплитудами вероятности прохождения электрона через данный проводник и, поэтому, дан краткий обзор метода Ландауэра-Буттикера. В завершении первой

главы обсужден вопрос об области применимости метода функционала плотности и метода Хартри-Фока для расчета транспорта электрона.

Во **второй главе** исследовалась взаимосвязь между двумя методами расчета проводимости наноразмерных проводов и интерфейсов. Первый метод основан на формализме Ландауэра-Буттикера в сочетании с методом модовой шивки, позволяющим рассчитать коэффициенты прохождения, используемые для определения проводимости по формуле Ландауэра. Коэффициенты прохождения можно получить, определив волновую функцию всей системы при помощи шивки волновой функции в проводнике с электронными модами в электродах, которые представлены в виде полубесконечных кристаллических проводников. Во данной главе метод модовой шивки волновой функции, сформулированный Андо, обобщен на самый общий случай Гамильтониана, представленного в приближении сильной связи. Второй метод расчета проводимости основан на формализме неравновесных функций Грина, предложенном Келдышем, и формуле Кароли, позволяющей выразить проводимость через функции Грина. Нами показано, каким образом все результаты, полученные с помощью метода функций Грина вытекают из метода модовой шивки. Также была выведена простая формула, связывающая амплитуды вероятности прохождения электрона через наноразмерный проводник с запаздывающей функцией Грина для данного проводника. Связь между методами функций Грина и модовой шивки проиллюстрирована на примере точно решаемой одномерной задачи в рамках приближения сильной связи и на примере численного расчета из первых принципов проводимости туннельного перехода железо-вакуум-железо.

В **третьей главе** развит численный метод для расчета когерентного транспорта электрона через наноразмерные проводники и туннельные переходы. Этот метод основан на использовании конечно-разностной схемы высокого порядка для представления одноэлектронного Гамильтониана и волновой функции на решетке в координатном пространстве. В этом случае одноэлектронное уравнение формально имеет ту же форму, что и одноэлектронное уравнение, полученное в рамках приближения сильной связи. Используя формулу Ландауэра, рассчитывалась проводимость через амплитуды рассеяния, а задача рассеяния электрона на проводнике решалась методом модовой шивки, описанным во второй главе. Сходимость метода была исследована для модельных туннельных переходов и натриевых атомных проводов. В частности, нами показано, что использование высокопорядковой конечно-разностной схемы для кинетической энергии электрона позволяет добиваться высокой точности расчета проводимости при разумных вычислительных затратах. В данной главе представлены все вычислительные детали разработанного численного метода.

В **четвертой главе** исследована стабильность осцилляций проводимости в натриевых моноатомных проводах по отношению к структурным изменениям. Вначале выполнялся самосогласованный расчет по методу функционала плотности для получения геометрии, электронной структуры и одноэлектронного потенциала провода, помещенного между двумя натриевыми электродами. Затем исследовался транспорт электрона при помощи конечно-разностного метода, сформулированного в третьей главе. Показано, что проводимость моноатомных

проводов испытывает регулярные осцилляции при изменении числа атомов в проводе. Провода с нечетным числом атомов имеют проводимость близкую к квантовой единице проводимости, а провода с четным числом атомов обладают более низкой проводимостью. Более того, проводимость проводов с нечетным числом атомов является устойчивой по отношению к различным изменениям геометрии провода и контактов между проводом и электродами. Нами также показано, что проводимость проводов с четным числом атомов более чувствительна к подобным структурным изменениям. Разница между этими двумя типами проводов может быть объяснена резонансной природой транспорта электрона через моноатомный провод. В случае нечетного числа атомов в проводе рассеяние электрона на проводнике является резонансным и слабо зависит от формы резонансов и расстояния между резонансами. В проводах с четным числом атомов рассеяние электрона не является резонансным, и достаточно сильно зависит как от формы резонансов, так и от расстояния между ними. Если предположить, что провод является зарядово нейтральным, то есть считать, что подсоединение провода к электродам не приводит к переносу заряда между ними, то тогда осцилляции проводимости можно объяснить на основе простой модели, но для предсказания амплитуды этих осцилляций необходим самосогласованный расчет из первых принципов, чтобы учесть реальную геометрию и электронную структуру провода и электродов. Качественный аналитический анализ результатов, полученных из первых принципов, был проведен на основе простой модели. Нами показано, что условие зарядовой нейтральности моноатомных проводов накладывает сильное ограничение на фазу осцилляций проводимости. Поскольку реальный эффект переноса заряда между проводом и электродами не может быть предсказан из простой несамосогласованной модели, то использование методов расчета из первых принципов является принципиально важным для получения правильного одноэлектронного потенциала, и, соответственно, для предсказания правильной фазы осцилляций проводимости. Проводимость является достаточно чувствительной к качеству полученного потенциала, поэтому, выбор критерия сходимости должен быть более жестким, чем при расчете полной энергии системы, которая сходится быстрее чем одноэлектронный потенциал. Суммируя все результаты, полученные в четвертой главе, можно утверждать, что во всех рассмотренных случаях стабильность фазы осцилляций проводимости по отношению к структурным изменениям является следствием того, что перенос заряда между моноатомным проводом и электродами незначителен. Поэтому противоречивые результаты, которые можно найти в литературе, по поводу стабильности фазы осцилляций проводимости являются следствием некоего нефизического переноса заряда из-за применения слишком упрощенных моделей для описания провода и электродов.



## Acknowledgements

This is the final chapter of my thesis. It is hard to imagine that in order to start writing this last part of the book I had to spend a few years of life. Looking back I can say that I feel no regret for coming here to the Netherlands and spending all these years on the research that turned out to be challenging and very interesting. The Netherlands has been my second home for more than four years, and I would like to thank all the people whom I have met here and who made my life full and comfortable in spite of my being far from home. Of course, there are people who were very close to me over these years and to whom I would like to express my sincere gratitude especially. In particular, *I feel deep gratitude to:*

My promotor, professor *Paul Kelly*, for supporting me from the most beginning. I still remember my first moments in Twente when I got off the train, and Paul drove me to his place to give me a sport bike of his, and then we went for a ride towards the university. It turned out to be a rather dangerous adventure for Paul because the first I did was a collision with him. Fortunately, we survived and could reach the university successfully. That was how I got familiar with one of the most important elements of living in Holland - bicycling. Speaking more seriously, I thank you, Paul, for all good you did for me, for interesting discussions, for constructive remarks that helped in improving things. I would also like to thank Andrea Kelly heartily for the friendly atmosphere during home dinners that Andrea and Paul arranged for our group.

My supervisor, Dr. *Geert Brocks*, for the invaluable assistance in doing a project of ours. I have learnt a lot from him. One of the amazing things about Geert that his help quite often exceeded my expectation. Moreover, working with you, Geert, gives real pleasure. Your jokes and stories always make me smiling. Thank you for everything!

Our secretary, *Els Braker-Peerik*, for taking care of us, CMS kids. She was always a great help to me. Els, I feel a bit sorry for improving my Dutch too slowly. Maybe I really have to start teaching Dutch kids how to play chess as Paul suggested, but I have a fear that they can begin speaking Russian or/and English before I get fluent in Dutch. In any way, I promise to do something about it in the near future.

Dr. *Teo Valkering*, for his ability to listen carefully and for giving useful advices.

*Gerrit van Hummel*, for always being helpful in fixing computer's things and just for pleasant conversations.

Dr. *Maciej Zwierzycki*, for taking a leading role in many activities of the CMS group. Playing football and basketball, sailing and drinking were a part of the CMS life. Unfortunately, all these things except drinking were almost gone right after Maciej left the group for Germany. Maciej, come back, all the people need you! I also thank you for fruitful discussions that were a big help to me in solving many problems.

My room-mate at the university, *Paul Rusu*, for being patient to me. Paul, thank you for making daily life not boring. I think you should admit that my Romanian and your Russian have improved considerably since you moved to my room.

*Mohand Talanana*, for sharing his experience on science, computers and life. Mohand, thank you for many friendly chats.

Russian-speaking corner of CMS, *Volodymyr Karpan*, *Anton Starikov* and *Ilya Marushchenko*, for hot discussions about science and life, for preserving slav traditions and keeping my Russian up.

*Victor Popa*, for his help in understanding codes. Victor, your ability in explosive sneezing really impressed me.

New comers of the group, *Gianluca Giovanetti*, *Suleyman Er*, *Danny Vanpoucke*, *Qinfang Zhang* and *Zhicheng Zhong*, for joining the group. Gianluca, your thirst for knowledge always impresses me. Suleyman, thank you for pleasant way of spending time at the conferences and help with a poster. Danny, thank you a lot for helping with Dutch, I apologize for complaining about your Flemish accent.

Former member of the group, professor *Jeroen van den Brink*, for many interesting scientific discussions. Former master students, *Bart Husken*, *Geert Willem Spakman* and *Sijmen Gerritsen* for giving me an opportunity to get familiar with Dutch society and for being a big help to me in many cases.

I express my special gratitude to *Jordi Hernando* for being a perfect flatmate. Jordi, thank you for your natural kindness and tact. Your prominent sense of humour was a great help in many circumstances. Thank you for sharing a spirit of free Catalonia that made my national identity consistent with my nationality finally. Here I would also like to show gratitude to the Spanish community of UT for having a fine time together at parties and sports competitions.

I thank heartily all the Russian-speaking community of Twente in the person of *Nina Dziomkina* and *Vanya Nikolaev*, *Valera Souchkov*, *Sergej Kruglik*, *Sveta Bahatyrova*, *Natallia* and *Sergej Uzunbajakavy*, *Sergej Shkulipa*, *Vovan Shchetinin* and many others for all the good time spent together in all sorts of activities.

At last, I would like to show my undying gratitude to my wife, *Nata*, for making a great effort to prevent me from getting bored in this life.

Я хочу поблагодарить всю мою большую семью за ту любовь и поддержку, которую чувствую на протяжении всей моей жизни, и за то ощущение Дома, которое у меня возникает всякий раз по возвращению в Минск, мой родной город. И все это придает мне уверенности в любых начинаниях, поскольку при любых обстоятельствах я знаю, что есть место на земле, где меня всегда ждут.

Петя Хомяков  
Petr Khomyakov

# Curriculum Vitae

**Name:** Petr A. Khomyakov

**Date of birth:** March 25, 1975

**Place of birth:** Minsk, USSR

**Nationality:** Republic of Belarus

**Marital status:** Married

## EDUCATION

**June 1992** *Secondary School No. 88*, Minsk, Belarus.

- Graduated with gold medal (Educational Ministry Award).

**June 1997** *Belarussian State University*, Minsk, Belarus.

- Graduated with honors (average grade 4.9 at maximum 5.0).
- Diploma in Physics with major in Theoretical Physics.  
Subject: Operator method for non-polynomial potentials.

## EMPLOYMENT

**Nov 1997 - Nov 2000** *research assistant* in the group of Prof.dr. Lev I. Komarov, Department of Theoretical Physics, Faculty of Physics, Belarussian State University.

**Dec 2000 - Oct 2001** *junior research worker* at the Laboratory of Theoretical Physics, Institute of Physics of National Academy of Sciences of Belarus, in collaboration with Prof.dr. Ilya D. Feranchuk.

**Since Oct 2001** *research assistant* in the Computational Materials Science group of Prof.dr. Paul J. Kelly, University of Twente, the Netherlands, under supervision of Dr. Geert Brocks.





## Publications

P. A. Khomyakov and G. Brocks, *Stability of conductance oscillations in monatomic sodium wires*, submitted to Phys. Rev. B.

P. A. Khomyakov, G. Brocks, V. Karpan, M. Zwierzycki, and P. J. Kelly, *Conductance calculations for quantum wires and interfaces: Mode matching and Green's functions*, Phys. Rev. B **72**, 035450 (2005).

P. A. Khomyakov and G. Brocks, *Real-space finite-difference method for conductance calculations*, Phys. Rev. B **70**, 195402 (2004).

P. A. Khomyakov, *Perturbation theory for the one-dimensional optical polaron*, Phys. Rev. B **63**, 153405 (2001).

P. A. Khomyakov, *Operator method for solution of the Schrödinger equation with the rational potential*, Doklady Akademii Nauk Belarusi **45**(4), 49 (2001).

L. I. Komarov and P. A. Khomyakov, *Two-dimensional complex oscillator for description of a many-electron atom*, Nonlinear Phenomena in Complex Systems / An Interdisciplinary Journal **4**(4), 341 (2001).

I. D. Feranchuk and P. A. Khomyakov, *On an excited state of the one-dimensional optical polaron*, Nonlinear Phenomena in Complex Systems / An Interdisciplinary Journal **4**(4), 347 (2001).

P. A. Khomyakov, *Operator method for solution of the nonlinear Schrödinger equation*, Collected articles: Covariant methods in Theoretical physics. Elementary Particles Physics and Theory of Relativity. Minsk: Institute of Physics **5**, 169 (2001).

P. A. Khomyakov, *Perturbative calculation of the binding energy of the one-dimensional optical polaron*, Proc. of National Academy of Sciences of Belarus: Ser. fiz.-mat. **4**, 112 (1999).

P. A. Khomyakov, *On virial in theory of atom*, Proc. of International Workshop "Quantum systems 99: New Trends and Methods" (June 1999, Minsk), "MET": Minsk, 2000. - P.20.